Numerical modeling of conjugate magnetohydrodynamic flow phenomena

Blishchik, A.

DOI
10.4233/uuid:b3ffbc58-efa6-4761-a020-5240ea7948f1

Publication date
2022

Document Version
Final published version

Citation (APA)
Blishchik, A. (2022). *Numerical modeling of conjugate magnetohydrodynamic flow phenomena*. [Dissertation (TU Delft), Delft University of Technology]. https://doi.org/10.4233/uuid:b3ffbc58-efa6-4761-a020-5240ea7948f1

NUMERICAL MODELING OF CONJUGATE MAGNETOHYDRODYNAMIC FLOW PHENOMENA

NUMERICAL MODELING OF CONJUGATE MAGNETOHYDRODYNAMIC FLOW PHENOMENA

Dissertation

for the purpose of obtaining the degree of doctor
at Delft University of Technology
by the authority of the Rector Magnificus, prof.dr.ir. T.H.J.J. van der Hagen
chair of the Board for Doctorates
to be defended publicly on
Thursday 15 September 2022 at 10:00 o'clock

by

Artem BLISHCHIK

Master of Science in Applied Mathematics and Physics,
Peter the Great St. Petersburg Polytechnic University, Saint Petersburg, Russia
born in Saint Petersburg, Russia

This dissertation has been approved by the promotors.

Composition of the doctoral committee:

Rector Magnificus	chairperson
Prof. dr. S. Kenjereš	Delft University of Technology, promotor
Prof. dr. ir. C. R. Kleijn	Delft University of Technology, promotor
Independent members:	
Prof. dr. B. Knaepen	Université Libre de Bruxelles
Prof. dr. ir. B. J. Boersma	Delft University of Technology
Prof. dr. ir. C. Vuik	Delft University of Technology
Dr. rer. nat. D. Krasnov	Ilmenau University of Technology
Dr. D. van Odyck	Tata Steel Europe

This project has received funding from the European Union's Horizon 2020 research and innovation program TOMOCON (Smart Tomographic Sensors for Advanced Industrial Process Control) under the Marie Sklodowska-Curie grant agreement No. 764902.

Keywords: Magnetohydrodynamics, turbulence, steelmaking, simulations

Printed by: Ridderprint

Front & Back: Iana Kharlan

ISBN 978-94-6384-360-7

An electronic version of this dissertation is available at
`http://repository.tudelft.nl/`.

The rules are simple: they lie to us, we know they are lying, they know we know they are lying but they keep lying anyway, and we keep pretending to believe them.

Alexander Solzhenitsyn

CONTENTS

SUMMARY

Steel is found irreplaceable in many industrial applications. It is currently predicted that steel consumption will increase significantly in the coming decades. Humanity is expected to produce more and more steel-based products, such as cables, cars, railways, bridges, stadiums, skyscrapers, etc. The increased demand will pose a serious challenge to steel-producing companies. At the same time, these companies strive to reduce the amount of carbon emissions which are released during the majority of steel-making processes. Thus, the steel-producing corporations currently carry out a lot of reforms aimed at improving production efficiency and making plants environmentally friendly.

Continuous casting is a very important part of the steel-making process. During the continuous casting process, steel solidifies and takes the correct shape. There are several important nodes in this process, e.g. the tundish, the mold, the turning zone, etc. Given that the mold is the first stage where the solidification starts, a deep understanding of all physical phenomena in the mold flow could potentially help researchers to increase the process efficiency and the quality of final products. Originally, the mold flow is highly turbulent and unstable due to various physical processes arising simultaneously inside the mold. To control the flow, one of the tools widely used in the steel-making industry is the electromagnetic brake (EMBr).

The work of the EMBr is based on magnetohydrodynamic (MHD) principles. A strong magnet is used to impose an external magnetic field on the flow of liquid steel which is highly electrically conductive. Hence, the generated electric current inside the liquid steel results in an active Lorentz force affecting the flow. The most optimal and efficient configuration of the EMBr remains an open question as well as a full understanding of processes caused by EMBr. In particular, it is not clear whether the electric interaction between the solidified shell (which has also a relatively high electrical conductivity) and the turbulent flow of liquid steel is significant.

In order to investigate the above-mentioned phenomena related to the interaction between liquid steel and the solidified shell, several important steps have to be taken. First, due to the limitations of MHD experiments, a numerical MHD solver is needed. Second, this MHD solver should be able to predict the solid-liquid MHD interaction, for example, using a specific method called conjugate MHD. Magnetohydrodynamic turbulence should be also taken into account. Third, fundamental physics phenomena lying behind the solid-liquid MHD interaction must be clarified. Hence, in this dissertations, we are primarily addressing these points. We developed and implemented a numerical magnetohydrodynamic solver capable to predict a wide range of MHD phenomena including the solid-liquid MHD interaction. Our solver was successfully validated against

several reference cases and used to conduct all simulations presented in this dissertation. In order to gain a fundamental understanding of physics lying behind the solid-liquid MHD interaction, we first studied this effect in a simplified geometric configuration. Remarkably, we found that changes in electrical conductivity of the solid walls led to the appearance of the transitional flow regime. Stronger changes in electrical conductivity resulted in full turbulence suppression and then turbulence regeneration. Further investigation of the solid-liquid MHD interaction in the casting mold demonstrated the strong impact on the double-roll flow structure and on the sub-meniscus zone. Therefore, all attempts to increase the efficiency of the casting process via the EMBr should account for the presence of the solidified shell.

We hope that our work will help both fundamental researchers and engineers who work with magnetohydrodynamic flows of liquid metals to better understand the MHD phenomena.

SAMENVATTING

Staal is een onvervangbaar materiaal voor veel industriële processen. Er wordt voorspeld dat het gebruik van staal in de komende jaren alleen maar zal toenemen doordat de mensheid steeds meer staalproducten zal maken, zoals bijvoorbeeld kabels, auto's, spoorrails, bruggen, stadions, wolkenkrabbers, enz. De groter wordende vraag naar staal zal een grote uitdaging voor staalproducenten worden. Tegelijkertijd moeten deze bedrijven de emissies van CO2 en andere broeikasgassen, die vrijkomen bij het productieproces terugdringen. Staalproducenten maken daarom veel aanpassingen in de fabrieken om ze efficiënter en milieuvriendelijker te maken.

Continugieten is een zeer belangrijk onderdeel van het staalproductieproces. Tijdens het continugietproces stolt het staal en krijgt het de juiste vorm. Er zijn verschillende belangrijke onderdelen in dit proces, bijv. de tundish, de gietvorm, de draaizone, enz. Aangezien in de gietvorm de stolling begint, zou het begrip van alle fysische verschijnselen in de stroming in de gietvorm onderzoekers kunnen helpen om de kwaliteit van de producten te verbeteren. Oorspronkelijk is de stroming in de gietvorm zeer turbulent en onstabiel ten gevolge van verschillende fysische processen die zich gelijktijdig in de gietvorm voordoen. Om de stroming te beheersen, wordt in de staalindustrie op grote schaal gebruik gemaakt van de elektromagnetische rem (EMBr, Electro Magnetic Brake).

De werking van de EMBr is gebaseerd op magnetohydrodynamische (MHD) principes. Een sterke magneet wordt gebruikt om een extern magnetisch veld op te leggen aan de stroom van vloeibaar staal, die sterk elektrisch geleidend is. De opgewekte elektrische stroom in het vloeibare staal resulteert in een actieve Lorentz-kracht op de stroming. De meest optimale en efficiënte configuratie van de EMBr blijft een open vraag, evenals een volledig begrip van de processen die worden veroorzaakt door de EMBr. Het is niet duidelijk of de elektrische interactie tussen de mantel van gestold ijzer (die ook een relatief hoog elektrisch geleidingsvermogen heeft) en de turbulente stroom van vloeibaar staal significant is.

Om bovengenoemde interactie tussen vloeibaar staal en het gestolde ijzeren omhulsel te onderzoeken, moeten verschillende belangrijke stappen worden ondernomen. Ten eerst is, vanwege de beperkingen van MHD experimenten, een numerieke MHD aanpak nodig. Ten tweede moet deze numerieke MHD solver in staat zijn om de vast-vloeistof MHD interactie te voorspellen, bijvoorbeeld met behulp van een specifieke methode die "conjugate MHD" wordt genoemd. Magnetohydrodynamische turbulentie moet ook mee worden genomen. Ten derde moeten de fundamentele fysische fenomenen achter de vast-vloeibaar MHD interactie opgehelderd worden.

Vandaar dat we in dit proefschrift vooral deze punten behandelen. We hebben een

numerieke magnetohydrodynamische solver ontwikkeld en geïmplementeerd die in staat is om een breed scala van MHD fenomenen te voorspellen, waaronder de vast-vloeibaar MHD interactie. Onze solver werd met succes gevalideerd tegen verschillende voorbeelden uit de literatuur en gebruikt om alle simulaties uit te voeren die in dit proefschrift worden gepresenteerd. Om begrip te krijgen van de fysica die schuilgaat achter de vast-vloeibaar MHD interactie, hebben we dit effect eerst bestudeerd in een eenvoudige geometrische configuratie. Opmerkelijk was dat veranderingen in elektrisch geleidingsvermogen van de vaste wanden leidden tot het verschijnen van het laminar-turbulente overgangsregime. Sterkere veranderingen in elektrisch geleidingsvermogen resulteerden in volledige onderdrukking van turbulentie en vervolgens tot het opnieuw verschijnen van turbulentie. Verder onderzoek van de vast-vloeibaar MHD interactie in de gietvorm toonde de sterke invloed aan op de dubbele rol stromingsstructuur en op de submeniscus zone. Daarom moeten alle pogingen om de efficiëntie van het gietproces via de EMBr te verhogen, rekening houden met de aanwezigheid van de gestolde schil. Wij hopen dat ons werk zowel fundamentele onderzoekers als ingenieurs die werken met magnetohydrodynamische stromingen van vloeibare metalen zal helpen om de MHD fenomenen beter te begrijpen.

1

INTRODUCTION

1

1.1. APPLICATION BACKGROUND

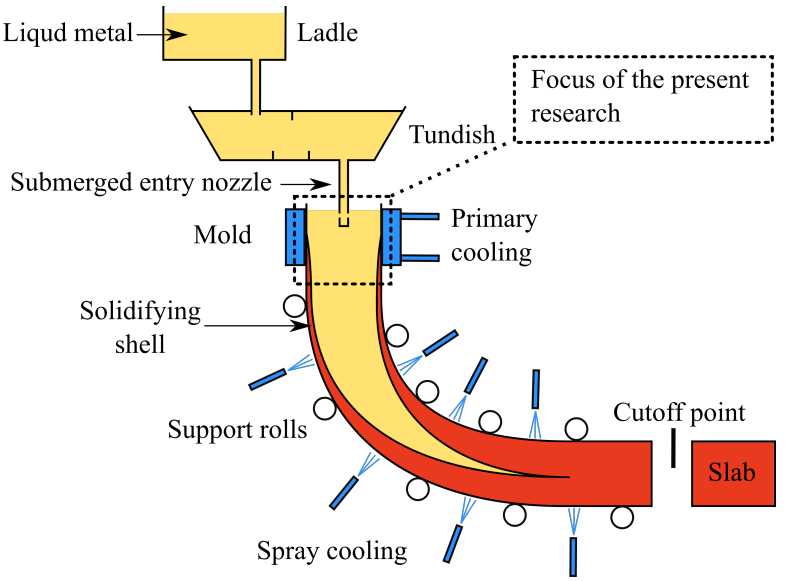

Figure 1.1: Schematic view of the continuous casting setup.

Prior to the invention of continuous casting (CC) technology, steel was poured into ingots using stationary molds. Such an operation was excessively costly and time-consuming, and, in the middle of the 18th century, Sir Henry Bessemer came up with the first idea of a continuous casting process [1]. However, the technological level at that time was not sufficient to implement such a large-scale project, and thus the first real continuous casting facilities were not built until the 1950s [2].

A schematic view of a continuous casting process is presented in Fig. 1.1. Several parts of the CC can be distinguished [3]. Liquid steel starts its way down from a ladle located at the top of the facility. The ladle is connected to a tundish which plays the role of an additional reservoir and a flow rate controller. Next, the liquid steel goes to a mold through a submerged entry nozzle (SEN). The mold performs several crucial functions, such as forming a casting shape, correcting the strand surface quality, and cooling the liquid steel via water-cooled walls. The resulting solidifying shell is moved down to a turning zone by support rolls. To continue the formation of the solidifying shell, an additional spray cooling system is applied in the turning zone. By reaching the cutoff point, the solidification process is completed and the shell is split into slabs. The slabs are further cooled to reach an acceptable temperature level and finally moved to storage.

The importance of the processes occurring in the mold has been already mentioned, and thus the mold represents one of the most critical nodes [4]. Naturally, there are many processes that can dramatically affect the final quality of slabs, such as separation of the solid shell, involvement of a slag layer, bubbles, etc., [5, 6]. A limited number of con-

trol tools are available in order to reduce the impact of the aforementioned interactions. Among the available options, particular attention is devoted to an electromagnetic brake (EMBr) which is able to suppress turbulence in the flow in the mold via an imposed external magnetic field [7]. Application of the electromagnetic brake becomes possible due to the electrically conductive nature of liquid metals and can be physically described in the framework of magnetohydrodynamics (MHD). The EMBr use is very common in the steel casting industry, but many open questions, especially related to MHD turbulence phenomena, still remain. To fully address these gaps, a new generation of studies has to be conducted. Thus, there are several important points that should be highlighted:

- Given the limitations of the measurement techniques in liquid steel flows as well as the enormous costs of the experimental setup, numerical MHD simulations appear as the most optimal and viable method.
- An MHD solver should be able to simulate solid-liquid MHD interactions. In order to do that, it is necessary to implement a specific method called conjugate MHD. The additional impact of the magnetohydrodynamic turbulence should be also taken into account.
- A detailed understanding of phenomena underlying solid-liquid MHD interactions must be obtained.

In this chapter, we discuss the main principles of magnetohydrodynamic flow and how to implement these principles in numerical solvers. Next, the MHD turbulence phenomenon is considered. Finally, we discuss the impact of the EMBr on a turbulent liquid metal flow in a casting mold.

1.2. FIELD OF RESEARCH

1.2.1. ONE-WAY COUPLED MAGNETOHYDRODYNAMICS

Magnetohydrodynamics describes the physics of electrically conductive fluid flows within the scope of both classical fluid dynamics and electromagnetism [8]. This phenomenon is widely found in space (astrophysical jets, nebulae) and on Earth (the geomagnetic dynamo) [9–13]. Technological implementation of MHD processes was found extremely useful in the following industrial applications: micro-pumps, sensors, crystal growth, fusion reactors, and the above-mentioned continuous casting [14–23]. In the latter case, magnetohydrodynamics determines the interplay between an electrically conductive incompressible fluid, i.e. a liquid metal, and an imposed external magnetic field. This interplay results in the occurrence of the Lorentz force affecting the fluid flow [24]. Given the dominant magnetic diffusivity of the liquid metals, the magnetic Reynolds number is small. Hence, an induced secondary magnetic field, arising from the generated electric current inside the electrically conductive fluid, can be neglected [25]. Following this statement, the one-way coupled magnetohydrodynamic governing

equations, i.e. the low magnetic Reynolds number, can be formulated as:

$$\nabla \cdot \mathbf{u} = 0 \tag{1.1}$$

$$\frac{\partial \mathbf{u}}{\partial t} + (\mathbf{u} \cdot \nabla)\mathbf{u} = -\frac{1}{\rho}\nabla p + \nu \nabla^2 \mathbf{u} + \frac{1}{\rho} \underbrace{(\mathbf{j} \times \mathbf{B})}_{\mathbf{F^L}} \tag{1.2}$$

$$\mathbf{j} = \sigma(-\nabla \phi + \mathbf{u} \times \mathbf{B}) \tag{1.3}$$

$$\nabla^2 \phi = \nabla \cdot (\mathbf{u} \times \mathbf{B}) \tag{1.4}$$

where $\mathbf{u}$, $\mathbf{B}$, $\mathbf{j}$, $\mathbf{F^L}$, p, ϕ, ν, ρ, σ are the fluid velocity, the imposed magnetic field, the current density, the Lorentz force, the pressure, the electric potential, the kinematic viscosity, the density,the electrical conductivity respectively. To characterize the MHD flow, the crucial non-dimensional numbers are introduced, namely the Hartmann number $Ha = BL\sqrt{\frac{\sigma}{\rho\nu}}$, the Reynolds number $Re = \frac{uL}{\nu}$, and the magnetic Reynolds number $Re_m = \frac{uL}{\eta}$, where L and η are the characteristic length and the magnetic diffusivity respectively.

Analytical solutions of equations (1.1) - (1.4) can be obtained only for relatively simple MHD flows, such as laminar flow in a channel, duct, and pipe [26–28]. To explore more complex flow physics in various geometrical configurations, researchers mostly use numerical simulations or experiments. Although studying MHD phenomena via numerical frameworks is more affordable compared to conducting real experiments, MHD modules in general-purpose commercial fluid flow simulation codes usually lack the ability to model application-specific physical phenomena. At the same time, these physical phenomena can play a decisive role under certain conditions. For example, neglecting influence of the electrically conductive solidified shell in the casting mold leads to incorrect prediction of the flow structure [29]. It is also an open question whether the impact of the EMBr on fluctuations on the meniscus free surface is significant [30]. In order to predict the above-mentioned phenomena, the development of an appropriate magnetohydrodynamic code becomes a vital task.

Several important points should be taken into account during the code implementation. First, one has to fulfill the conservation of the current density in order to avoid numerical instabilities, especially at high Hartmann numbers [31, 32]. Second, modeling of electrically conductive walls requires either resolving the conjugate fluid-solid current density transport or mimicking this transport via special boundary conditions [33]. Third, multiphase magnetohydrodynamics is often described in the framework of the modified Volume of Fluid method or by introducing the Lagrangian approach [34, 35]. Finally, the code must be validated with appropriate benchmark solutions. However, most of the available MHD benchmarks concentrate either on reproducing the influence of different Ha or determining the effect of the heat transfer [36–40]. This dissertation presents the new generation of MHD benchmarks and describes in detail the novel numerical implementation of arbitrary electrically conducting walls and multiphase phenomena.

1.2.2. MAGNETOHYDRODYNAMIC TURBULENCE

The vast majority of magnetohydrodynamic flows in industrial low-Re_m MHD applications are highly turbulent. Even dealing with "normal" turbulence significantly increases the complexity of a physical system, while the additional magnetic interaction brings new challenges. The impact of the applied magnetic field on low-Re_m turbulent flow can be expressed in terms of the following two principal mechanisms. First, the Lorentz force affects the mean flow and changes the flow structure. Second, the dissipation mechanism affects turbulence fluctuations themselves. Depending on the Hartmann and Reynolds numbers, the impact of these two principal mechanisms can be essential [41].

To investigate fundamental characteristics of MHD turbulence, flow in simplified configurations, such as a duct or a channel, are considered. Using these geometries is relatively simple but allows the reproduction of the main key features of magnetohydrodynamics, such as the Hartmann layer formation. Furthermore, the aforementioned configurations are geometrically close to those used in real industrial applications [21, 23]. Experimental studies, conducted for these configurations, clearly demonstrated the damping effect due to the application of an external magnetic field to a turbulent flow of a liquid metal [42–45]. The strongest damping effect was observed for a transverse orientation of the magnetic field, implying active involvement of both Lorentz force and Joule dissipation. By reducing the ratio $R = Re/Ha$, the magnetic suppression eventually transformed turbulent flow into a laminar flow. Thus, experiments provided the basic concept of the magnetic field influence while further analysis is complicated due to the lack of visualization [46].

Recent progress in high-performance computing has advanced the use of numerical simulations as the main tool for studying MHD turbulence. However, serious concerns have arisen related to the capacities of existing numerical methods to correctly determine the contribution of a magnetic field to turbulence [47]. Significant efforts have been made to expand the most effective Reynolds-Averaged-Navier-Stokes (RANS) turbulence models to incorporate MHD interactions. Modifications for $k-\epsilon$ and $k-\omega$ SST models have been successfully introduced, validated, and used in industrial applications [29, 48–50]. Detailed investigations have been conducted in the framework of the Large Eddy Simulations method (LES). Sub-grid scale (SGS) models relying on the dynamical procedure, such as the dynamic Smagorinsky model or WALE, demonstrated significantly better accuracy compared to the classical models based on the constant coefficients for sub-grid contribution. Correct behavior of dynamic SGS models is caused by the ability to be locally adapted according to changes in the dissipation rate [51–55]. Meanwhile, Direct Numerical Simulations (DNS) remain the most accurate but computationally expensive method [54].

Following the expansion of the numerical methods, low-Re_m MHD turbulence has been widely studied numerically, and fundamental analyses have been carried out [46, 56–60]. In particular, a detailed discussion was devoted to the pronounced anisotropy

promoted by the imposed magnetic field. Meanwhile, it was discovered that the transition process between the turbulent and the laminar state was not immediate. The so-called patterned turbulence phenomenon is characterized by the formation of coexisting separate laminar and turbulent spots in the vicinity of the walls [61–63]. Previously, this phenomenon was observed only for electrically insulated walls. In this investigation, we analyze the impact of electrically conductive walls on a turbulent MHD flow, and we demonstrate the onset of a double transition between the turbulent and laminar flow regimes.

1.2.3. THE MAGNETOHYDRODYNAMIC FLOW IN A CONTINUOUS CASTING MOLD

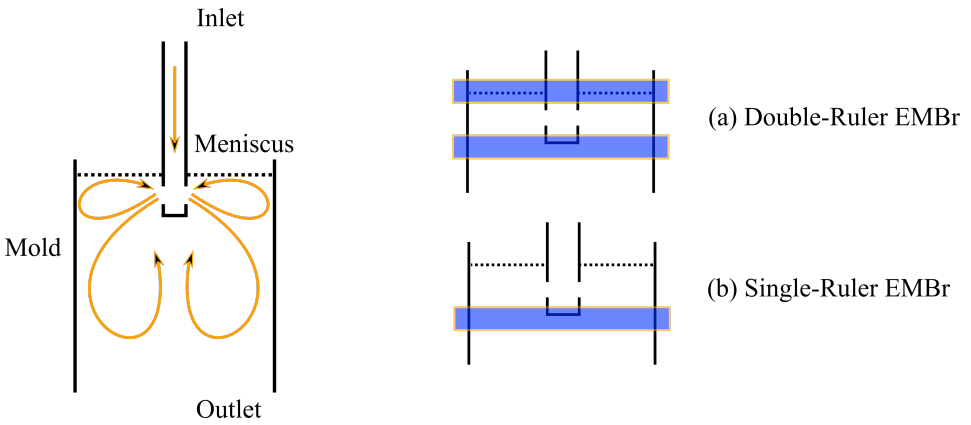

Figure 1.2: Schematic view of a liquid metal flow in a casting mold (left). The possible application of an electromagnetic brake (right). The magnetic field influence is shown in blue.

We now revisit the continuous casting process and discuss the application of the electromagnetic brake. The continuous casting mold is one of the last steps in the CC process after which the quality of the steel can not be improved significantly [64]. Ongoing research attempts have been made to increase production efficiency and to remove all unnecessary interactions from the mold flow [5, 6, 65–67]. Given the challenging operating conditions of the real casting process, most of the studies are focused on laboratory-scale casting facilities [68, 69]. The liquid-metal flow in the mold can be generally characterized by the presence of two smaller rolls close to the meniscus and two bigger rolls below the submerged-entry nozzle (SEN), Fig. 1.2. The present pattern is known as the double-roll flow structure and its behavior is critical to the entire process [65]. Multiple aspects of the double-roll flow have been reported to have a strong effect on the final product. One of the critical areas is the meniscus zone where the liquid slag is formed. High velocities occurring in the sub-meniscus zone can potentially capture the slag particles from the surface and involve them in the downstream flow [66]. The other critical aspect is related to bottom rolls where the strong jets can damage the so-

lidifying shell by imprinting, for instance, argon bubbles emerging from the SEN [70]. Consequently, controlling the liquid steel flow in the casting mold becomes a highly prioritized task.

It was found that the application of an external magnetic field could be used to control the flow. Currently, one can distinguish two ways to apply the magnetic field. First, application of a static field based on a direct current and generation a Lorentz force opposing the flow direction, i.e. the electromagnetic brake [71]. Second, application of a moving field based on an alternating current and generation a rotation flow in the mold, i.e. electromagnetic stirring [72]. In this investigation, we primarily focus on the electromagnetic brake. Given the contactless interaction between the magnetic field and the liquid metal, the EMBr represents an efficient and suitable tool. Since the first conception of EMBr, the device has been experimentally studied in order to expand its possible application area [73]. However, these studies were difficult due to need to use a liquid metal that hampers measurements. In past, to ease operation conditions, researchers used mercury instead of liquid steel. Later, mercury was replaced by an eutectic alloy of Gallium-Indium-Tin (GaInSn), which is much safer [74, 75]. Nevertheless, only limited information about the potential impact of the EMBr can be extracted from experiments, while numerical simulations provide a deeper insight into the flow physics [76, 77].

There are multiple electromagnetic brake configurations but the most effective layouts are the following: the single-ruler layout where the magnet is positioned slightly below the SEN, and the double-ruler layout where an additional magnet is positioned at the meniscus area, Fig. 1.2 [78–81]. Other geometric and flow parameters, such as the immersion depth of the SEN, mold dimensions, the casting speed, and the strength of the magnetic field contribute to the flow behavior as well [35, 77, 82–85]. In this investigation, we focus on the interaction between the the solidified shell and the flow in a continuous casting mold.

1.3. RESEARCH OBJECTIVES

In the above referenced works, the presence of arbitrary electrically conductive walls/ shell is usually neglected in both fundamental and engineering MHD studies. Nevertheless, the limited available knowledge demonstrates that the MHD flow can undergo dramatic changes in the presence of conductive walls. Given the widespread use of such walls in real applications, a thorough study should be conducted. Modeling the interactions between an electrically conductive fluid and electrically conductive walls lies outside the capability of conventional algorithms, and hence a tailored numerical method has to be developed. Validation against existing analytical solutions or benchmarks must be conducted prior to further analysis. Once the appropriate numerical tool is completed, it is crucial to investigate the fundamental flow physics to understand how MHD turbulence is influenced by the presence of conductive walls. To do that, a simplified geometry (rectangular duct) is used where all main MHD flow aspects can be captured. Next, the obtained understanding of the fundamental flow physics is applied to the con-

tinuous casting flow to investigate the impact of the electrically conductive solidified shell.

Our research questions are formulated as follows:

1. **How to model the interaction between electrically conductive walls and an electrically conductive flowing fluid?**
2. **How does the presence of electrically conductive walls affect the MHD turbulent flow?**
3. **What is the influence of an electrically conductive shell on the MHD liquid metal flow structure in a continuous casting mold?**

1.4. OUTLINE

We numerically investigate a one-way coupled magnetohydrodynamic liquid metal flow subjected to an external constant magnetic field, in Chapters 2, 3, 4, and 5. These chapters are self-contained articles that have been published in scientific journals. Detailed discussions about the applied numerical methods and schemes are presented in each chapter.

In Chapter 2 we address the problem of developing an appropriate numerical solver to model various magnetohydrodynamic flows. The following MHD cases are considered: a laminar flow in an insulated or partially conductive duct, a laminar back-step flow, a multiphase cavity flow, and a rising bubble. A comprehensive discussion of the implemented methods is provided as well as validation of the solver against existing benchmarks.

In Chapter 3 we briefly discuss how the presence of electrically conductive walls affects a turbulent MHD flow in a rectangular duct. A novel flow regime is observed, namely the gradual flow laminarization and the subsequent turbulence recovery.

In Chapter 4 we further continue the discussion started in Chapter 3. The analysis of second-order moments, turbulent kinetic energy budgets, energy spectrum, and turbulence anisotropy is demonstrated. We additionally illustrate the main principle of interaction between the current density redistribution mechanism and turbulence.

In Chapter 5 we study the MHD flow in a casting mold augmented with electrically conductive walls representing the solidified shell. A wide range of wall conductivity values is considered. Particular attention is given to changes in the double-roll flow structure and at the meniscus zone.

In Chapter 6 we conclude the dissertation with an overview of the achieved results. Further research opportunities are also described.

1.5. ACKNOWLEDGMENTS

This project has received funding from the European Union's Horizon 2020 research and innovation program TOMOCON (Smart Tomographic Sensors for Advanced Industrial

Process Control) under the Marie Sklodowska-Curie grant agreement No. 764902.

1

REFERENCES

[1] J.-P. Birat, *The relevance of Sir Henry Bessemer's ideas to the steel industry in the twenty-first century,* Ironmaking & Steelmaking **31**, 183 (2004).

[2] S. Mizoguchi, T. Ohashi, and T. Saeki, *Continuous casting of steel,* Annual Review of Materials Science **11**, 151 (1981).

[3] B. G. Thomas, *Continuous casting,* in *Encyclopedia of Materials: Science and Technology* (2011) pp. 1595–1598.

[4] B. G. Thomas, *Modeling of continuous casting defects related to mold fluid flow,* Iron and Steel Technology **3**, 127 (2006).

[5] L. Zhang, J. Aoki, and B. G. Thomas, *Inclusion removal by bubble flotation in a continuous casting mold,* Metallurgical and Materials Transactions B **37**, 361 (2006).

[6] B. G. Thomas, *Review on modeling and simulation of continuous casting,* Steel Research International **89**, 1700312 (2018).

[7] K. Cukierski and B. G. Thomas, *Flow control with local electromagnetic braking in continuous casting of steel slabs,* Metallurgical and Materials Transactions B **39**, 94 (2008).

[8] H.Alfven, *Existence of electromagnetic-hydrodynamic waves,* Nature **150**, 405 (1942).

[9] M. Janvier, G. Aulanier, and P. Démoulin, *From coronal observations to MHD simulations, the building blocks for 3D models of solar flares (invited review),* Solar Physics **290**, 3425 (2015).

[10] G. García-Segura, E. Villaver, N. Langer, S.-C. Yoon, and A. Manchado, *Single rotating stars and the formation of bipolar planetary nebula,* The Astrophysical Journal **783**, 74 (2014).

[11] A. Mignone, P. Rossi, G. Bodo, A. Ferrari, and S. Massaglia, *High-resolution 3D relativistic MHD simulations of jets,* Monthly Notices of the Royal Astronomical Society **402**, 7 (2010).

[12] T. Nakagawa, *Effect of a stably stratified layer near the outer boundary in numerical simulations of a magnetohydrodynamic dynamo in a rotating spherical shell and its implications for earth's core,* Physics of the Earth and Planetary Interiors **187**, 342 (2011).

[13] C. A. Jones, *Planetary magnetic fields and fluid dynamos,* Annual Review of Fluid Mechanics **43**, 583 (2011).

[14] M. Rivero and S. Cuevas, *Analysis of the slip condition in magnetohydrodynamic (MHD) micropumps,* Sensors and actuators B: Chemical **166**, 884 (2012).

[15] V. Patel and S. K. Kassegne, *Electroosmosis and thermal effects in magnetohydrodynamic (MHD) micropumps using 3D MHD equations,* Sensors and Actuators B: Chemical **122**, 42 (2007).

[16] E. Egorov, V. Agafonov, S. Avdyukhina, and S. Borisov, *Angular molecular–electronic sensor with negative magnetohydrodynamic feedback,* Sensors **18**, 245 (2018).

[17] D. R. Laughlin, *A magnetohydrodynamic angular motion sensor for anthropomorphic test device instrumentation,* SAE transactions , 1648 (1989).

[18] Y. Khine and J. Walker, *Thermoelectric magnetohydrodynamic effects during bridgman semiconductor crystal growth with a uniform axial magnetic field,* Journal of Crystal Growth **183**, 150 (1998).

[19] S. S. Molokov, R. Moreau, and H. K. Moffatt, *Magnetohydrodynamics: Historical evolution and trends*, Vol. 80 (Springer Science & Business Media, 2007).

[20] X. Liu, L. Liu, Z. Li, and Y. Wang, *Effects of cusp-shaped magnetic field on melt convection and oxygen transport in an industrial Cz-Si crystal growth,* Journal of crystal growth **354**, 101 (2012).

[21] L. Bühler, C. Mistrangelo, J. Konys, R. Bhattacharyay, Q. Huang, D. Obukhov, S. Smolentsev, and M. Utili, *Facilities, testing program and modeling needs for studying liquid metal magnetohydrodynamic flows in fusion blankets,* Fusion Engineering and Design **100**, 55 (2015).

[22] H. Zohm, *Magnetohydrodynamic stability of tokamaks* (John Wiley & Sons, 2015).

[23] B. G. Thomas and R. Chaudhary, *State of the art in electromagnetic flow control in continuous casting of steel slabs: Modeling and plant validation,* 6th International Conference on Electromagnetic Processing of Materials EPM (2009).

[24] J. Hartmann and F. Lazarus, *Theory of the laminar flow of an electrically conducting liquid in an homogeneous magnetic field,* Kongelige Danske Videnskabernes Selskab Matematisk **15**, 1 (1937).

[25] P. A. Davidson, *An introduction to magnetohydrodynamics*, Cambridge Texts in Applied Mathematics (Cambridge University Press, 2001).

[26] J. Shercliff, *Steady motion of conducting fluids in pipes under transverse magnetic fields,* Mathematical Proceedings of the Cambridge Philosophical Society **49**, 136 (1953).

[27] J. Shercliff, *Magnetohydrodynamic pipe flow. High Hartmann number.* Journal of Fluid Mechanics **13**, 513 (1962).

[28] J. Hunt, *Magnetohydrodynamic flow in rectangular ducts,* Journal of Fluid Mechanics **21**, 577 (1965).

[29] X. Miao, K. Timmel, D. Lucas, Z. Ren, S. Eckert, and G. Gerbeth, *Effect of an electromagnetic brake on the turbulent melt flow in a continuous-casting mold,* Metallurgical and Materials Transactions B **43**, 954 (2012).

[30] T. Toh, H. Hasegawa, and H. Harada, *Evaluation of multiphase phenomena in mold pool under in-mold electromagnetic stirring in steel continuous casting,* ISIJ International **41**, 1245 (2001).

[31] M.-J. Ni, R. Munipalli, N. B. Morley, P. Huang, and M. A. Abdou, *A current density conservative scheme for incompressible MHD flows at a low magnetic Reynolds number. Part I: On a rectangular collocated grid system,* Journal of Computational Physics **227**, 174 (2007).

[32] M.-J. Ni, R. Munipalli, P. Huang, N. B. Morley, and M. A. Abdou, *A current density conservative scheme for incompressible MHD flows at a low magnetic Reynolds number. Part II: On an arbitrary collocated mesh,* Journal of Computational Physics **227**, 205 (2007).

[33] J. Walker, *Magnetohydrodynamic flow in rectangular ducts with thin conducting walls,* Journal de Mecanique **20**, 79 (1981).

[34] B. W. Righolt, *Hydrodynamics of electromagnetically controlled jet oscillations*, Ph.D. thesis, Delft University of Technology (2016).

[35] C. Kratzsch, *Liquid Metal Flow in Continuous Casting Molds: A numerical approach of Electromagnetic Flow Control, Turbulence and multiphase phenomena*, Ph.D. thesis, Technical University of Bergakademie Freiberg (2018).

[36] S. Smolentsev, S. Badia, R. Bhattacharyay, L. Bühler, L. Chen, Q. Huang, H.-G. Jin, D. Krasnov, D.-W. Lee, E. M. De Les Valls, *et al.*, *An approach to verification and validation of MHD codes for fusion applications,* Fusion Engineering and Design **100**, 65 (2015).

[37] K. Mramor, R. Vertnik, and B. Šarler, *Simulation of laminar backward facing step flow under magnetic field with explicit local radial basis function collocation method,* Engineering Analysis with Boundary Elements **49**, 37 (2014).

[38] N. L. Gajbhiye, P. Throvagunta, and V. Eswaran, *Validation and verification of a robust 3-D MHD code,* Fusion Engineering and Design **128**, 7 (2018).

[39] J. Feng, H. Chen, Q. He, and M. Ye, *Further validation of liquid metal MHD code for unstructured grid based on openfoam,* Fusion Engineering and Design **100**, 260 (2015).

[40] M.-J. Ni, R. Munipalli, N. B. Morley, P. Huang, and M. A. Abdou, *Validation case results for 2D and 3D MHD simulations,* Fusion Science and Technology **52**, 587 (2007).

[41] D. Biskamp, *Magnetohydrodynamic turbulence* (Cambridge University Press, 2003).

[42] P. Moresco and T. Alboussiere, *Experimental study of the instability of the Hartmann layer,* Journal of Fluid Mechanics **504**, 167 (2004).

[43] C. B. Reed and P. S. Lykoudis, *The effect of a transverse magnetic field on shear turbulence,* Journal of Fluid Mechanics **89**, 147 (1978).

[44] J. Baylis, *Experiments on laminar flow in curved channels of square section,* Journal of Fluid Mechanics **48**, 417 (1971).

[45] A. Pothérat and R. Klein, *Why, how and when MHD turbulence at low becomes three-dimensional,* Journal of Fluid Mechanics **761**, 168 (2014).

[46] D. Krasnov, O. Zikanov, and T. Boeck, *Numerical study of magnetohydrodynamic duct flow at high Reynolds and Hartmann numbers,* Journal of Fluid Mechanics **704**, 421 (2012).

[47] S. Kenjereš, *On modeling and eddy-resolving simulations of flow, turbulence, mixing and heat transfer of electrically conducting and magnetizing fluids: A review,* International Journal of Heat and Fluid Flow **73**, 270 (2018).

[48] H.-C. Ji and R. Gardner, *Numerical analysis of turbulent pipe flow in a transverse magnetic field,* International journal of heat and mass transfer **40**, 1839 (1997).

[49] O. Widlund, S. Zahrai, and F. H. Bark, *Development of a Reynolds stress closure for modeling of homogeneous MHD turbulence,* Physics of fluids **10**, 1987 (1998).

[50] S. Kenjereš and K. Hanjalić, *On the implementation of effects of Lorentz force in turbulence closure models,* International Journal of Heat and Fluid Flow **21**, 329 (2000).

[51] D. K. Lilly, *A proposed modification of the Germano subgrid-scale closure method,* Physics of Fluids A: Fluid Dynamics **4**, 633 (1992).

[52] F. Nicoud and F. Ducros, *Subgrid-scale stress modelling based on the square of the velocity gradient tensor,* Flow, turbulence and Combustion **62**, 183 (1999).

[53] H. Kobayashi, *Large eddy simulation of magnetohydrodynamic turbulent channel flows with local subgrid-scale model based on coherent structures,* Physics of Fluids **18**, 045107 (2006).

[54] D. Krasnov, O. Zikanov, J. Schumacher, and T. Boeck, *Magnetohydrodynamic turbulence in a channel with spanwise magnetic field,* Physics of Fluids **20**, 095105 (2008).

[55] V. I. Artemov, M. V. Makarov, K. B. Minko, and G. G. Yankov, *Assessment of performance of subgrid stress models for a les technique for predicting suppression of turbulence and heat transfer in channel flows under the influence of body forces,* International Journal of Heat and Mass Transfer **146**, 118822 (2020).

[56] L. Bühler, T. Arlt, T. Boeck, L. Braiden, V. Chowdhury, D. Krasnov, C. Mistrangelo, S. Molokov, and J. Priede, *Magnetically induced instabilities in duct flows,* IOP Conference Series: Materials Science and Engineering **228**, 012003 (2017).

[57] R. Chaudhary, S. Vanka, and B. Thomas, *Direct numerical simulations of magnetic field effects on turbulent flow in a square duct,* Physics of Fluids **22**, 075102 (2010).

[58] O. Zikanov, D. Krasnov, T. Boeck, and S. Sukoriansky, *Decay of turbulence in a liquid metal duct flow with transverse magnetic field,* Journal of Fluid Mechanics **867**, 661 (2019).

[59] S. Kenjereš, *Energy spectra and turbulence generation in the wake of magnetic obstacles,* Physics of Fluids **24**, 115111 (2012).

[60] M. Kinet, B. Knaepen, and S. Molokov, *Instabilities and transition in magnetohydrodynamic flows in ducts with electrically conducting walls,* Physical Review Letters **103**, 154501 (2009).

[61] D. Krasnov, A. Thess, T. Boeck, Y. Zhao, and O. Zikanov, *Patterned turbulence in liquid metal flow: Computational reconstruction of the Hartmann experiment,* Physical review letters **110**, 084501 (2013).

[62] O. Zikanov, D. Krasnov, T. Boeck, A. Thess, and M. Rossi, *Laminar-turbulent transition in magnetohydrodynamic duct, pipe, and channel flows,* Applied Mechanics Reviews **66** (2014).

[63] O. Zikanov, D. Krasnov, Y. Li, T. Boeck, and A. Thess, *Patterned turbulence in spatially evolving magnetohydrodynamic duct and pipe flows,* Theoretical and Computational Fluid Dynamics **28**, 319 (2014).

[64] L. Zhang and B. G. Thomas, *Inclusions in continuous casting of steel,* XXIV National Steelmaking Symposium, Morelia, Mich, Mexico **26**, 28 (2003).

[65] B. G. Thomas and L. Zhang, *Mathematical modeling of fluid flow in continuous casting,* ISIJ International **41**, 1181 (2001).

[66] L. C. Hibbeler and B. G. Thomas, *Mold slag entrainment mechanisms in continuous casting molds,* Iron Steel Technol **10**, 121 (2013).

[67] Y. Wang and L. Zhang, *Fluid flow-related transport phenomena in steel slab continuous casting strands under electromagnetic brake,* Metallurgical and Materials Transactions B **42**, 1319 (2011).

[68] K. Timmel, S. Eckert, G. Gerbeth, F. Stefani, and T. Wondrak, *Experimental modeling of the continuous casting process of steel using low melting point metal alloys—the limmcast program,* ISIJ International **50**, 1134 (2010).

[69] K. Timmel, S. Eckert, and G. Gerbeth, *Experimental investigation of the flow in a continuous-casting mold under the influence of a transverse, direct current magnetic field,* Metallurgical and Materials Transactions B **42**, 68 (2011).

[70] L. Zhang, S. Yang, K. Cai, J. Li, X. Wan, and B. G. Thomas, *Investigation of fluid flow and steel cleanliness in the continuous casting strand,* Metallurgical and Materials Transactions B **38**, 63 (2007).

[71] J. Nagai, K. Suzuki, S. Kojima, and S. Kollberg, *Steel flow control in a high-speed continuous slab caster using an electromagnetic brake,* Iron and Steel Engineer **61**, 41 (1984).

[72] K.-H. Spitzer, M. Dubke, and K. Schwerdtfeger, *Rotational electromagnetic stirring in continuous casting of round strands,* Metallurgical Transactions B **17**, 119 (1986).

[73] S.-M. Cho and B. G. Thomas, *Electromagnetic forces in continuous casting of steel slabs,* Metals **9**, 471 (2019).

[74] T. Wondrak, S. Eckert, G. Gerbeth, K. Klotsche, F. Stefani, K. Timmel, A. J. Peyton, N. Terzija, and W. Yin, *Combined electromagnetic tomography for determining two-phase flow characteristics in the submerged entry nozzle and in the mold of a continuous casting model,* Metallurgical and Materials Transactions B **42**, 1201 (2011).

[75] Y. Plevachuk, V. Sklyarchuk, S. Eckert, G. Gerbeth, and R. Novakovic, *Thermophysical properties of the liquid Ga–In–Sn eutectic alloy,* Journal of Chemical & Engineering Data **59**, 757 (2014).

[76] D. Schurmann, B. Willers, G. Hackl, Y. Tang, and S. Eckert, *Experimental study of the mold flow induced by a swirling flow nozzle and electromagnetic stirring for continuous casting of round blooms,* Metallurgical and Materials Transactions B **50**, 716 (2019).

[77] D. Schurmann, I. Glavinić, B. Willers, K. Timmel, and S. Eckert, *Impact of the electromagnetic brake position on the flow structure in a slab continuous casting mold: An experimental parameter study,* Metallurgical and Materials Transactions B **51**, 61 (2020).

[78] R. Chaudhary, B. Thomas, and S. Vanka, *Effect of electromagnetic ruler braking (EMBr) on transient turbulent flow in continuous slab casting using large eddy simulations,* Metallurgical and Materials Transactions B **43**, 532 (2012).

[79] R. Singh, B. G. Thomas, and S. P. Vanka, *Large eddy simulations of double-ruler electromagnetic field effect on transient flow during continuous casting,* Metallurgical and Materials Transactions B **45**, 1098 (2014).

[80] S.-M. Cho, S.-H. Kim, and B. G. Thomas, *Transient fluid flow during steady continuous casting of steel slabs: Part II. Effect of double-ruler electro-magnetic braking,* ISIJ International **54**, 855 (2014).

[81] B. Thomas, R. Singh, S. Vanka, K. Timmel, S. Eckert, and G. Gerbeth, *Effect of single-ruler electromagnetic braking (EMBr) location on transient flow in continuous casting,* Journal for Manufacturing Science and Production **15**, 93 (2015).

[82] P. Andrzejewski, K.-U. Köhler, and W. Pluschkell, *Model investigations on the fluid flow in continuous casting moulds of wide dimensions,* Steel Research **63**, 242 (1992).

[83] D. Gupta and A. K. Lahiri, *A water model study of the flow asymmetry inside a continuous slab casting mold,* Metallurgical and Materials Transactions B **27**, 757 (1996).

[84] Q. Zhang, L. Wang, and X. Wang, *Influence of casting speed variation during unsteady continuous casting on non-metallic inclusions in if steel slabs,* ISIJ International **46**, 1421 (2006).

[85] Z. Liu, A. Vakhrushev, M. Wu, E. Karimi-Sibaki, A. Kharicha, A. Ludwig, and B. Li, *Effect of an electrically-conducting wall on transient magnetohydrodynamic flow in a continuous-casting mold with an electromagnetic brake,* Metals **8**, 609 (2018).

2

THE MAGNETOHYDRODYNAMIC SOLVER AND NUMERICAL BENCHMARKS

There is a continuous need for an updated series of numerical benchmarks dealing with various aspects of the magnetohydrodynamics (MHD) phenomena (i.e. interactions of the flow of an electrically conducting fluid and an externally imposed magnetic field). The focus of the present study is numerical magnetohydrodynamics (MHD) where we have performed an extensive series of simulations for generic configurations, including: (i) a laminar conjugate MHD flow in a duct with varied electrical conductivity of the walls, (ii) a back-step flow, (iii) a multiphase cavity flow, and (iv) a rising bubble in liquid metal. All considered benchmark situations are for the one-way coupled MHD approach, where the induced magnetic field is negligible. The governing equations describing the one-way coupled MHD phenomena are numerically implemented in the open-source code OpenFOAM. The novel elements of the numerical algorithm include fully-conservative forms of the discretized Lorentz force in the momentum equation and divergence-free current density, the conjugate MHD (coupling of the wall/fluid domains), and, finally, the multi-phase MHD. The multiphase phenomena are simulated with the Volume of Fluid (VoF) approach. The presented extensive numerical benchmarks are expected to be potentially useful for developers of the numerical codes used to simulate various types of the complex MHD phenomena.

Published as: A. Blishchik, M. van der Lans, S. Kenjereš, An extensive numerical benchmark of the various magnetohydrodynamic flows. International Journal of Heat and Fluid Flow 90, 108800, 2021, doi: 10.1016/j.ijheatfluidflow.2021.108800

2.1. INTRODUCTION

One of the pre-requisites to be able to deal with advanced physical transport phenomena involving the magnetohydrodynamics (MHD) interactions is to have a well-validated and numerically efficient computer code. This still poses a quite challenging task due to a lack of advanced experimental studies that can provide detailed insights into the flow and electromagnetic parameters that can be used to validate computer codes. The essence of the MHD phenomena is usually associated with a flow of highly electrically conducting liquid metals, which are, due to their non-transparency, notoriously difficult to study with standard laser-based optics diagnostics tools.

To validate MHD numerical models, we have to rely on analytical solutions that are based on significant simplifications. In the present manuscript, we are revisiting and proposing an extensive list of possible benchmark cases available in the open literature dealing with various aspects of the MHD phenomena. One of the simplest numerical MHD benchmarks is a fully developed laminar channel, duct, or pipe flow subjected to a uniform magnetic field of different orientations, for which an exact analytical solution exists, [1], [2]. The effects of the non-uniform longitudinal magnetic field on a laminar flow of electrically conducting fluid in a pipe were recently numerically simulated in [3]. The open-source computer code OpenFOAM was used and good agreement was obtained between simulations and experiments. The MHD flow in a duct with very thin electrically conducting walls was presented in [4]. Instead of fully resolving the wall region, a special type of boundary conditions was applied at the wall/fluid interface that takes into account a finite wall conductivity, as proposed in [5]. It should be noted that this approach can be applied only for a very thin wall thickness and small conductance ratios.

Fusion engineering and technology-related research include numerous topics dealing with the MHD phenomena. Smolentsev et al.[6] provided an extensive review of MHD codes for fusion applications and selected benchmark problems of importance for fusion applications. The proposed benchmarks covered a series of 2D and 3D steady and developing MHD flows in both laminar and turbulent regimes, and the final case also included the effects of thermal buoyancy. Gajbhiye et al.[7] validated their general-purpose solver by analyzing the free convection in a cubical enclosure under a uniform magnetic field and the electro-magnetically driven flow in a toroidal duct. The commercial ANSYS-CFX finite-volume based code was used to simulate a water-cooled lithium lead (WCLL) breeding blanket module subjected to a strong uniform magnetic field, [8]. The commercial multi-physics finite-element code COMSOL was successfully applied to simulate transient natural convection phenomena under influence of the imposed uniform magnetic field, [9].

Validation of the multi-phase MHD flows is a challenging topic. The number of validation studies dealing with multi-phase MHD phenomena is significantly smaller compared to single-phase MHD phenomena. The analytical solutions for the multi-phase MHD situations are very scarce. One of the recently proposed analytical solu-

tions for a 2D multi-phase MHD flow is presented in [10], where the elevation of the liquid-metal/air interface due to the presence of an imposed magnetic field is analytically solved. Numerical simulations of a rising bubble in the liquid metal subjected to an external homogeneous magnetic field of different strengths were studied in [11]. The finite-difference code was used and the terminal bubble velocity dependency on the strength of the imposed magnetic field was analyzed.

The main goal of the present study is to obtain and validate results from our newly developed OpenFOAM solver over a range of various magnetohydrodynamic flows, and based on these findings, to propose an extensive numerical MHD benchmark, which can be potentially useful for developers of the computer codes for simulations of the MHD phenomena. We are primarily focusing on the influence of the finite electric conductivity of surrounding walls and the multiphase aspects of the MHD phenomena. We have analyzed the following situations: (i) a laminar duct flow with finite conductivity of surrounding walls, (ii) a laminar back-step flow, (iii) a shallow 2D multi-phase cavity, and, finally, (iv) a rising bubble in the liquid metal. For all mentioned cases we performed a detailed comparative assessment against available analytical solutions or/and numerical results presented in the literature.

2.2. GOVERNING EQUATIONS AND NUMERICAL DETAILS

2.2.1. GOVERNING EQUATIONS FOR A SINGLE-PHASE MHD

We consider an incompressible electrically conductive fluid with liquid metal properties. The fluid is affected by the imposed external (constant) magnetic field through the Lorentz force. Conservation of mass and momentum are used to describe the MHD flow (under the assumption that the imposed magnetic field is known), and are written as:

$$\nabla \cdot \mathbf{U} = 0 \tag{2.1}$$

$$\frac{\partial \mathbf{U}}{\partial t} + (\mathbf{U} \cdot \nabla)\mathbf{U} = -\frac{1}{\rho}\nabla p + \nu \nabla^2 \mathbf{U} + \frac{1}{\rho}(\mathbf{J} \times \mathbf{B}) \tag{2.2}$$

where $\mathbf{U}$ is velocity, p is pressure, ν is the kinematic viscosity, ρ is density, $\mathbf{J}$ is the current density, and $\mathbf{B}$ is the imposed magnetic field. In the momentum equation, the MHD interactions are accounted for through the Lorentz force term. In addition to the velocity and pressure, also the current density ($\mathbf{J}$) needs to be calculated. For the one-way coupled MHD phenomena, i.e. when the following conditions are valid:

$$Re_m = \frac{UL}{\lambda} << 1 \tag{2.3}$$

where Re_m is the magnetic Reynolds number, L is the characteristic length and λ is the magnetic diffusion, ν is the kinematic viscosity, Ohm's law for a moving conducting fluid is used:

$$\mathbf{J} = \sigma(-\nabla\phi + \mathbf{U} \times \mathbf{B}) \tag{2.4}$$

where σ is the electrical conductivity of the fluid. By imposing the divergence-free current density condition in Ohm's law, i.e.

$$\nabla \cdot \mathbf{J} = 0 \tag{2.5}$$

the final Poisson's equation for the electric potential (ϕ) is obtained and can be written as:

$$\nabla^2 \phi = \nabla \cdot (\mathbf{U} \times \mathbf{B}) \tag{2.6}$$

In addition to Re_m (given in Eqn. (2.3)), the hydrodynamic Reynolds and Hartmann number are used as typical MHD non-dimensional parameters:

$$Re = \frac{UL}{\nu}, \quad Ha = BL\sqrt{\frac{\sigma}{\rho \nu}} \tag{2.7}$$

2.2.2. GOVERNING EQUATIONS FOR A MULTI-PHASE MHD: VOLUME OF FLUID METHOD

In the current study, the Volume of Fluid (VoF) method is applied to the multi-phase MHD flow simulations. In addition to the Lorentz force, also the surface-tension and gravitational forces need to be included into the momentum equation:

$$\frac{\partial \mathbf{U}}{\partial t} + (\mathbf{U} \cdot \nabla)\mathbf{U} = -\frac{1}{\rho_{av}} \nabla p + \nu_{av} \nabla^2 \mathbf{U} + \frac{1}{\rho_{av}} \Big((\mathbf{J} \times \mathbf{B}) + \mathbf{f_g} + \gamma k \nabla \alpha \Big) \tag{2.8}$$

where $\mathbf{f_g}$ is the gravity force term, γ is the surface tension, k is the curvature of the interface (calculated as $k = \nabla \cdot \frac{\nabla \alpha}{|\nabla \alpha|}$), ν_{av} is the phase averaged viscosity (calculated as $\nu_{av} = \alpha \cdot \nu_1 + (1-\alpha) \cdot \nu_2$, where '1' and '2' are phase indicators), ρ_{av} is the phase averaged density (calculated as $\rho_{av} = \alpha \cdot \rho_1 + (1-\alpha) \cdot \rho_2$) and the volume fraction α is described by the following transport equation:

$$\frac{\partial \alpha}{\partial t} + \nabla \cdot (\alpha \mathbf{U}) + \nabla \cdot \Big(\mathbf{U}_r \alpha (1-\alpha) \Big) = 0 \tag{2.9}$$

where $\mathbf{U_r}$ is the artificial compression velocity used for the interface sharpening, which is calculated as:

$$\mathbf{U_r} = \mathbf{n}_f min\Big[C_\alpha \frac{|\psi|}{|S_f|}, max\Big(\frac{|\psi|}{|S_f|} \Big) \Big] \tag{2.10}$$

where $\mathbf{n_f}$ is the normal vector of the cell surface, ψ is the mass flux through the face, S_f is the cell surface area, and C_α is a coefficient that is used to control the interface thickness. There is no artificial interface compression when $C_\alpha = 0$. In order to control

the spurious velocities which appear near the interface due to the sharp change of α, the volume fraction function is smoothed by the following Laplacian filter [12], [13]:

$$\widetilde{\alpha_c} = \frac{\sum_{f=1}^{n}(\alpha_f S_f)}{\sum_{f=1}^{n}(S_f)} \tag{2.11}$$

where $\widetilde{\alpha}$ is the resulting smooth volume fraction function, while subscripts c and f indicate the cell center and cell face, respectively. Using the smooth function $\widetilde{\alpha}$ in Eqn. (2.9), instead of the original function α will suppress these parasitic velocities. In the current study, the filter (2.11) is applied twice for each time step.

2.2.3. NUMERICAL DETAILS

THE CONSERVATIVE FORM OF THE LORENTZ FORCE

The additional Lorentz force in the momentum equation is traditionally treated in a non-conservative way (i.e. by applying the volume integration of the source term). This can potentially lead to significant numerical errors, especially for flow regimes with high Hartmann numbers. Similarly, the total electric current density must be conserved too. Both of these requirements are achieved through the application of the Four Steps Projection Method (FSPM) proposed by [14], which can be summarized through the following four steps:

1. Calculate the magnetic flux at cell faces:

$$\psi_{mhd} = \sigma_f(\mathbf{U}\times\mathbf{B})_f \cdot \mathbf{S_f} \tag{2.12}$$

where the cell -face electric conductivity (σ_f) is calculated by applying the harmonic average between different phases, and ($\mathbf{S_f}$) is the cell surface area vector.

2. Use Eqn. (2.12) to solve the discretized electrical potential equation and find electric potential (ϕ) at the cell centers:

$$\sum_{f=1}^{m} \sigma_f \nabla_{nf}\phi \cdot |\mathbf{S_f}| = \sum_{f=1}^{m} \psi_{mhd} \tag{2.13}$$

where 'm' indicates the number of cell faces.

3. Calculate the current density flux at cell faces using the surface-normal gradient of electric potential (ϕ):

$$J_n = -\sigma_f \nabla_{nf}\phi \cdot |\mathbf{S_f}| + \psi_{mhd} \tag{2.14}$$

where (J_n) is the cell face normal component of the current density.

4. Finally, use the current density flux from Eqn. (2.14) and calculate the fully conservative form of the Lorentz force as:

$$(\mathbf{J}\times\mathbf{B})_c = -\frac{1}{\Omega_c}\sum_{f=1}^{m}(J_n)_f(\mathbf{B}_f\times\mathbf{r_f}) - \mathbf{r_c}\times\frac{1}{\Omega_c}\sum_{f=1}^{m}(J_n)_f\mathbf{B}_f \tag{2.15}$$

where (Ω_c) is the volume of cell, $(\mathbf{r_c})$ is the cell center distance vector and $(\mathbf{r_f})$ is the face center distance vector.

CONJUGATE MHD: TAKING INTO ACCOUNT ELECTRIC CONDUCTIVITY AND THICKNESS OF SURROUNDING WALLS

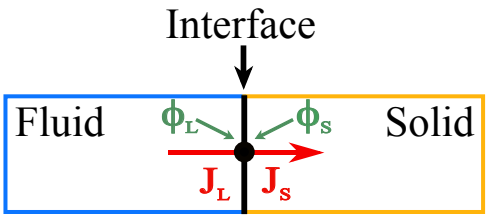

Figure 2.1: Sketch of the fluid/wall interface condition for the conjugate MHD problem.

The finite electric conductivity and finite thickness of surrounding walls have a significant impact on the fluid flow. This is due to the effects of the current density transfer between a liquid layer and solid walls, which is directly influencing the intensity and direction of the local Lorentz force in the near-wall region. To include the fluid/wall interface effects, we have developed an approach similar to traditional conjugate heat transfer, but now instead of the heat flux transfer, we focus on the distribution of the electric potential and current density in both domains. Transport equations of the electric potential in liquid (L) and solid (S) wall domains can be written as:

$$\nabla\cdot(\sigma_L\nabla\phi_L) = \nabla\cdot\left(\sigma_L(\mathbf{U}\times\mathbf{B})\right) \tag{2.16}$$

$$\nabla\cdot(\sigma_S\nabla\phi_S) = 0 \tag{2.17}$$

Note that the source term (the RHS of Eqn. (2.17) is absent for the solid wall domain. Along the fluid/wall interface (Fig. 2.1), the conservation and continuity of the electric current density $(\mathbf{J})$ need to be kept. This is achieved by imposing following set of the boundary conditions at the interface:

$$\sigma_L\frac{\partial\phi_L}{\partial n} = \sigma_S\frac{\partial\phi_S}{\partial n} \tag{2.18}$$

$$\phi_L = \phi_S \tag{2.19}$$

The electric current density in the computational cell center is calculated in the same manner for both liquid and solid part of computational domain as:

$$\mathbf{J_c}_{[L,S]} = \frac{1}{\Omega_c} \sum_{f=1}^{m} \left((J_{n,f})_{[L,S]} \cdot \mathbf{r_f} \right) - \mathbf{r_c} \cdot \frac{1}{\Omega} \sum_{f=1}^{m} (J_{n,f})_{[L,S]} \tag{2.20}$$

where the harmonic average is used to interpolate the electric conductivity at the interface, needed for calculation of the current density flux at the cell faces ($J_{n,f}$).

THE COMPUTER CODE

The integrated MHD solver, which includes all above-listed transport equations, for both single- and multi-phase MHD phenomena is based on the finite-volume open-source computer code OpenFOAM-extend 4.0, [15]. Coupling between pressure and velocity field is performed with the PISO algorithm, [16].

2.3. APPLICATIONS: TEST CASES

2.3.1. LAMINAR DUCT FLOW WITH CONJUGATE MHD

In the first test case, we address a laminar pressure-driven flow of an electrically conducting fluid in the rectangular duct subjected to a transverse magnetic field, Fig. 2.2.

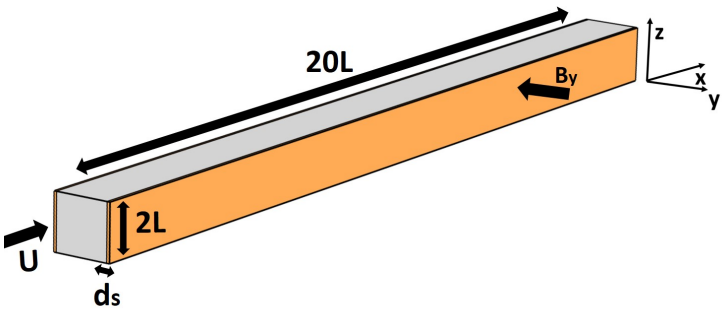

Figure 2.2: Sketch of the simulated domain for a laminar MHD flow in a duct with Hartmann walls with finite electric conductivity, subjected to a transverse magnetic field.

The duct has the square cross-section (where L- is the half-width), length of $20L$ and d_s is the thickness of side-walls (Hartmann walls). The Reynolds number is kept constant at $Re = 10$ and the Hartmann number is varied in the $0 \leq Ha \leq 10^4$ range. At the inlet, a uniform velocity profile is imposed. At all walls, the no-slip velocity boundary conditions are applied. At the outlet, a zero-pressure boundary condition is imposed. The uniform transverse magnetic field is imposed. To deal with the finite-thickness surrounding walls, we introduce characteristic wall conductance parameter, defined as:

$$C_d = (\sigma_S d_s) / (\sigma_L L). \tag{2.21}$$

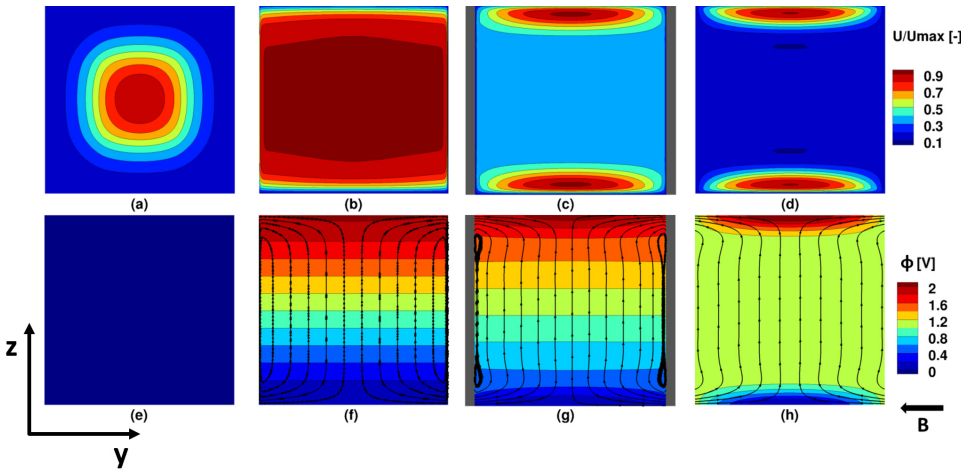

Figure 2.3: The contours of the streamwise velocity (top row) and electric potential with current density streamlines (bottom row) in the center of the conjugate MHD duct flow: (a), (e) Ha = 0. (b), (f) Ha = 100, fully insulated walls ($C_d = 0$). (c), (g) Ha = 100, arbitrary conductive walls ($C_d = 0.1$). (d), (h) Ha = 100, fully conductive walls ($C_d \to \infty$).

Three types of electric boundary conditions for the walls perpendicular to the magnetic field (Hartmann walls) are considered: (i) arbitrary conductive walls with varied wall conductance parameter ($0.005 \leq C_d \leq 40$), (ii) fully electrically insulated walls ($\partial\phi/\partial n = 0$ and $d_S = 0$), and finally, (iii) fully conductive walls ($\phi = 0$ and $d_S = 0$). The walls parallel to the magnetic field (Shercliff walls) are considered as electrically insulated for all cases. Although the final steady-state results are validated against analytical solutions, the solution procedure is performed in a time-dependent mode. This time-dependent approach is not numerically efficient, but our final goal is to have a well-validated solver able to simulate MHD phenomena in transient flow regimes, so we adopted a time-dependent solution approach for all benchmark cases presented here. The second-order central difference scheme (CDS) is applied for both convective and diffusive terms of discretized momentum equation, whereas the second-order backward scheme is used for time integration.

For all simulations the same hexahedral non-uniform orthogonal mesh is used with $(\mathrm{Nx} \times \mathrm{Ny} \times \mathrm{Nz} = 80 \times 100 \times 100)_{\mathrm{fluid}}$ control volumes for the fluid domain and $(\mathrm{Nx} \times \mathrm{Ny} \times \mathrm{Nz} = 80 \times 10 \times 100)_{\mathrm{solid}}$ for the solid domain, respectively. In making the spatial distribution of the non-uniform mesh, special attention is devoted that the characteristic Hartmann and Shercliff boundary layers (with a typical thickness of $\delta_{Ha} = L/Ha$ and $\delta_{Sh} = L/Ha^{1/2}$) are properly resolved. This is achieved by placing between 5 and 10 control volumes with a typical grid expansion ratio of 1.14 in the region bounded by the wall and the edge of the boundary layer (at δ_{Ha}).

Contours of the calculated streamwise velocity and electric potential- after reaching

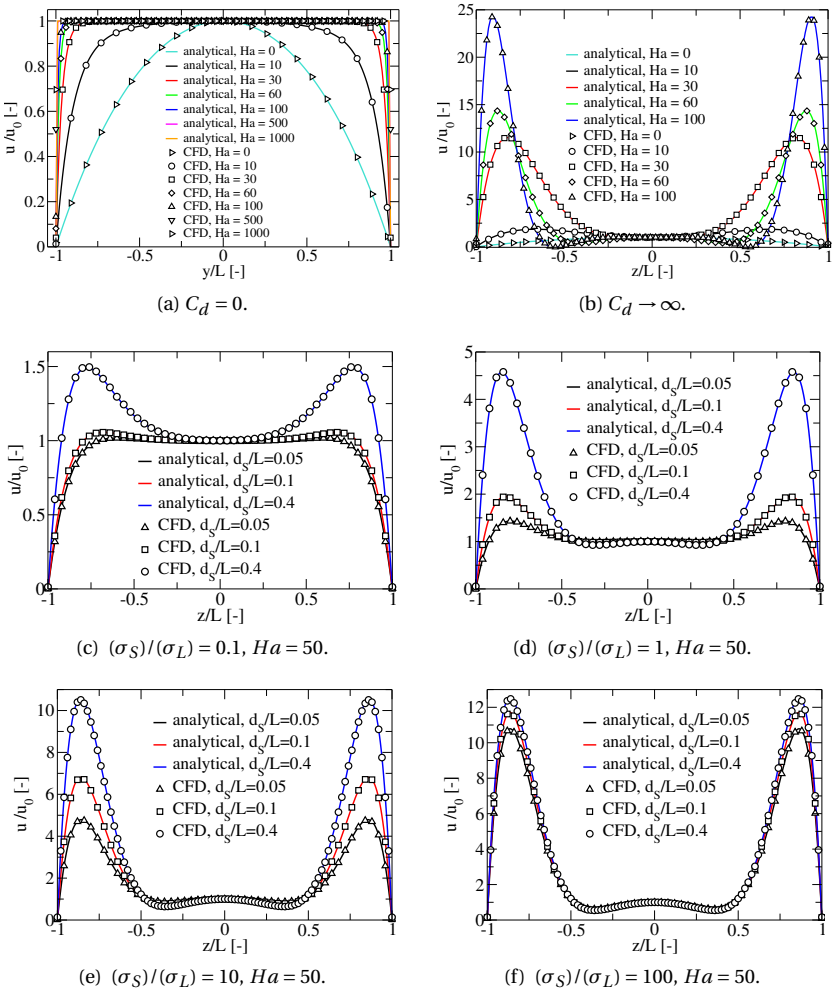

(a) $C_d = 0$. (b) $C_d \to \infty$.

(c) $(\sigma_S)/(\sigma_L) = 0.1$, $Ha = 50$. (d) $(\sigma_S)/(\sigma_L) = 1$, $Ha = 50$.

(e) $(\sigma_S)/(\sigma_L) = 10$, $Ha = 50$. (f) $(\sigma_S)/(\sigma_L) = 100$, $Ha = 50$.

Figure 2.4: The streamwise velocity profiles along y-axis (between Hartmann walls) and z-axis (between Shercliff walls) in the duct at various C_d and Ha.

a steady state in the center of the duct ($x = 10L$) - are shown in Fig. 2.3. For the MHD neutral case ($Ha = 0$) the velocity exhibits a typical symmetric parabolic-like distribution, Fig2.3(a). By imposing the transverse magnetic field ($Ha = 100$) and by keeping all duct walls electrically insulated, a flattening of the velocity distribution occurs in the central part of the duct, whereas thin Hartmann boundary layers are generated along opposite vertical walls, Fig. 2.3(b). Next, by keeping the same strength and direction of the imposed magnetic field, and by changing electric properties of the vertical walls from fully insulated to walls with a finite thickness and conductivity (i.e. $C_d = 0.1$), we observe a

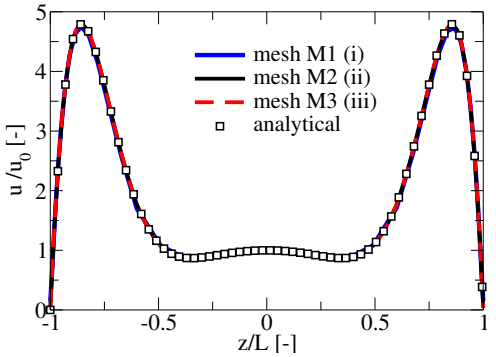

Figure 2.5: Numerical mesh dependency on the streamwise velocity profiles along z-axis in a conjugate MHD duct, $C_d = 0.5$, $Ha = 50$.

dramatic reorganization of the velocity with peaks in the proximity of the Shercliff walls, Fig. 2.3(c). Finally, by making Hartmann walls fully electrically conducting ($C_d \rightarrow \infty$), the velocity distribution with two peaks is still present, Fig. 2.3(d). The electric potential contours exhibit close to a linear distribution in the vertical direction for electrically insulated and finite-conductivity Hartmann walls, Figs.2.3(f, g). In contrast to this, the perfectly electrically conducting Hartmann walls impose almost a uniform distribution in the central part of the duct, Fig. 2.3(h).

The numerical solutions are compared next against the following analytical solutions: (1) Shercliff's solution for the electrically insulated walls, [2], (2) Hunt's solution for the electrically fully conductive walls, [17], and (3) Sloan's solution for the walls with the arbitrary electrical conductivity and thickness, [18]. For all simulated cases, an excellent agreement between present numerical simulations and analytical solutions is obtained, confirming an adequate implementation and validation of the conjugate MHD solver, Fig. 2.4.

To illustrate the sensitivity of the numerical solution, we perform a mesh dependency study with three mesh levels: (i) the coarse mesh (M1), $(\mathrm{Nx} \times \mathrm{Ny} \times \mathrm{Nz} = 40 \times 50 \times 50)_{\mathrm{fluid}}$ and $(\mathrm{Nx_s} \times \mathrm{Ny_s} \times \mathrm{Nz_s} = 40 \times 5 \times 50)_{\mathrm{solid}} = (0.11 \times 10^6)_{\mathrm{total}}$ CVs, (ii) the present mesh (M2) $(\mathrm{Nx} \times \mathrm{Ny} \times \mathrm{Nz} = 80 \times 100 \times 100)_{\mathrm{fluid}}$ and $(\mathrm{Nx_s} \times \mathrm{Ny_s} \times \mathrm{Nz_s} = 80 \times 10 \times 100)_{\mathrm{solid}} = (0.88 \times 10^6)_{\mathrm{total}}$ CVs and (iii) the fine mesh (M3) $(\mathrm{Nx} \times \mathrm{Ny} \times \mathrm{Nz} = 160 \times 200 \times 200)_{\mathrm{fluid}}$ and $(\mathrm{Nx_s} \times \mathrm{Ny_s} \times \mathrm{Nz_s} = 160 \times 20 \times 200)_{\mathrm{solid}} = (7.04 \times 10^6)_{\mathrm{total}}$ CVs. As it can be seen in Fig. 2.5, a very good agreement with the analytical solution is obtained for the intermediate (M2) and fine mesh (M3), and that a slight underprediction of the double peaks is observed for the coarse mesh (M1). To test possible limits of the numerical stability and accuracy, two additional high values of $Ha = 5000$ and 10000 are simulated for the case with finite electrically conducting walls ($C_d = 0.05$), Fig. 2.6. For such high values of Ha, very strong wall jets are generated along Shercliff walls. With a proper mesh refinement in the proximity of walls, i.e. $(\mathrm{Nx} \times \mathrm{Ny} \times \mathrm{Nz} = 100 \times 180 \times 180)_{\mathrm{fluid}}$ control volumes for the fluid domain and

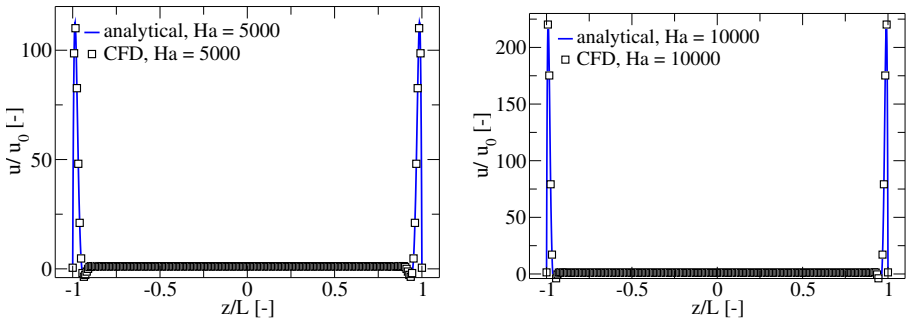

(a) $Ha = 5000$. (b) $Ha = 10000$.

Figure 2.6: The streamwise velocity profiles along z-axis (between Shercliff walls) in the duct with arbitrary conductivity walls, ($C_d = 0.05$) for $Ha = 5 \times 10^3$ (a) and $Ha = 10^4$ (b), respectively.

$(\mathrm{Nx} \times \mathrm{Ny} \times \mathrm{Nz} = 100 \times 15 \times 180)_{\mathrm{solid}}$ for the solid domain, Again, a very good agreement is obtained between numerical simulations and analytical solutions for both values of Ha, additionally proving the accuracy and numerical stability of the algorithm.

2.3.2. THE 2D MHD LAMINAR BACK-STEP FLOW

Next, we consider the two-dimensional backward-facing step flow in a laminar flow regime subjected to a uniform vertical magnetic field, Fig. 2.7.

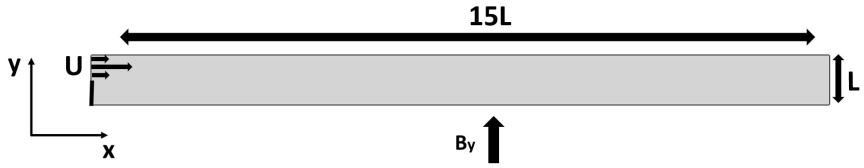

Figure 2.7: The sketch of the simulation domain of the 2D laminar MHD back-step test case.

In contrast to the previous case, this configuration is expected to produce a more complex flow pattern with a well-defined recirculation region in the lower part of the domain. The channel height is L and its length is $15L$. The lower and upper boundaries of the channel are no-slip walls. The upper half of the left boundary is the inlet, while the lower half is the solid wall. The inlet velocity is defined as:

$$u(x=0,y) = \begin{cases} 12(y-1)(1-2y), & L/2 < y < L \\ 0, & 0 < y < L/2 \end{cases} \tag{2.22}$$

For the right boundary, a simple zero-gradient condition is imposed. All walls are treated as perfectly electrically insulated. The simulation domain and all boundary conditions are selected such that they match exactly the numerical study of [19], who applied an

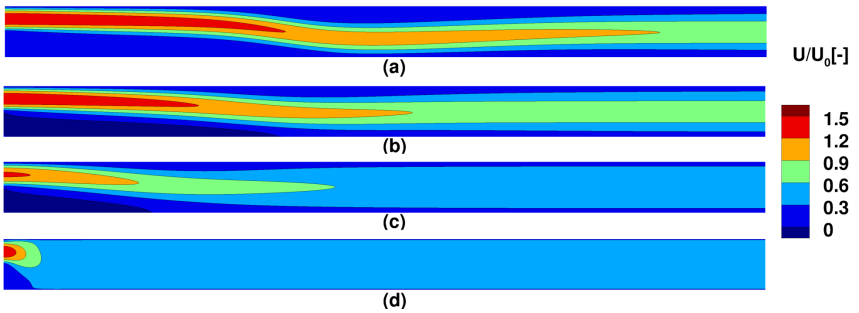

Figure 2.8: The contours of the non-dimensional horizontal (streamwise) velocity (u/u_0) for Re = 800 and different Ha. (a) $Ha = 0$, (b) $Ha = 5$, (c) $Ha = 10$, (d) $Ha = 50$.

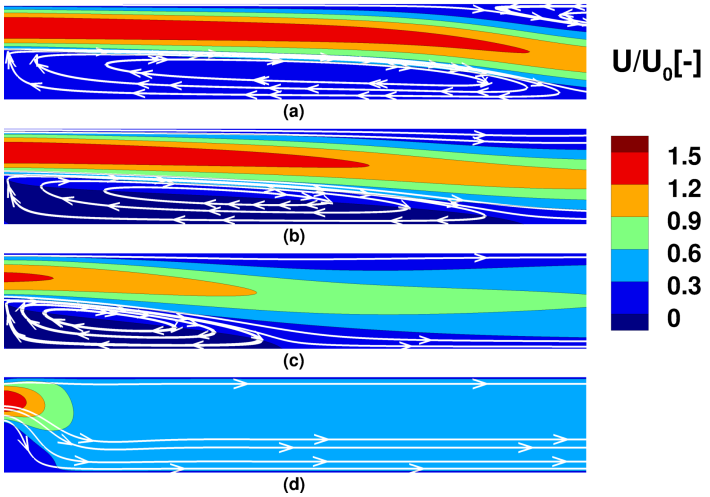

Figure 2.9: Same as in the previous figure, only now the zoom-in regions in the proximity of the inlet are shown with superimposed streamlines.

MHD extension of the Local Radial Basis Function Collocation Method (LRBFCM). The entire simulation domain is represented by an orthogonal numerical mesh with (Nx × Ny = 600 × 50) = $(3 \times 10^4)_{\text{total}}$ control volumes. Two values of the Reynolds number are simulated (Re = 300 and 800, where $Re = \overline{u_x} L/\nu$) over a range of Hartmann numbers ($0 \leq \text{Ha} \leq 50$). The second-order linear upwind differential scheme is used for convective terms, the second-order central differencing scheme (CDS) is used for diffusion terms, and the second-order backward scheme for the time integration.

The contours of the non-dimensional streamwise velocity (u/u_0 where $u_0 = \left(\overline{u_x}\right)|_{x=0}$, i.e. the inlet integrated velocity profile), at Re = 800 and different strengths of the imposed magnetic field ($Ha = 0$, 5, 10 and 50) are shown in Fig. 2.8. It can be seen that with a magnetic field increase, the recirculation length reduces, and flow becomes much more

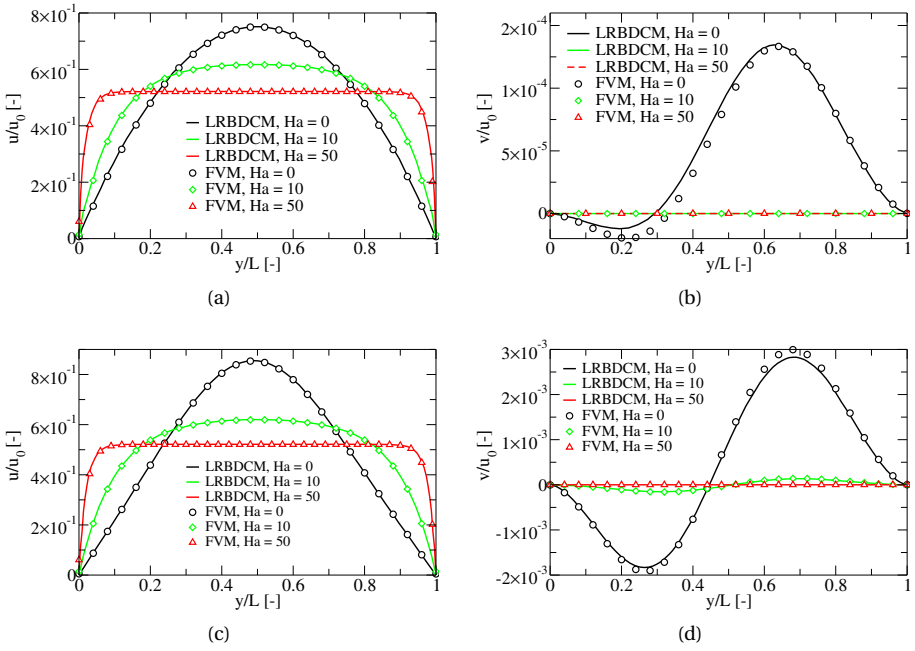

Figure 2.10: The vertical profiles of the non-dimensional horizontal (u/u_0) and vertical (v/u_0) velocity components at various Ha and two values of Re: $Re = 300$ (a-b) and $Re = 800$ (c-d). Comparison between the reference study based on the Local Radial Basis Function Collocation Method (LRBFCM) [19] and the present Finite Volume Method (FVM) results.

uniform. At $Ha = 0$, two large recirculation regions along the upper and lower walls are generated. With Ha increase, the recirculation region along the upper wall disappears, while the recirculation long the lower wall is still present, but its length is significantly reduced. This reduction of the recirculation region is further illustrated in zoom-in plots, where we superimposed contours of the streamwise velocity and streamlines, as shown in Fig. 2.9. At the highest value of $Ha = 50$, the recirculation can be observed only in a very small region attached to the lower part of the inlet plane. A comparison of obtained profiles of horizontal (u/u_0) and vertical (v/u_0) velocity components at the exit plane with values presented in the literature [19], are shown in Fig. 2.10. It can be seen that the horizontal velocity profiles become flatter with the magnetic field increase for both Reynolds numbers. The vertical velocity component almost completely disappears at higher values of Ha. A very good agreement between the present profiles and results from the literature ([19]) is obtained for all presented cases.

To demonstrate that the obtained results at present mesh of ($Nx \times Ny = 600 \times 50$) (M2) ($3 \times 10^4$ CVs) are grid independent, one coarser ($Nx \times Ny = 300 \times 25$) (M1) ($0.75 \times 10^4$ CVs) and one finner ($Nx \times Ny = 1200 \times 100$) (M3) ($1.2 \times 10^5$ CVs) numerical mesh are generated, and results are compared in Fig. 2.11. A good agreement between different mesh levels

Table 2.1: The reattachment position (at $y/L = 0$ for $Re = 300$ and 800, and $0 \leq Ha \leq 100$).

Re	Ha	present x/L	LRBFCM, [19] x/L
300	0	3.57	3.57
	5	2.56	2.55
	10	1.28	1.28
	50	0.02	0.02
	100	0.007	0.01
800	0	6.07	6.1
	5	5.46	5.48
	10	2.93	2.93
	50	0.07	0.07
	100	0.01	0.01

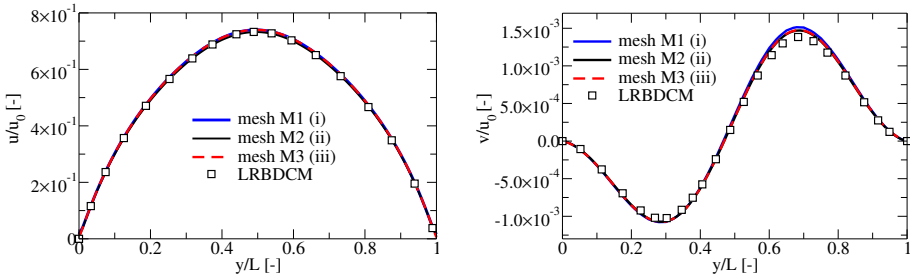

Figure 2.11: The non-dimensional horizontal (u/u_0) and vertical (v/u_0) velocity profiles at the exit plane for various meshes at $Re = 800$ and $Ha = 5$ compared to the reference solution (LRBFCM, [19]).

is obtained, with a slight overprediction of the local maxima of the non-dimensional vertical velocity (v/u_0) at $y/L = 0.7$ for the coarse mesh.

2.3.3. THE MULTI-PHASE TWO-DIMENSIONAL SHALLOW CAVITY FLOW WITH MHD

The first example of the MHD multi-phase test case is a shallow cavity subjected to combined effects of the imposed non-uniform magnetic field and electric potential difference. The two-dimensional cavity with characteristic length L and partially filled with the electrically conductive liquid (where d is the liquid layer height and $d << L$) is shown in Fig. 2.12. The upper part of the cavity if filled with air ($\sigma_{air} = \mathcal{O}(10^{-15})$ S/m, i.e. negligible electric conductivity).

The external magnetic field is aligned with the negative z-direction (perpendicular

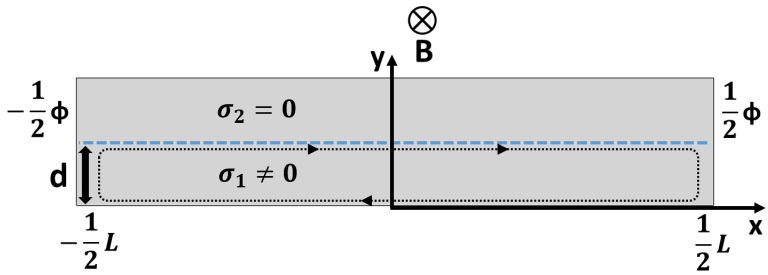

Figure 2.12: The sketch of the simulation domain of a two-dimensional multi-phase MHD cavity test case.

to the cavity) and its linear distribution is defined as:

$$\mathbf{B} = -b_0(1 + \alpha_b \cdot x)\hat{\mathbf{z}} \tag{2.23}$$

where $\alpha_b = 0.1$ defines a distribution parameter. The no-slip velocity boundary condition is imposed at all walls (i.e. bottom and side-walls). The gravity force is aligned with the negative y-coordinate direction. The side-walls are kept at constant (but different) electric potential ($\phi_1 = -\frac{1}{2}\Delta\phi$, $\phi_2 = \frac{1}{2}\Delta\phi$, where $\Delta\phi$ is the imposed electric potential difference). The bottom wall is perfectly electrically insulated ($\partial\phi/\partial n = 0$ and $C_d = 0$). Because of the imposed magnetic field and electric potential difference, the generated Lorentz force within the fluid will drive the flow. This fluid motion will be opposed by a joint combination of the viscous, gravitational, and surface tension forces. To account for additional free-surface related physical mechanisms, the following set of non-dimensional parameters is introduced, [10]:

$$Re^* = \frac{U^* d}{\nu}, \quad Ha^* = b_0 d\sqrt{\frac{\sigma\alpha_b}{\mu}}, \quad Bo^* = \frac{\rho g d^2}{\gamma}, \quad Ca^* = \frac{\rho\nu U^*}{\gamma} \tag{2.24}$$

In addition to the redefined Reynolds (Re^*) and Hartmann (Ha^*), also the Bond (Bo^*) and capillary (Ca^*) numbers are introduced. The characteristic non-dimensional velocity is calculated as:

$$U^* = \frac{\sigma\Delta\phi b_0 \alpha_b d A}{\rho\nu} \tag{2.25}$$

Because of the large number of possibilities based on the various combinations of characteristic non-dimensional numbers, in the present chapter we kept constant $Re^* = A$ and $Ha^* = 1$, while we change Bo^* and Ca^*. We also kept the identical aspect ratio of the domain, $A = d/L = 0.1$. The two-dimensional orthogonal, non-uniform mesh (Nx × Ny = 50 × 200) with rectangular control volumes is used. The central differencing scheme (CDS) is used for the diffusive and convective terms of transport equations. The time integration is performed with the second-order backward scheme. For this particular case, the different values of the interface compression coefficient ($0 \leq C_\alpha \leq 1$) did

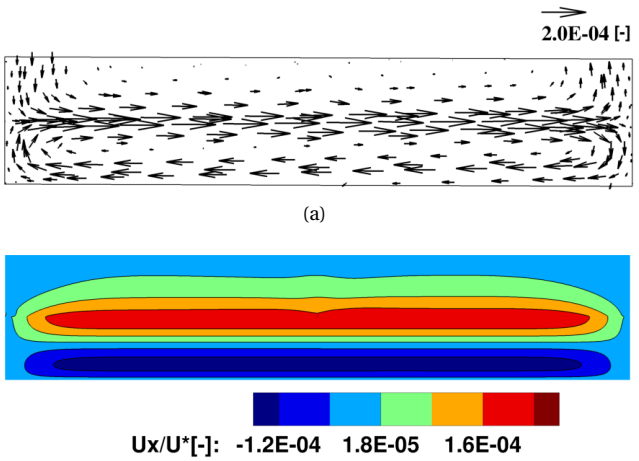

Figure 2.13: The velocity vector distribution (a) and contours of the non-dimensional horizontal (x-component) velocity (U_x/U^*) in the 2D MHD cavity, $Re^* = A, Ha^* = 1, Bo^* = A^2, Ca^* = A^4$.

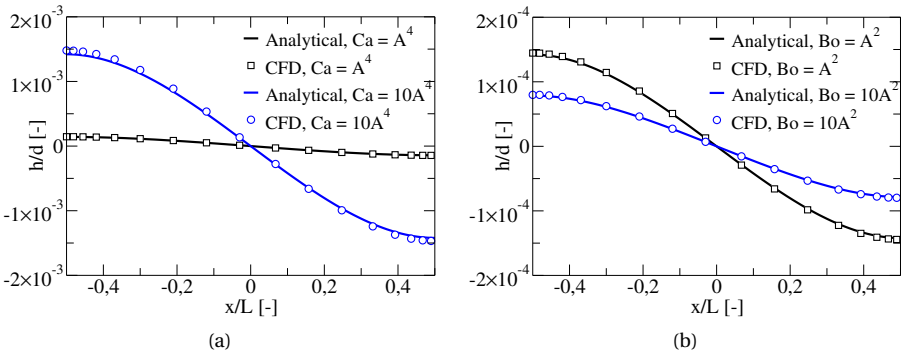

Figure 2.14: The free-surface elevation for various (a) Ca and (b) Bo. Comparison between the present simulations (CFD) and analytical solution of [10].

not have any significant impact on the obtained solutions due to a smooth free-surface deformation. The local variation of the resulting Lorentz force generates the flow of electrically conducting fluid (initially at rest) in the lower part of the cavity with characteristic elevation of the free surface, as shown in Fig. 2.13.

This non-dimensional vertical elevation (h/d) of the free-surface, as a function of Ca^* and Bo^* numbers, is shown in Fig. 2.14. It can be seen that an excellent match between the present numerical results (CFD) and analytical solutions is obtained for all calculated cases. Note that a vertical elevation of the free-surface increases with an increase

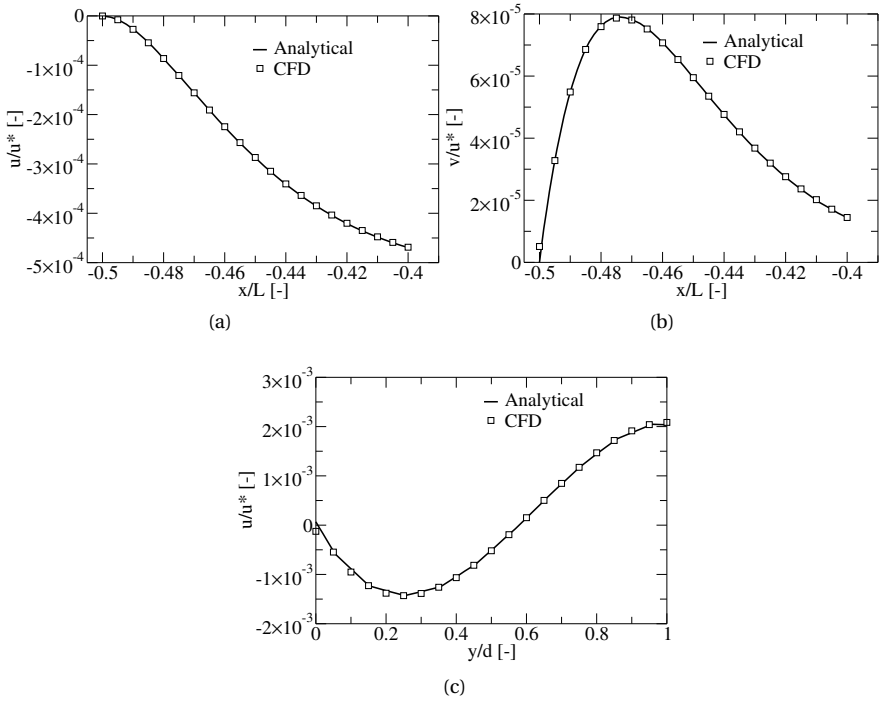

Figure 2.15: The profiles of the velocity components in the proximity of the side-wall extracted along the $y = d/2$ line (a), (b), and in the center of the cavity extracted along the $x = 0$ line (c): $Re^* = A, Ha^* = 1, Bo = A^2, Ca = A^4$.

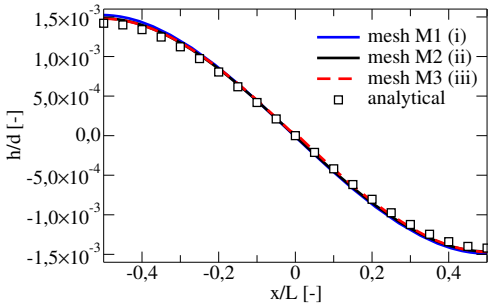

Figure 2.16: The mesh-dependency of the non-dimensional free-surface elevation (h/d) for $Re^* = A, Ha^* = 1, Bo = A^2, Ca = A^4$.

in both Ca^* and Bo^*. The horizontal profiles of the non-dimensional horizontal (u/u^*) and vertical (v/u^*) velocity in the proximity of the left-wall are shown in Figs.2.15a,b, respectively. The vertical profile of the non-dimensional horizontal velocity at the central vertical line is shown in Fig. 2.15 (c). Again, an excellent agreement between the present

simulation (CFD) and analytical solution from the literature ([10]) is obtained, proving the capability of the MHD multi-phase solver.

To confirm that the presented solutions are grid independent, we analyzed the non-dimensional free-surface elevation (h/d) for three mesh sizes: (i) the coarse mesh (M1) ($N_x \times N_y = 25 \times 100$), (ii) the intermediate (previously presented results) mesh (M2) ($N_x \times N_y = 50 \times 200$), and (iii) the fine mesh (M3) with ($N_x \times N_y = 100 \times 400$). A good agreement between results at different mesh resolutions confirms the full mesh convergence of the presented results, Fig. 2.16.

2.3.4. THE 3D RISING GAS BUBBLE IN LIQUID METAL SUBJECTED TO A LONGITUDINAL MAGNETIC FIELD

A rising gas bubble (with an initial diameter $d_b = L/2$) is submerged into the liquid metal confined in the 3D rectangular box (with height $3L$, width and depth L) is analyzed next, Fig. 2.17. This test case is based on the study of [11].

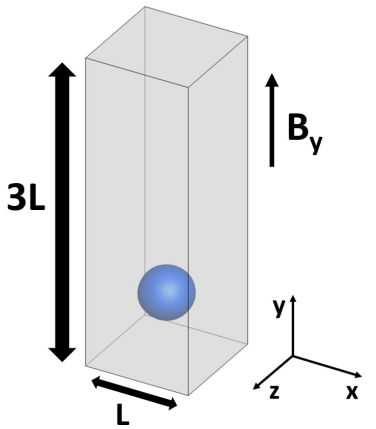

Figure 2.17: The sketch of the simulation domain for the rising bubble in a liquid metal subjected to an external (axial) magnetic field.

All boundary surfaces are electrically insulated walls ($\partial\phi/\partial n = 0, C_d = 0$) with imposed no-slip boundary conditions. The external magnetic field is aligned with the y-coordinate and the gravity is oriented in the opposite direction. The problem is fully defined with the following set of non-dimensional parameters:

$$G = \frac{g\rho_G^2 d_b^3}{\mu_G^2}, \quad \Gamma = \frac{\gamma \rho_G d}{\mu_G^2}, \quad Ha = B d_b \sqrt{\frac{\sigma_L}{\mu_L}} \tag{2.26}$$

where G is the Galilei number, Γ is the Tension number, and subscripts (G) and (L) indicate the gas and liquid phase, respectively. The non-dimensional velocity, pressure, and

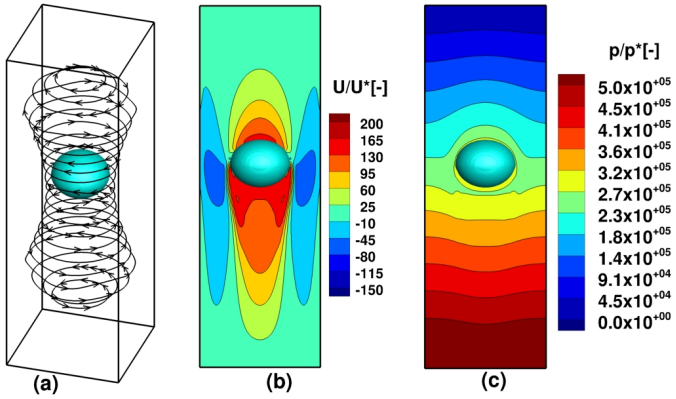

Figure 2.18: The bubble shape (extracted as the isosurface of the volume fraction $\alpha = 0.5$) with superimposed streamlines of the total current density (a), (b) contours of the non-dimensional vertical velocity (u_y/u^*) in the central vertical plane, (c) contours of the non-dimensional pressure field (p/p^*) in the central vertical plane - all at $t/t^* = 0.02$ and for $Ha = 50$.

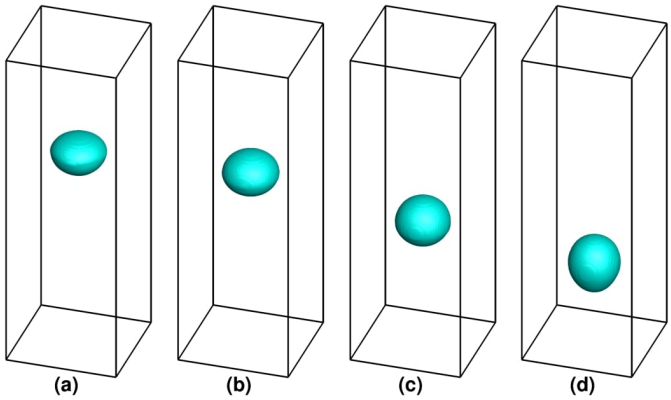

Figure 2.19: The bubble shape (identified as the isosurface of the volume fraction $\alpha = 0.5$) and its location at time instant $t/t^* = 0.025$ for various Ha: $Ha = 0, 50, 100, 200$ (a-d), respectively.

time are defined as:

$$u^* = \mu_G/(\rho_G d_b), \quad p^* = \mu_G^2/(\rho_G d_b^2), \quad t^* = \rho_G d^2/\mu_G \tag{2.27}$$

We kept constant $G = 4 \cdot 10^4$, $\Gamma = 2 \cdot 10^6$ and varied $0 \leq Ha \leq 200$ to study the influence of the magnetic field strength on the rising bubble behavior. The electrical conductivity ratio is $\sigma_G/\sigma_L = 2.49 \cdot 10^{-7}$. The orthogonal mesh is created with the mesh size ($N_x \times N_y \times N_z = 60 \times 180 \times 60$), identical to the mesh used in [11]. The second-order linear-upwind scheme is used for the convective terms in both momentum and volume fraction equations, whereas the backward scheme is used for time integration. Because of a sharp jump of the electrical properties at the phase interface, we have applied the

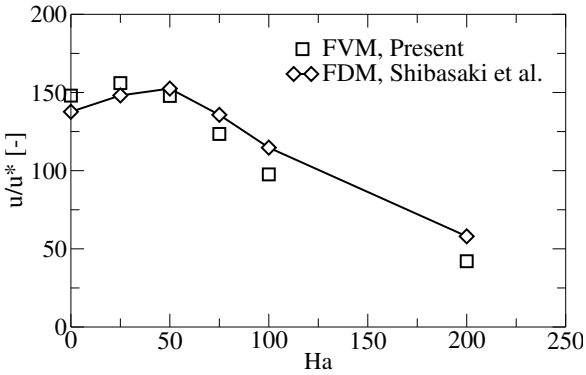

Figure 2.20: Terminal bubble velocity at various Ha. Comparison with the finite-difference (FDM) results of [11].

harmonic interpolation scheme for the electric conductivity. For this case, the interface compression coefficient (C_α) had a stronger effect on the final shape of the rising bubble. The selected value of $C_\alpha = 0.1$ proved to be a good choice for both multi-phase benchmarks presented here.

The obtained characteristic bubble shape, current density streamlines, contours of the vertical velocity, and pressure in the central vertical plane at an arbitrary time instant $t/t^* = 0.02$ and for $Ha = 50$, are shown in Fig. 2.18. The current density streamlines form close loops around the bubble with opposite directions above and below the bubble. The velocity contours portray an updraft region in the center of the domain - above and below the bubble, whereas the down-drafts are generated along the side-walls. Contours of the pressure exhibit almost linear distribution in the vertical direction, with small deviations in the proximity of the bubble surface. It can be seen that the resulting shape of the bubble strongly depends on the imposed magnetic field strength, Fig. 2.19. The higher Ha leads to the bubble stretching in the direction of the imposed magnetic field (y-direction) and to a reduction of its rising velocity. We compare our results with a numerical study of [11] who applied the finite-difference (FDM) multi-phase MHD code. Comparison of the computed terminal velocity for different values of Ha is shown in Fig. 2.20. After an initial slight increase in the terminal velocity for intermediate values of $Ha < 50$, a gradual decrease is obtained with a further increase of the imposed magnetic field. The agreement between the current simulations and data presented in [11] is good up to $Ha = 50$. After reaching this peak value, larger differences are observed, but qualitatively similar trends are observed. Differences for larger values of Ha number can be partially explained by the use of different discretization approaches (the present finite-volume vs. finite-difference of [11]), the application of different convective schemes (the present second-order linear-upwind vs. the third-order UTOPIA scheme of [11]), as well as due to the absence of the mesh-dependency study of [11]). We also performed additional simulations with a second-order quadratic-upwind scheme for convective terms

Table 2.2: The non-dimensional terminal velocity at $Ha = 50$ and $Ha = 200$ for different meshes. Comparisons with values presented in the finite-differences based method (FDM) of [11].

Ha	The non-dimensional terminal velocity, (u_y/u^*)	Present	Shibasaki et al.[11]
50	mesh (M1)	143.3	
	mesh (M2)	147.8	152
	mesh (M3)	149.9	
200	mesh (M1)	41.3	
	mesh (M2)	42.1	58
	mesh (M3)	42.5	

in momentum equations, but this resulted in marginal differences of rising velocity (less than 1%) compared to the linear-upwind scheme.

Finally, we complete a mesh-dependency study for two different Hartmann numbers Ha =50 and 200, and three meshes: (i) the coarse mesh (M1) (Nx × Ny × Nz = 30 × 90 × 30) = $(0.081 \times 10^6)_{\text{total}}$ CVs, (ii) the present mesh (M2) (Nx × Ny × Nz = 60 × 180 × 60) = $(0.64 \times 10^6)_{\text{total}}$ CVs and (iii) the fine mesh (M3) (Nx × Ny × Nz = 120 × 360 × 120) = $(5.1 \times 10^6)_{\text{total}}$ CVs. Results in Table. 2.2 demonstrate that the finest mesh (M3) provides the best agreement with the reference data. However, the difference in terminal velocity values between intermediate (M2) and fine (M3) mesh is only 1%, while the total number of CVs is four times larger. Based on this small difference, we conclude that results are grid independent already at the mesh (M2).

2.4. SUMMARY AND CONCLUSION

We have presented a comprehensive numerical benchmark study addressing a range of single- and multi-phase one-way coupled MHD flows. The single-phase cases included the conjugate MHD flows in ducts with varied electric conductivity of the wall, and the laminar back-step flow subjected to a transverse magnetic field. The multi-phase cases covered a two-dimensional MHD cavity and a rising bubble in a liquid metal flows - both simulated with the volume of fluid (VoF) approach. We have implemented an extended set of MHD transport equations in the open-source code OpenFOAM. Our particular focus was to extend the existing set of MHD benchmarks and to provide a detailed comparison with similar studies in the literature. For the multi-phase flows, we have introduced a recently proposed analytical solution of a two-dimensional partially-filled cavity flow subjected to an external magnetic field. An excellent agreement was obtained for all cases for which analytical solutions are available. For considered test cases without analytical solutions, a very good agreement was obtained with available numerical studies from the literature. It is concluded that here developed and validated version of the computer code can be used for advanced fundamental and industrial/technological studies

involving various aspects of the MHD phenomena.

REFERENCES

[1] J. Hartmann and F. Lazarus, *Theory of the laminar flow of an electrically conducting liquid in an homogeneous magnetic field,* Kongelige Danske Videnskabernes Selskab Matematisk **15**, 1 (1937).

[2] J. Shercliff, *Steady motion of conducting fluids in pipes under transverse magnetic fields,* Mathematical Proceedings of the Cambridge Philosophical Society **49**, 136 (1953).

[3] J. Feng, H. Chen, Q. He, and M. Ye, *Further validation of liquid metal MHD code for unstructured grid based on openfoam,* Fusion Engineering and Design **100**, 260 (2015).

[4] Z. Tao and M. Ni, *Benchmark solutions for MHD solver development,* Science China Physics, Mechanics and Astronomy **56**, 378 (2013).

[5] J. Walker, *Magnetohydrodynamic flow in rectangular ducts with thin conducting walls,* Journal de Mecanique **20**, 79 (1981).

[6] S. Smolentsev, S. Badia, R. Bhattacharyay, L. Bühler, L. Chen, Q. Huang, H.-G. Jin, D. Krasnov, D.-W. Lee, E. M. De Les Valls, *et al., An approach to verification and validation of MHD codes for fusion applications,* Fusion Engineering and Design **100**, 65 (2015).

[7] N. L. Gajbhiye, P. Throvagunta, and V. Eswaran, *Validation and verification of a robust 3-D MHD code,* Fusion Engineering and Design **128**, 7 (2018).

[8] A. Tassone, G. Caruso, A. Del Nevo, and I. Di Piazza, *CFD simulation of the magnetohydrodynamic flow inside the wcll breeding blanket module,* Fusion Engineering and Design **124**, 705 (2017).

[9] S. Sahu and R. Bhattacharyay, *Validation of comsol code for analyzing liquid metal magnetohydrodynamic flow,* Fusion Engineering and Design **127**, 151 (2018).

[10] B. Righolt, S. Kenjereš, R. Kalter, M. Tummers, and C. Kleijn, *Analytical solutions of one-way coupled magnetohydrodynamic free surface flow,* Applied Mathematical Modelling **40**, 2577 (2016).

[11] Y. Shibasaki, K. Ueno, and T. Tagawa, *Computation of a rising bubble in an enclosure filled with liquid metal under vertical magnetic fields,* ISIJ International **50**, 363 (2010).

[12] D. A. Hoang, V. van Steijn, L. M. Portela, M. T. Kreutzer, and C. R. Kleijn, *Benchmark numerical simulations of segmented two-phase flows in microchannels using the Volume of Fluid method,* Computers & Fluids **86**, 28 (2013).

[13] S. Mukherjee, A. Zarghami, C. Haringa, K. van As, S. Kenjereš, and H. E. Van den Akker, *Simulating liquid droplets: A quantitative assessment of lattice Boltzmann and Volume of Fluid methods,* International Journal of Heat and Fluid Flow **70**, 59 (2018).

[14] M.-J. Ni, R. Munipalli, N. B. Morley, P. Huang, and M. A. Abdou, *A current density conservative scheme for incompressible MHD flows at a low magnetic Reynolds number. Part I: On a rectangular collocated grid system,* Journal of Computational Physics **227**, 174 (2007).

[15] H. G. Weller, G. Tabor, H. Jasak, and C. Fureby, *A tensorial approach to computational continuum mechanics using object-oriented techniques,* Computers in Physics **12**, 620 (1998).

[16] R. I. Issa, A. Gosman, and A. Watkins, *The computation of compressible and incompressible recirculating flows by a non-iterative implicit scheme,* Journal of Computational Physics **62**, 66 (1986).

[17] J. Hunt, *Magnetohydrodynamic flow in rectangular ducts,* Journal of Fluid Mechanics **21**, 577 (1965).

[18] D. Sloan and P. Smith, *Magnetohydrodynamic flow in a rectangular pipe between conducting plates,* ZAMM-Journal of Applied Mathematics and Mechanics/Zeitschrift für Angewandte Mathematik und Mechanik **46**, 439 (1966).

[19] K. Mramor, R. Vertnik, and B. Šarler, *Simulation of laminar backward facing step flow under magnetic field with explicit local radial basis function collocation method,* Engineering Analysis with Boundary Elements **49**, 37 (2014).

3

THE TRANSITIONAL MAGNETOHYDRODYNAMIC FLOW IN AN ELECTRICALLY CONDUCTIVE SQUARE DUCT

We present results of a series of numerical simulations of an initially fully developed turbulent flow of a liquid metal in a long duct under the influence of a constant uniform transverse magnetic field and various wall conductances (ranging from perfectly insulated to perfectly conducting walls). The changes in the wall conductance caused the appearance of novel flow regimes characterized by the co-existence of locally turbulent/laminar flow regions and a non-monotonic behavior of the corresponding wall-friction coefficients. In contrast to the situation where an increase of the imposed magnetic field will lead to continuous suppression of turbulence and final complete relaminarization of the flow, in a specific range of wall-conducting parameters, we also observe an apparent partial and complete turbulence regeneration from the magnetohydrodynamic-suppressed laminar state.

Published as: A. Blishchik, S. Kenjereš, Observation of a novel flow regime caused by finite electric wall conductance in an initially turbulent magnetohydrodynamic duct flow. Physical Review E 104, L013101, 2021, doi: 10.1103/PhysRevE.104.L013101

3.1. INTRODUCTION

Starting from the pioneering theoretical and experimental studies of [1, 2], the Magnetohydrodynamic (MHD) interactions (i.e. interactions between the flow of an electrically conducting fluid (liquid metal, electrolyte, or plasma) and an imposed magnetic field) play an important role in numerous physical phenomena in nature and technology (e.g. origin of planetary magnetic fields, continuous casting, crystal growth, liquid-metal blankets in fusion reactors, etc., [3]). Despite the progress of various experimental techniques in classical fluid mechanics in recent years, MHD-related experiments are still very challenging, especially if the local multi-physics information is needed (e.g. simultaneous measurements of the instantaneous velocity and its gradients, pressure, electric potential, and total current density). Experimental difficulties are caused by the non-transparency of liquid metals, limited spatial and temporal resolution, as well as the inherently three-dimensional nature of interactions between the velocity and electromagnetic fields. Recent progress in the eddy-resolving numerical simulation techniques, such as Direct Numerical Simulation (DNS) and Large Eddy Simulation (LES) approach, have opened additional possibilities for analysis of complex MHD interactions, [4],[5]. The advanced numerical simulations of MHD phenomena can provide detailed insights into local reorganization of the flow, turbulence and corresponding electric potential and total current density, and their cross-correlations. The latter are notoriously difficult to get from the current experimental approaches, and of crucial importance for the development of the Reynolds-averaging based class of turbulence models suitable for practical industrial and technological applications, [6–8].

In the great majority of cases presented in the literature, the central focus of the MHD numerical research aims to determine the transient and turbulent flow characteristics in generic configurations such as pipe, duct, and channel flow, subjected to an external (uniform or partially imposed) magnetic field of different strength and orientation, where the walls are assumed to be perfectly electrically insulated or conducting, [9–13]. However, in practical conditions, one has also to deal with the finite thickness and electrical conductivity of surrounding walls, which can significantly alter the electric current behavior in the entire configuration. This alternation of electric current will affect the distributions of the Lorentz force, and consequently, the velocity components. The inclusion of surrounding walls with a finite thickness and electric conductivity is associated with numerous difficulties in both experimental and numerical studies. For experiments, multiple modular setups are required to study the influence of walls with various parameters. For simulations, advanced numerical solvers need to be developed, which can include also solid wall regions (in addition to the flow domain) for calculations of the electric current, and potential (so-called conjugate MHD phenomena). Although the distinct effects of finite wall thickness and electric wall conductivity on a laminar MHD flow were thoroughly investigated by Hunt [14], studies reporting on the effects of a wide range of aforementioned wall parameters on MHD turbulent flow are scarce in the literature. The impact of specific wall conductivity values in a combination with dif-

ferent magnetic field orientations on a laminar MHD duct flow was demonstrated in a numerical research of [15]. The formation of the M-shape velocity profile, typical to the duct flow with conductive walls, was observed. Effects of electrically conducting walls on rotating magnetoconvection were analyzed in numerical simulations of [16]. It was shown that initially oscillatory magnetoconvection can become steady when electrically conducting walls were imposed. The instabilities in an MHD duct flow with a constant wall conductivity were numerically and experimentally studied in [17], [18], respectively. The onset of instabilities and jet detachments were found in a good agreement between the experiments and simulations. In experimental studies of [19], measurements of the single- and multi-phase MHD flows in rectangular channels were performed. When one of the electrically insulated walls was replaced with a copper plate (finite conductance), a suppression of the turbulence intensity was observed. Numerical studies of the linear stability of fully developed MHD flow in a square duct with insulating Shercliff walls and thin electrically conducting Hartmann walls subjected to a uniform magnetic field were presented in [20]. The main conclusion was that the wall conductance ratio determined flow stabilization or destabilization - depending on the strength of the imposed magnetic field.

The main motivation of the present chapter is to fill an existing gap in the literature; we seek to provide a detailed insight into the effects of finite electric conductivity of surrounding walls on a turbulent MHD flow.

3.2. GOVERNING EQUATIONS AND NUMERICAL DETAILS

We consider a single-phase flow of an incompressible electrically conductive fluid in an initially fully developed turbulent regime, subjected to the homogeneous transverse magnetic field. Because of the magnetic Reynolds number $\mathrm{Re_m} = U \cdot D/\lambda << 1$ condition (where U is characteristic velocity, D is characteristic length-scale, and $\lambda = 1/\mu_0\sigma$ is the magnetic diffusivity), the one-way coupled MHD approach is used. The flow is described by conservation of mass, momentum, and Ohm's law for the moving media, respectively:

$$\nabla \cdot \mathbf{u} = 0 \tag{3.1}$$

$$\frac{\partial \mathbf{u}}{\partial t} + (\mathbf{u} \cdot \nabla)\mathbf{u} = -\frac{1}{\rho}\nabla p + \nu \nabla^2 \mathbf{u} + \frac{1}{\rho}\underbrace{(\mathbf{j} \times \mathbf{B})}_{\mathbf{F^L}} \tag{3.2}$$

$$\mathbf{j} = \sigma(-\nabla\phi + \mathbf{u} \times \mathbf{B}) \tag{3.3}$$

where $\mathbf{u}$ is velocity, p is pressure, $\mathbf{j}$ is current density, ϕ is the electric potential, $\mathbf{B}$ is the imposed magnetic field, $\mathbf{F^L}$ is Lorentz force, ν is kinematic viscosity, ρ is density, σ is electrical conductivity. By imposing the $\nabla \cdot \mathbf{j} = 0$, the Ohm's law reduces to a simple Poisson equation for the electric potential as:

$$\nabla^2\phi = \nabla \cdot (\mathbf{u} \times \mathbf{B}) \tag{3.4}$$

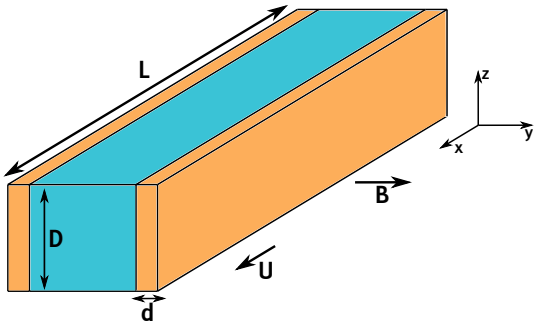

Figure 3.1: Sketch of the simulation domain for the conjugate MHD duct flow.

In contrast to the governing transport equations for mass and momentum, which are applied for the fluid domain, the electric potential equation needs to be extended as well to the surrounding walls of a finite thickness (d) and conductivity (σ_S). Note that the interface condition needs to be satisfied, i.e. $\phi_L = \phi_S$ and $\sigma_L \partial\phi_L/\partial n = \sigma_S \partial\phi_S/\partial n$, where L and S indicate liquid (fluid) and solid (wall) domains, respectively, and n is the wall-normal. The problem is fully defined by two characteristic non-dimensional parameters: Reynolds ($\mathrm{Re} = U \cdot D/\nu$) and Hartmann ($\mathrm{Ha} = B \cdot D\sqrt{\sigma/\rho\nu}$) numbers.

To be able to simultaneously solve the distribution of governing parameters (ϕ and $\mathbf{j}$) in both fluid and wall regions, as well to conserve the current density, we have developed the integrated conjugate MHD solver by combining the Four Steps Projection Method (FSPM), proposed in [21], and the grid-coupling approach to match the fluid and wall regions. A finite-volume in-house code based on the open-source OpenFOAM-Extend is applied to solve a discretized form of the transport equations, Eqn. (3.3 - 3.4). The second-order central differencing scheme (CDS) is applied for both diffusive and convective terms, while the time-integration is performed by the second-order backward scheme. For additional numerical details, see [22].

All simulations are performed for the configuration shown in Fig. 3.1. We analyze the turbulent flow of an electrically conducting fluid (σ_L) in a long duct (L = 40 D) with a square cross-section (D×D), surrounded by two walls with a finite thickness (d/D = 0.05), and an arbitrary electric conductivity (σ_S). The remaining upper- and lower-walls (Shercliff walls), parallel to the imposed magnetic field, are electrically insulated. At all walls, the no-slip velocity boundary condition is imposed. The flow is driven by the imposed pressure gradient in the streamwise x-direction (periodic boundary condition), whereas the uniform magnetic field is imposed in the transverse y-direction. The left- and right-surrounding walls (Hartmann walls), perpendicular to the imposed magnetic field, are characterized by a finite thickness and an arbitrary electric conductivity. These wall characteristics are incorporated into a single wall conductance ratio parameter, defined as $C_d = (\sigma_\mathrm{S} \cdot \mathrm{d}) / (\sigma_\mathrm{L} \cdot \mathrm{D})$. In the present study, we covered an extensive range of the wall conductance parameter, i.e. $0 \leq C_d < \infty$, where $C_d = 0$ indicates fully electrically

insulating walls, and $C_d \rightarrow \infty$ indicates the fully electrically conducting walls, respectively. For these two cases, boundary conditions for the electric potential are defined as: (i) $\partial\phi/\partial y = 0$ at y = 0 and y = D; $\partial\phi/\partial z = 0$ at z = 0 and z = D for perfectly electrically insulated walls (all walls); (ii) $\phi = 0$ at y = 0 and y = D for perfectly conducting (side) walls.

We apply the wall-resolving dynamic large-eddy simulation (LES) approach to capture the instantaneous turbulence structures. It serves as the best compromise between accuracy in capturing the instantaneous flow physics, and the total computational costs (in comparison to the fully resolving direct-numerical simulations (DNS),[23, 24]). The dynamic LES adopted here automatically takes into account the local effects of the Lorentz force generated, through local adjustment of the Smagorinsky coefficient,[4, 8]. The numerical mesh contains $(N_x \times N_y \times N_z = 720 \times 80 \times 80)_{\text{fluid}}$ and $(N_x \times N_y \times N_z = 720 \times 12 \times 80)_{\text{wall}}$ non-uniformly distributed control volumes in the fluid and wall regions, respectively. Special attention is devoted to having a proper resolution of boundary layers along the surrounding walls for all flow regimes. The Hartmann and Shercliff layer criteria (with a typical thickness of $\delta_{Ha} = D/Ha$ and $\delta_{Sh} = D/Ha^{1/2}$) have been accomplished with 10 points in the Hartmann layer and 25 points in the Shercliff layer. These criteria correspond to $\Delta[y,z]^{+}_{wall} < 1$.

3.3. RESULTS AND DISCUSSION

We start our analysis by validating the dynamic LES approach adopted here against the fully resolved direct numerical simulation (DNS) results for a non-MHD duct flow (Ha = 0, [25]) and an MHD duct flow with perfectly electrically insulating walls ($C_d = 0$, Ha = 21.1, [10]) - both in a fully developed turbulent regime at $Re = 5602$. The profiles obtained for the long-term time-averaged streamwise velocity fluctuations and the mean streamwise velocity component (characteristic log-law distributions) are shown in Fig. 3.2. For both the non-MHD ($Ha = 0$) and MHD cases ($Ha = 21.1$), predicted profiles are in very good agreement with DNS results from the literature. Characteristic peak values in the proximity of walls are properly captured, as well as the entire distribution towards the duct center - confirming the accuracy of the adopted simulation approach. Next, we move to perform a series of simulations by changing the wall-conductance ratio parameter (C_d) over an extensive range of values, varying from the electrically insulated to the perfectly electrically conducting walls, i.e. $0 \leq C_d < \infty$. All remaining flow parameters (Re and Ha) are kept unchanged.

The first distinct feature of the profiles of the non-dimensional streamwise fluctuating velocity is their peculiar non-monotonic behavior, Fig. 3.2. The characteristic peak values in the proximity of the duct walls are observed for the non-MHD case, with fully symmetric distributions along the Shercliff and Hartmann walls. Activation of the magnetic field, with fully electrically insulated walls ($C_d = 0$), leads to small suppression of the peak value in the proximity of the Shercliff wall, and a significant suppression in the proximity of the Hartmann wall. By slightly increasing the wall conductivity ($C_d = 0.05$),

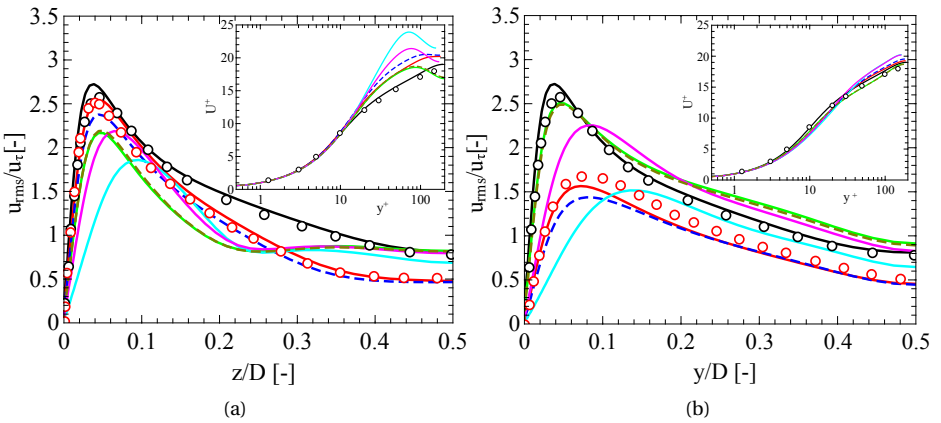

Figure 3.2: Comparison of the present dynamic LES and DNS results from the literature for a non-MHD ((○) - $Ha = 0$, [25]) and MHD ((○) - $Ha = 21.2$, $C_d = 0$, [10]): (a) the vertical profiles in the proximity of the Shercliff walls, (b) the horizontal profiles in the proximity of the Hartmann walls of the non-dimensional streamwise velocity fluctuations (u_{rms}). The zoom-ins show the log-law distribution of the mean streamwise velocity component. The present dynamic LES is indicated as follows: (——) - $Ha = 0$; (——) - Ha = 21.2, $C_d = 0$; (– –) - Ha = 21.2, $C_d = 0.05$; (——) - Ha = 21.2, $C_d = 0.25$; (——) - Ha = 21.2, $C_d = 0.5$; (– –) - Ha = 21.2, $C_d = 5$; (——) - Ha = 21.2, $C_d \to \infty$.

a small suppression of the peak values is observed in the proximity of both Hartmann and Shercliff walls, whereas the values in the duct center are unaffected. With $C_d = 0.25$, suppression of the peak value is obtained in the proximity of the Shercliff walls. The location of the peak is shifted farther from the wall (i.e. at z/L = 0.1), and the value in the center of the duct significantly increased, Fig. 3.2(a). In contrast to this behavior (for the same $C_d = 0.25$), the profile of streamwise velocity fluctuation in the vicinity of the Hartmann wall produced a peak value above that of $C_d = 0.05$, which is now shifted towards the duct center, with higher values also in the central part of the duct, Fig. 3.2(b). For $C_d = 0.5$, a remarkable increase is observed at both locations. The value at the duct center reaches identical values as for the non-MHD case (i.e. $Ha = 0$). For $C_d = 5$, a less dramatic reorganization is taking place, characterized by the movement of the peak location closer to the walls, whereas the values in the duct center remain unaffected. With a further increase of $C_d \to \infty$, there are no visible additional changes in the profiles at both locations, indicating that a saturation point was reached.

To provide additional insights in this remarkable non-monotonic behavior of the streamwise velocity fluctuations, we calculate the skin friction coefficients $C_f = \tau / \left(0.5\rho U^2\right)$ at the Hartmann and Shercliff walls over a wide range of C_d, Fig. 3.3. Starting from a fully developed turbulent (T) state at $Ha = 0$, activation of the uniform transverse magnetic field at $Ha = 21.2$ with perfectly electrically insulating walls ($C_d = 0$), generates suppression of C_f at the Shercliff walls and an enhancement at the Hartmann walls.

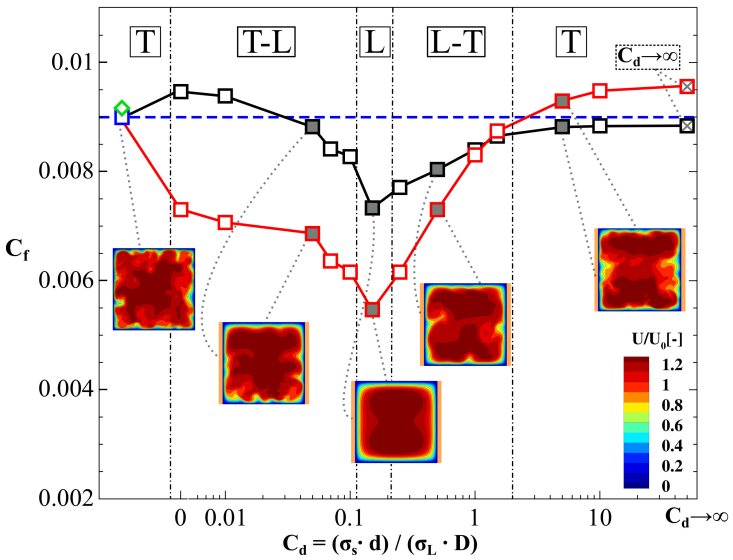

Figure 3.3: Dependency of the friction coefficient (C_f) at the Shercliff (□) and Hartmann (□) duct walls on the wall-conductance parameter (C_d) for fixed Re = 5602 and Ha = 21.2. One representative of each characteristic flow regime are selected: (T) - fully turbulent, (T-L) - turbulent to laminar transition, (L) - fully laminar, (L-T) - laminar to turbulent transition, respectively. In the current plot, the value of C_f at $C_d \rightarrow \infty$ regime has been assigned to a finite value of C_d instead of infinity. Furthermore, we indicate C_f values for the non-MHD case (Ha=0): (□ – –) -present study, (◇) - experimental correlation of [26].

With a further increase of the wall conductivity, a gradual reduction in C_f is observed for both Hartmann and Shercliff walls (up to $C_d = 0.05$). After reaching $C_d = 0.05$, a more rapid suppression occurs for both walls, resulting in local minimum values in the $0.1 \leq C_d \leq 0.2$) range. The plots of the instantaneous streamwise velocity contours portray a stable fully symmetrical distribution without any traces of the locally occurring intermittency, indicating a complete re-laminarization (L) of the flow, Fig. 3.3. After reaching $C_d > 0.2$, both friction coefficients start to increase. Analysis of the instantaneous streamwise velocity contours confirms the re-appearance of the intermittent flow features. The slope of the C_f for the Shercliff walls is much steeper compared to the Hartmann walls, resulting in a characteristic cross-over at approximately $C_d = 1$. For $C_d > 1$, the friction coefficient at the Shercliff walls takes over its counterpart along the Hartmann walls and a fully recovered turbulent state is present. Additional cross-over can be observed at $C_d = 5$ where the C_f along the Shercliff walls reaches the C_f of the non-MHD case. After $C_d = 5$, characteristic slopes are much less steep, indicating convergence towards the final asymptotic states. The values of C_f when $C_d \rightarrow \infty$, show an increase compared to the neutral non-MHD (Ha = 0) case for the Shercliff walls. In contrast to the Shercliff walls, C_f for the Hartmann walls reaches values close to the neu-

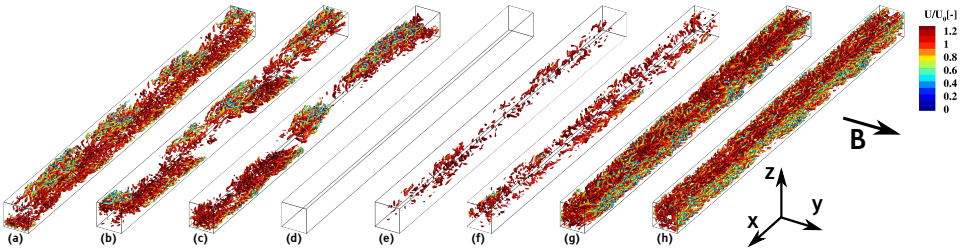

Figure 3.4: The instantaneous coherent structures in the MHD duct flow identified as isosurfaces of the second-invariant of the velocity-gradient tensor (Q-criterion, Q=1 s^{-2}), colored with the streamwise velocity at Re=5602 and Ha=21.2: (a) $C_d = 0$, (b) $C_d = 0.05$, (c) $C_d = 0.1$, (d) $C_d = 0.15$, (e) $C_d = 0.25$, (f) $C_d = 0.5$, (g) $C_d = 1.5$, (h) $C_d \to \infty$.

tral case. It can be concluded that C_f behavior along the Hartmann and Shercliff walls portrays complex behavior indicating a significant flow and turbulence reorganization. Starting from a fully developed turbulent flow regime for the neutral non-MHD case, by changing solely the wall-conductance, the partial or complete re-laminarization can be observed, followed by a rapid recovery of the intermittent states. Finally, for the $C_d \to \infty$, the fully developed turbulence is recovered. Both of the previously analyzed quantities - the friction coefficients along the walls (Fig. 3.3) and profiles of the RMS of the streamwise fluctuations (Fig. 3.2)- are long-term time-averaged quantities. We also partially addressed some of the instantaneous flow features by plotting contours of the streamwise velocity in the characteristic central plane (inserts of Fig. 3.3).

To provide detailed insights into a full three-dimensional flow and turbulence structures, we calculate the second-invariant of the velocity-gradient tensor parameter (so-called Q-criterion), and apply this criterion to identify instantaneous features over a wide range of $0 \leq C_d < \infty$, Fig. 3.4. The plots reveal a very dense population of the coherent structures in the proximity of the Shercliff walls at the $C_d = 0$, Fig. 3.4(a). By changing the wall conductivity ($C_d = 0.05$ and $C_d = 0.1$) a distinct clustering of the coherent structures along the Shercliff walls is observed with a clear reduction of their spatial extent in the streamwise direction, Figs. 3.4(b) and (c). These distributions of the coherent structures exhibit similar patterns (patterned turbulence) as previously observed in standard MHD channels with electrically insulated walls ($C_d = 0$) when the strength of the imposed magnetic field is increased, [12]. At $C_d = 0.15$, there is total suppression of the coherent structures, confirming full re-laminarization of the flow, Fig. 3.4(d). For $C_d = 0.25$, re-appearance of coherent structures in the central part of the duct takes place, confirming localized turbulence production, Fig. 3.4(e). By further increasing $C_d = 0.5$, the coherent structures start to occupy regions closer to the Shercliff walls, Fig. 3.4(f). This trend continues for higher values of $C_d = 1.5$, where coherent structures are rapidly expanding towards the wall regions (in both directions), producing even more dense distributions compared to the $C_d = 0$ case, Figs. 3.4(g) and (a). It should be noted that this is the range

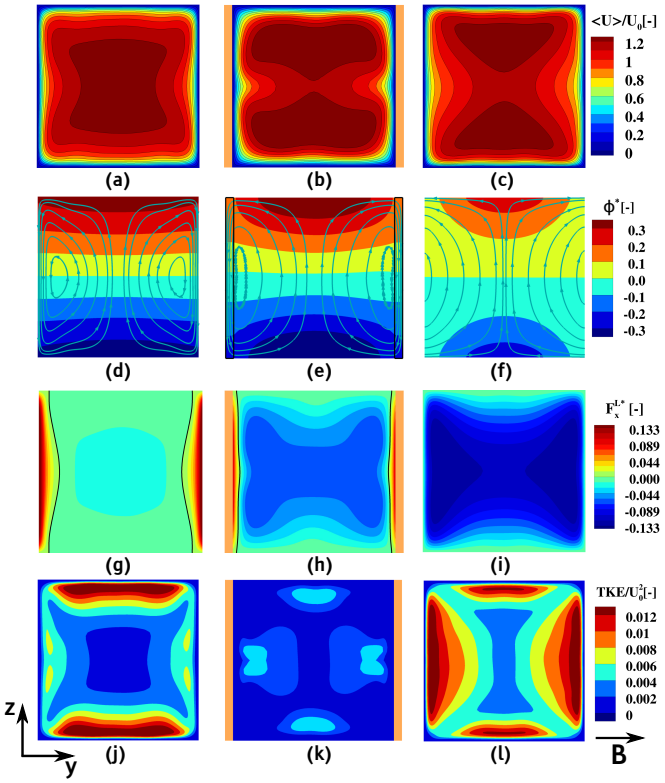

Figure 3.5: Contours of the long-term time-averaged streamwise velocity (a-b-c), non-dimensional electric potential ($\phi^* = \phi/U_0BD$) with iso-lines of electric current (d-e-f), the streamwise component of the non-dimensional Lorentz force ($F_x^{L*} = F_x^L/\sigma U_0 B^2$) (g-h-i), and non-dimensional turbulent kinetic energy (TKE = $0.5\overline{u_i'^2}/U_0^2$) (j-k-l) in the central vertical plane (x/L = 20), for the fixed Re=5602, H=21,2, and various wall conductances: $C_d = 0$ (-first column), $C_d = 0.25$ (-second column) and $C_d \to \infty$ (-third column).

of C_d where C_f plots indicate a cross-over between the Hartmann and Shercliff walls, Fig. 3.3. There are no significant differences in coherent structure distributions between $C_d = 1.5$ (Fig. 3.4(g)) and the case with perfectly conducting walls, $C_d \to \infty$ (Fig. 3.4(h)).

To provide a possible origin of the observed changes of flow regimes - from initially fully turbulent, then partial and complete relaminarization, and finally, return to fully recovered turbulence - we next analyze complex mechanisms along the following flow/electromagnetic field interaction pathways: $\left[\mathbf{u} \xrightarrow{\times \mathbf{B}} \nabla\phi \to \mathbf{e} \to \mathbf{j} \xrightarrow{\times \mathbf{B}} \mathbf{F^L} \to \mathbf{u}\right]$ (where $\mathbf{e}$ is the generated electric field). We plot contours of the mean streamwise velocity, electric potential, total current density, as well as resulting streamwise Lorentz force and turbulent kinetic energy - all in the central vertical plane (L = 20 D), Fig. 3.5. For the fully insulated walls ($C_d = 0$), the mean streamwise velocity contours show a clear sup-

pression along the central horizontal line, Fig. 3.5(a). The electric potential exhibits a nearly linear distribution in the vertical direction, Fig. 3.5(d). The total current streamlines form characteristic double loops which are closed within the fluid domain, with the highest density in the proximity of the Hartmann walls, Fig. 3.5(d). These regions coincide with locations where the horizontal Lorentz force is highest, Fig. 3.5(g), due to mutual perpendicular orientation between the total current and imposed magnetic field (note that the solid black line indicates the zero value of the F_x^{L*}) resulting in a significant reduction of turbulence here, Fig. 3.5(j). In contrast to this behavior, in the proximity of the Shercliff walls, the Lorentz force is much weaker, and the resulting turbulent kinetic energy is almost unaffected in comparison to the non-MHD case. The imprints of the generated Lorentz force on the mean streamwise velocity are shown in Fig. 3.5(a), where a transition from a full diagonal symmetrical distribution (for the non-MHD case) towards symmetry along the central vertical line is obtained. By replacing the fully insulated Hartmann walls with walls with the finite conductance ($C_d = 0.25$), different distributions of the mean velocity are obtained, showing two distinct regions aligned with the Shercliff walls, Fig. 3.5(b). Note that the selected value of $C_d = 0.25$ is for the case for which a local turbulence reoccurrence happens (as illustrated in Fig. 3.4(e)). The total current streamlines are now entering the sidewalls and electric potential starts to increase gradients in the corner regions, Fig. 3.5(e). The resulting positive streamwise Lorentz force is confined within much thinner Hartmann boundary layers, while the significant negative Lorentz force is generated in the duct center, Fig. 3.5(h). The regions with the positive streamwise Lorentz force disappear entirely for $C_d \to \infty$, Fig. 3.5(i). The strong shear originating from the 'M-shaped' velocity profiles re-introduces the turbulence seed-regions farther away from the boundary layer regions, generating the four distinct islands of the elevated turbulence, Fig. 3.5(k). With further increase of C_d, these regions expand toward walls, producing final ($C_d \to \infty$) turbulence distribution as shown in Fig. 3.5(l). In contrast to $C_d = 0$ case (Fig. 3.5(j), the turbulence along the Hartmann walls is augmented - in both intensity and area that occupies. The turbulence along the Shercliff walls now covers a significantly smaller area, Fig. 3.5(l). Despite this locally enhanced turbulence region the friction coefficient (C_f) along the Hartmann walls is smaller than along the Shercliff walls, Fig. 3.3. This confirms that the observed non-monotonic changes in the friction coefficients along the Hartmann and Shercliff walls are the result of combined effects of the generation of the distinct wall-jet regions in the proximity of the Shercliff walls (i.e. M-shaped mean streamwise velocity profiles) and turbulence reorganization. Our argument that the combined effects are responsible for the observed novel regimes are also supported by the fact that a monotonic behavior of the friction coefficient versus wall-conductance dependency (i.e. continuously increasing for the Shercliff walls and continuously decreasing for the Hartmann walls) is obtained for the laminar MHD duct cases with changing wall conductance in the $0 \leq C_d < \infty$ range, [22].

3.4. SUMMARY AND CONCLUSION

In summary, we numerically investigated the influence of varying the electric conductance of surrounding duct walls on the initially fully developed turbulence subjected to a transverse constant uniform magnetic field. We analyzed the instantaneous and long-term time-averaged features of the flow, turbulence, electric potential, total current density, and resulting Lorentz force. The instantaneous coherent structures portray distinct regimes characterized by a co-existence of the turbulent and laminar flow regimes, a complete relaminarization, as well as a partial and complete turbulence regeneration. This non-monotonic behavior was also reflected in the distributions of the friction coefficients along the Hartmann and Shercliff walls. The initially higher values of C_f along the Hartmann walls and lover values along the Shercliff walls for $C_d = 0$ are inverted for $C_d \to \infty$. The characteristic cross-over occurred when $C_d \approx 1$. This behavior is explained in terms of the combined reorganization of the main flow (wall jets) and local turbulence. The presented results can be directly applicable for the electromagnetic braking in continuous casting of liquid steel and design of the liquid metal blankets in a new generation of fusion reactors. Finally, with the present study, we would like to motivate a new generation of the MHD experiments in generic configurations based on here presented working conditions.

REFERENCES

[1] J. Hartmann and F. Lazarus, *Hg-dynamics ii,* Theory of laminar flow of electrically conductive Liquids in a Homogeneous Magnetic Field **15** (1937).

[2] J. Hartmann and F. Lazarus, *Hg-dynamics ii,* Theory of laminar flow of electrically conductive Liquids in a Homogeneous Magnetic Field **15** (1937).

[3] P. A. Davidson, *An introduction to magnetohydrodynamics*, Cambridge Texts in Applied Mathematics (Cambridge University Press, 2001).

[4] B. Knaepen and R. Moreau, *Magnetohydrodynamic turbulence at low magnetic Reynolds number,* Annu. Rev. Fluid Mech. **40**, 25 (2008).

[5] O. Zikanov, D. Krasnov, T. Boeck, A. Thess, and M. Rossi, *Laminar-turbulent transition in magnetohydrodynamic duct, pipe, and channel flows,* Applied Mechanics Reviews **66** (2014).

[6] A. Yoshizawa, *Hydrodynamic and Magnetohydrodynamic Turbulent Flows: Modelling and Statistical Theory*, Vol. 48 (Springer Science & Business Media, 2013).

[7] S. Kenjereš, K. Hanjalić, and D. Bal, *A direct-numerical-simulation-based second-moment closure for turbulent magnetohydrodynamic flows,* Physics of Fluids **16**, 1229 (2004).

[8] S. Kenjereš, *On modeling and eddy-resolving simulations of flow, turbulence, mixing and heat transfer of electrically conducting and magnetizing fluids: A review,* International Journal of Heat and Fluid Flow **73**, 270 (2018).

[9] D. Krasnov, O. Zikanov, J. Schumacher, and T. Boeck, *Magnetohydrodynamic turbulence in a channel with spanwise magnetic field,* Physics of Fluids **20**, 095105 (2008).

[10] R. Chaudhary, S. Vanka, and B. Thomas, *Direct numerical simulations of magnetic field effects on turbulent flow in a square duct,* Physics of Fluids **22**, 075102 (2010).

[11] D. Krasnov, O. Zikanov, and T. Boeck, *Numerical study of magnetohydrodynamic duct flow at high Reynolds and Hartmann numbers,* Journal of Fluid Mechanics **704**, 421 (2012).

[12] D. Krasnov, A. Thess, T. Boeck, Y. Zhao, and O. Zikanov, *Patterned turbulence in liquid metal flow: Computational reconstruction of the Hartmann experiment,* Physical review letters **110**, 084501 (2013).

[13] O. Zikanov, D. Krasnov, T. Boeck, and S. Sukoriansky, *Decay of turbulence in a liquid metal duct flow with transverse magnetic field,* Journal of Fluid Mechanics **867**, 661 (2019).

[14] J. Hunt, *Magnetohydrodynamic flow in rectangular ducts,* Journal of Fluid Mechanics **21**, 577 (1965).

[15] A. Sterl, *Numerical simulation of liquid-metal MHD flows in rectangular ducts,* Journal of Fluid Mechanics **216**, 161 (1990).

[16] K. Zhang, M. Weeks, and P. Roberts, *Effect of electrically conducting walls on rotating magnetoconvection,* Physics of Fluids **16**, 2023 (2004).

[17] T. Arlt and L. Bühler, *Numerical simulations of time-dependent Hunt flows with finite wall conductivity,* Magnetohydrodynamics (0024-998X) **55** (2019).

[18] L. Bühler, T. Arlt, T. Boeck, L. Braiden, V. Chowdhury, D. Krasnov, C. Mistrangelo, S. Molokov, and J. Priede, *Magnetically induced instabilities in duct flows,* IOP Conference Series: Materials Science and Engineering **228**, 012003 (2017).

[19] S. Eckert, *Technical University of Dresden*, Ph.D. thesis, Technical University of Dresden (1998).

[20] T. Arlt, J. Priede, and L. Bühler, *The effect of finite-conductivity Hartmann walls on the linear stability of hunt's flow,* Journal of Fluid Mechanics **822**, 880 (2017).

[21] M.-J. Ni, R. Munipalli, N. B. Morley, P. Huang, and M. A. Abdou, *A current density conservative scheme for incompressible MHD flows at a low magnetic Reynolds number. Part I: On a rectangular collocated grid system,* Journal of Computational Physics **227**, 174 (2007).

[22] A. Blishchik, M. van der Lans, and S. Kenjereš, *An extensive numerical benchmark of the various magnetohydrodynamic flows,* International Journal of Heat and Fluid Flow **90**, 108800 (2021).

[23] D. K. Lilly, *A proposed modification of the Germano subgrid-scale closure method,* Physics of Fluids A: Fluid Dynamics **4**, 633 (1992).

[24] S. B. Pope, *Ten questions concerning the large-eddy simulation of turbulent flows,* New Journal of Physics **6**, 35 (2004).

[25] S. Gavrilakis, *Numerical simulation of low-Reynolds-number turbulent flow through a straight square duct,* Journal of Fluid Mechanics **244**, 101 (1992).

[26] O. Jones, *An improvement in the calculation of turbulent friction in rectangular ducts,* Journal of Fluids Engineering **98**, 173 (1976).

4

TURBULENCE SUPPRESSION AND REGENERATION IN A MAGNETOHYDRODYNAMIC DUCT FLOW

In the current chapter, we present a series of numerical simulations describing a turbulent magnetohydrodynamic (MHD) flow subjected to a transverse magnetic field in a square duct with arbitrary electrically conductive walls. The characteristic flow and electromagnetic non-dimensional parameters (Reynolds and Hartmann number, respectively) were fixed, while the wall conductivity ratio (C_d) was varied from the perfectly electrically insulated ($C_d = 0$) to perfectly electrically conducting ($C_d \to \infty$). The obtained results confirmed a significant impact of the conductivity of the surrounding walls on the flow and turbulence reorganization. We have observed that the initially fully developed turbulence regime was gradually suppressed in the $0 \leq C_d < 0.15$ range, while the fully laminarized state was obtained at $C_d = 0.15$. We found that the process of turbulence suppression was accompanied by the appearance of the patterned turbulence phenomenon in the proximity of the walls parallel to the magnetic field direction. With a further increase of the wall conductivity parameter ($0.15 < C_d < \infty$), we have observed a complete turbulence regeneration. We found that this turbulence regeneration was caused by the local reorganization of the total current density loops near the electrically conducting walls.

Published as: A. Blishchik, S. Kenjereš, Turbulence suppression and regeneration in a magnetohydrodynamic duct flow due to influence of arbitrary electrically conductive walls, Physics of Fluids 34, 045101, 2022, doi:10.1063/5.0084442

4.1. INTRODUCTION

Starting from the pioneering works of Hartmann [1] and Alfvén [2], the research field of magnetohydrodynamics (MHD), which addresses interactions between the flow of an electrically conducting fluid and imposed magnetic field, significantly advanced in various fields of the fundamental (plasma) physics and technological applications such as: a new generation of fusion reactors [3–5], continuous casting [6, 7], microfluidic systems [8–10], etc. The majority of the MHD turbulence-related studies presented in the literature addressed relatively simple flow geometries including the plane channels, pipes, or ducts [11]. However, the experimental studies of the MHD turbulence are associated with numerous difficulties due to the non-transparent nature of the working fluids characterized by high electrical conductivity (e.g. liquid metals), which requires novel measuring techniques. Additional challenges regarding experimental studies are associated with the potentially high temperatures (continuous casting), and suitable magnetic field generators able to provide sufficiently strong magnetic fields. These experimental challenges can be easily removed in numerical studies of the MHD phenomena. However, the numerical studies need to be based on the specific additional pre-requirements for the MHD extended Navier-Stokes solver. This includes the conservative form of the pressure and Lorentz force terms in the momentum equation, and the divergence-free conditions of the magnetic induction and total current density, respectively. Furthermore, the proper treatment of the MHD turbulence needs to be performed [12, 13].

To begin with the Reynolds-Averaged Navier-Stokes (RANS) turbulence modeling approach, additional MHD extensions of the two-equations eddy-viscosity based models were proposed [14]. The proposed model was able to correctly describe the turbulence suppression due to imposed magnetic field. The one-equation RANS turbulence model for quasi-two-dimensional turbulent MHD flow was presented by Smolentsev et al. [15]. The modified variant of the $k-\omega$ SST turbulence model with additional MHD anisotropy parameter [16] was presented by Miao et al. [17], and applied for simulations of the continuous casting. The full second-moment Reynolds-stress turbulence closure with MHD extensions was presented by Kenjereš et al. [18]. The model performances were studied in simulating turbulent channel flows subjected to external magnetic fields of different orientations. A good agreement with available DNS and experimental data was obtained over an extended range of Reynolds and Hartmann numbers.

In recent years, impressive progress was made in applying the high-fidelity eddy-resolving simulations (DNS and LES) of the MHD turbulence. Different subgrid closures (SGS) were tested in LES simulations of the turbulent MHD channel flow [19]. The dynamic Smagorinsky and originally developed coherent structures based SGS models demonstrated their accuracy and numerical robustness. A combined DNS/LES study was performed by Krasnov et al. [20] where the impact of the uniform spanwise oriented magnetic field on the turbulent MHD channel flow was analyzed. The increased strength of the imposed magnetic field reduced velocity fluctuations, and finally have produced the full flow laminarization. The DNS study of the turbulent MHD duct was conducted

by Chaudhary et al. [21]. It was observed that the stronger suppression of the turbulence occurred in the proximity of the side walls perpendicular to the imposed magnetic field. Krasnov et al. [22] performed the DNS simulations of the turbulent MHD duct flow at very high Reynolds numbers and found a relatively wide range of Hartmann numbers for which the flow was neither fully laminar nor fully turbulent, but with a distinct laminar core. This coexistence of the laminar and turbulent parts of the flow (patterned turbulence) was also addressed in DNS studies of evolving MHD duct and pipe flows by Krasnov et al. [23] and Zikanov et al. [24]. It was demonstrated that using a sufficiently long computational domain was crucial in reproducing the patterned turbulence patterns. The decay of the honeycomb-generated turbulence in a duct due to influence of the imposed transverse magnetic field was studied by Zikanov et al. [25]. The paradoxical observation of the high-amplitude velocity fluctuations was explained in terms of the large-scale quasi-two-dimensional flow structures forming, which survived the magnetic suppression. Compressible MHD turbulence was studied by Yang et al. [26]. The authors investigated which turbulence theories proposed for the incompressible cases would be also valid for compressible cases. An alternative approach to simulate magnetohydrodynamic flows, namely the one-stage simplified lattice Boltzmann method, was proposed by De Rosis et al. [27]. The accuracy and computational efficiency of this method were demonstrated, making it a good alternative approach for predicting MHD flows.

Despite this extensive number of the numerical studies in the literature dealing with the turbulent MHD flows, the prevailing majority of the considered cases were with electrically insulated surrounding walls. However, it was recognized that a significant flow reorganization can be generated when the electrically insulated walls were replaced with the walls of a finite electrical conductance [28]. The laminar MHD duct flow with arbitrary electrically conducting walls was numerically simulated by Sterl [29], and generation of the M-shaped velocity profile was reported. The linear stability analysis of the MHD duct flow was performed by Arlt et al. [30], and a strong dependency between the flow instabilities and imposed Hartmann walls conductance ratio was found. The MHD duct flows in laminar and turbulent flow regimes at various Hartmann numbers and with a constant value of the wall conductance were presented by Thomas et al. [31]. The onset of the flow instabilities was investigated and a good agreement between simulations and experiments [32] was obtained. Besides the channel and duct flows, effects of the various wall conductances were also analyzed in different configurations. Effects of the electrically conducting walls on the rotating magnetoconvection were analyzed by Zhang et al.[33]. When electrically insulated walls were replaced by the walls of finite conductivity, the flow oscillations were suppressed. The MHD mixed convection in micro-channels with one electrically conducting and one electrically insulated wall was analyzed by Akinshilo [34]. It was concluded that an increase in the radiation parameter produced a temperature decrease, with a stronger effect taking place near the electrically conducting wall.

In the present chapter, we focus on filling the existing gap in the literature dealing with a systematic investigation of effects of the finite electrical conductivity of the side walls in the initially fully developed turbulent flow regime in a square duct. The present contribution is a significantly extended version of our initial findings [35].

4.2. GOVERNING EQUATIONS AND NUMERICAL DETAILS

4.2.1. ONE-WAY COUPLED MHD FLOW AND TURBULENCE MODELING

In the present chapter, a turbulent flow of an incompressible electrically conductive fluid is considered. The fluid is subjected to an external uniform magnetic field (constant in time), which results in the generation of the active Lorentz force. The conservation laws of the mass and momentum can be formulated as:

$$\frac{\partial u_i}{\partial x_i} = 0 \tag{4.1}$$

$$\frac{\partial u_i}{\partial t} + u_j \frac{\partial u_i}{\partial x_j} = -\frac{1}{\rho}\frac{\partial p}{\partial x_i} + \nu \frac{\partial^2 u_i}{\partial x_j^2} + \frac{1}{\rho} F_i^L \tag{4.2}$$

where u_i is velocity, p is pressure, ν is the kinematic viscosity, ρ is density, and $F_i^L = \epsilon_{ijk} J_j B_k$ is the resulting Lorentz force (where J_j is the instantaneous total electric current density and B_k is the imposed magnetic field.) Considering the highly turbulent flow, we introduce the Large Eddy Simulation (LES) approach to simulate instantaneous flow and electromagnetic interactions by introducing the following set of the spatially-filtered transport equations:

$$\frac{\partial \overline{u}_i}{\partial x_i} = 0 \tag{4.3}$$

$$\frac{\partial \overline{u}_i}{\partial t} + \overline{u}_j \frac{\partial \overline{u}_i}{\partial x_j} = -\frac{1}{\rho}\frac{\partial \overline{p}}{\partial x_i} + \nu \frac{\partial^2 \overline{u}_i}{\partial x_j^2} - \frac{\partial \tau_{ij}^{sgs}}{\partial x_j} + \frac{1}{\rho}\overline{F}_i^L \tag{4.4}$$

where (–) indicates the spatial filtering and τ_{ij}^{sgs} is the sub-grid scale (SGS) stress tensor, which is calculated as:

$$\tau_{ij}^{sgs} = -2\nu_{sgs}\overline{S}_{ij}, \;\; \nu_{sgs} = (C_S\Delta)^2 (2\overline{S}_{ij}\overline{S}_{ij})^{\frac{1}{2}} \tag{4.5}$$

where ν_{sgs} is the sub-grid scale viscosity, S_{ij} is the strain rate tensor, C_S is the Smagorinsky parameter, and Δ is the filter length. The evaluation of C_S becomes crucial since the widely-used approach implying the constant Smagorinsky parameter [36] is not suitable for the present type of flow. It is recognized that the strong influence of the magnetic field affects not only the flow structure but also the turbulence [37]. At the same time, the dynamic determination of C_S is proved to be capable of reproducing this influence

[20]. Thus, the dynamic approach originally proposed by Lily [38] has been adopted in our work as follows:

$$C_S^2 = \frac{1}{2}\frac{\widehat{L_{ij}M_{ij}}}{\widehat{M_{ij}M_{ij}}} \tag{4.6}$$

$$L_{ij} = \widehat{\widetilde{u_i}\widetilde{u_j}} + \widehat{\widetilde{u_i}}\,\widehat{\widetilde{u_j}} \tag{4.7}$$

$$M_{ij} = \Delta^2\widehat{\widetilde{S}\widetilde{S}_{ij}} + \widehat{\Delta^2}\widehat{\widetilde{S}}\,\widehat{\widetilde{S}_{ij}} \tag{4.8}$$

where $\widehat{(\cdot)}$ indicates the averaging over the cell faces, $\widetilde{(\cdot)}$ indicates the second filtering operation, and $\widetilde{\Delta} = 2\Delta$ is the second filter length. Finally, the filtered Lorentz force in the extended momentum equation is calculated as:

$$\overline{F}_i^L = \epsilon_{ijk}\overline{J}_j B_k \tag{4.9}$$

where $\overline{J}_i$ is the filtered total current density and B_k is the uniform magnetic field. In the present study, we are dealing with the highly electrically conducting fluid (liquid metal) implying that the induced magnetic field can be neglected. Consequently, the one-way MHD coupling approach for the moving electrically conducting fluid can be formulated as:

$$Re_m = \frac{u_0 D}{\lambda} << 1 \tag{4.10}$$

$$\overline{J}_i = \sigma\Big(-\frac{\partial\overline{\phi}}{\partial x_i} + \epsilon_{ijk}\overline{u}_j B_k\Big) \tag{4.11}$$

where Re_m is the magnetic Reynolds number, u_0 is the inlet bulk velocity, D is the characteristic length, λ is the magnetic diffusivity, σ is the electrical conductivity of the fluid, J_i is the total current density, and ϕ is the electric potential. To find the electric potential, the Poisson equation, obtained by substituting the zero-divergence total current density condition into Eqn. (4.11), is used:

$$\frac{\partial^2\overline{\phi}}{\partial x_i^2} = \frac{\partial}{\partial x_i}(\epsilon_{ijk}\overline{u}_j B_k) \tag{4.12}$$

Finally, to define the flow regimes, the following non-dimensional numbers need to be introduced:

$$Re = \frac{u_0 D}{\nu}, \quad Ha = BD\sqrt{\frac{\sigma}{\rho\nu}} \tag{4.13}$$

where Re is the Reynolds number and Ha is the Hartmann number.

4.2.2. ARBITRARY ELECTRICALLY CONDUCTIVE WALLS

Continuous contact of a moving electrically conductive fluid subjected to an external magnetic field, with surrounding electrically conductive walls, leads to the transfer of the electric current density between the fluid/wall interface. To model this phenomenon, we have applied our recently developed conjugated MHD method [39] based on splitting the computation domain into liquid and solid sub-domains. Consequently, the Poisson equation is solved separately for each sub-domain as:

$$\frac{\partial}{\partial x_i}\left(\sigma_L \frac{\partial \overline{\phi}_L}{\partial x_i}\right) = \frac{\partial}{\partial x_i}(\epsilon_{ijk}\sigma_L \overline{u}_j B_k) \tag{4.14}$$

$$\frac{\partial}{\partial x_i}\left(\sigma_S \frac{\partial \overline{\phi}_S}{\partial x_i}\right) = 0 \tag{4.15}$$

where subscript L marks the liquid sub-domain values and S marks the solid sub-domain values. In order to characterize the flow regimes with electrically conductive walls, we introduce the following wall conductivity ratio parameter:

$$C_d = \frac{\sigma_S d_w}{\sigma_L D} \tag{4.16}$$

where d_w is the characteristic thickness of the wall.

4.2.3. NUMERICAL DETAILS

The discretized forms of the above-listed transport equations (Eqn. (4.3 - 4.15) were solved by our in-house finite-volume code ([39]) based on the open-source library OpenFOAM, [40]. The calculation of the Lorentz force is based on the Four Steps Projection Method [41], which fulfills the zero-divergence condition of the total electric current density on all cell faces. The second-order central differencing scheme (CDS) was used for spatial discretization, and the second-order backward scheme for temporal discretization. To obtain the electric potential values at the interface between the solid and fluid sub-domains, the weighted-flux scheme was applied [42]. Finally, coupling between the velocity and pressure fields was established through the PISO algorithm, [43].

4.3. GEOMETRY AND FLOW REGIMES

4.3.1. GEOMETRY AND MESH

The entire computational domain consists of two main parts: (i) the long square duct representing the liquid metal sub-domain, and (ii) two arbitrary conductive finite walls representing the solid sub-domain, Fig. 4.1. The width of the square duct is D, the thickness of the conductive wall is d_w, and the length of the entire domain is L. It should be noted that special attention should be devoted to the length of the domain in terms of

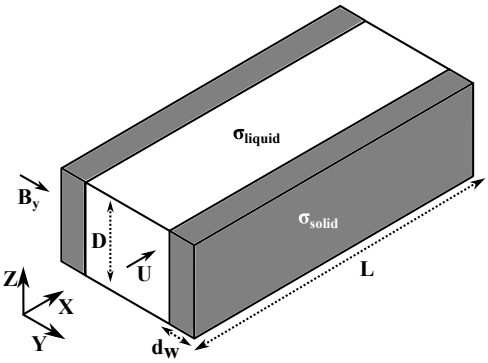

Figure 4.1: Sketch of the computational domain (not to scale). The grey color indicates finite arbitrary conductive walls (solid domain), while the white color indicates the liquid domain.

proper capturing of the coexisting laminar and turbulence regions (so-called patterned turbulence, [11]) and therefore the specific length of $L = 40D$ was chosen. To carry out the simulations, the orthogonal hexahedral non-uniform mesh was created. The numerical mesh was split into two sub-domains with the following distribution of control volumes: $(N_x \times N_y \times N_z = 720 \times 80 \times 80)_{\text{liquid}}$ and $(N_x \times N_y \times N_z = 720 \times 12 \times 80)_{\text{solid}}$, respectively. To exclude numerical errors on the interface between solid and liquid regions, the size of the first cells on each side was equal. Additional mesh requirement is associated with the proper numerical resolving of the Hartmann (walls perpendicular to the imposed magnetic field) and Shercliff (walls aligned with the imposed magnetic field) boundary layers. The mesh was refined in the boundary layers with the following set of the non-dimensional wall-distance parameters: $\Delta y^+_{wall} = 0.77$ and $\Delta z^+_{wall} = 0.79$. Such a refinement corresponds to approximately 9 mesh points for the Hartmann layer and over 20 mesh points for the Shercliff layer. The coarser mesh was applied in the core region with the following set of the parameters: $\Delta y^+_{core} = 11$ and $\Delta z^+_{core} = 10.7$. A cell-to-cell expansion ratio of $k_{exp} \approx 1.05$ was used in the y- and z-directions. An uniform mesh distribution was imposed in the streamwise x-direction with $\Delta x^+ = 21$.

4.3.2. BOUNDARY CONDITIONS AND FLOW REGIMES

The turbulent flow of the liquid metal is continuously driven in the x-direction by the pressure gradient. In order to maintain turbulence in the duct, periodic boundary conditions were imposed at the inlet and outlet of the duct. All other surfaces act as walls with no-slip velocity boundary conditions. The external constant uniform magnetic field is aligned with the y-direction, Fig. 4.1. The arbitrary electrically conductive finite walls are placed perpendicular to the imposed magnetic field (Hartmann walls). The top and bottom walls parallel to the magnetic field (Shercliff walls) were kept as fully electrically insulated ($(\partial\phi)/(\partial n) = 0$ and $C_d = 0$). The used arrangement of the conductive and insulated walls was theoretically postulated to be able to potentially impose significant

changes on flow and turbulence reorganization, [12].

Table 4.1: The overview of the flow conditions simulated in the present work.

Re	Ha	C_d, Hartmann walls
5602	0	-
	21.2	0
		0.05
		0.1
		0.15
		0.25
		0.5
		5
		∞

To focus primarily on the wall conductivity effects, the Reynolds and Hartmann number were fixed, $Re = 5602$ and $Ha = 21.2$. This set of the non-dimensional parameters proved to be sufficient to impose a significant flow and turbulence reorganization of the initially fully developed turbulence when all duct walls were electrically insulated, [21]. We have considered a wide range of the wall conductivity parameter (C_d), ranging from the fully electrically insulated to fully electrically conducting, i.e. $0 \leq C_d \leq \infty$. For the asymptotic wall conductivities the solid sub-domains can be excluded. The additional neutral case at $Ha = 0$ was also considered for validation purposes. An overview of all performed simulations is presented in Table. 4.1. To obtain fully convergent first- and second-moments statistics, we have used a time-averaging period of 300 flow-through times. This period equals to approximately 3 months of real-time using 32 cores of 2.6 GHz Intel Xeon E5-2697A v4.

4.4. RESULTS AND DISCUSSION

4.4.1. REORGANIZATION IN THE FLOW STRUCTURE

We start our analysis by showing the instantaneous flow features (arbitrary time) in the forms of the iso-surfaces of the second invariant of the velocity gradient tensor (Q-criterion), Fig. 4.2. It can be seen that a dense pattern is observed for the pure hydrodynamic case ($Ha = 0$), Fig. 4.2(a). Activation of the magnetic field for the electrically perfectly insulated walls ($C_d = 0$) leads to a suppression of coherent structures in the proximity of the Hartmann walls and in the duct center, Fig. 4.2(b). The distribution of coherent structures near the top Shercliff wall shows localized turbulent puffs, which are the first indicators of the patterned turbulence formation. The presence of these puffs is expected because of the present value of $Re/Ha = 264$ being close to the approximate transition limit of $Re/Ha = 250$ determined by Zikanov et al.[11] for the patterned MHD turbu-

lence.

With the activation of the finite electrical conductivity of the Hartmann walls, even relatively low value of the conductivity ratio parameter ($C_d = 0.05$) produced a significant turbulence suppression, Fig. 4.2(c). Now, the coherent structures are less dense in the vicinity of the Shercliff walls and almost vanished near the Hartmann walls. Moreover, in contrast to the case of the fully electrically insulated walls ($C_d = 0$), the clustering of turbulent puffs near the Shercliff walls is more pronounced. This behavior is further enhanced at $C_d = 0.1$, where distinct morphology of laminar and turbulent spots can be observed, Fig. 4.2(d). The full laminarization occurs at $C_d = 0.15$, Fig. 4.2(e). The here observed patterned turbulence phenomenon is a well-recognized feature of the characteristics turbulent to laminar suppression of the MHD turbulence, as previously reported in [23], [11]. However, the appearance of this regime was always associated with a continuous increase of the magnetic field strength but not with the fixed Ha and variable C_d. The onset of patterned turbulence is sensitive to the length of the computational domain (required to be at least eighty half-widths of the duct, as shown in [23]). A significantly reduced horizontal extension of the computational domain can artificially suppress the turbulent puffs producing a fully laminarized flow regime. To be able to properly resolve the coexistence of the laminar/turbulent flow regimes within the duct, the length of the square duct was selected to satisfy this condition, i.e. $L = 40D$. With a further increase of $C_d = 0.25$, the turbulent puffs reappear, as shown in Fig. 4.2(f). This turbulence regeneration process is characterized by the appearance of clusters of turbulence puffs in the duct center. At $C_d = 0.5$, the clusters of turbulent puffs expand towards the Hartmann walls, Fig. 4.2(g). After reaching $C_d = 5$, the coherent structures are significantly denser than for the case of the electrically insulated walls ($C_d = 0$), as it can be seen in Fig. 4.2(h). Finally, when $C_d \to \infty$, the turbulence state is fully recovered portraying a very dense distribution of coherent structures, Fig. 4.2(i).

Next, we focus on the long-term time-averaged flow characteristics. The contours of the mean velocity magnitude spatially averaged over the entire duct length, for different values of C_d, are shown in Fig. 4.3. The velocity distribution for the MHD neutral case exhibits a fully symmetrical pattern with the maximum value in the duct center, Fig. 4.3(a). Activation of the magnetic field for the duct with electrically insulated walls ($C_d = 0$) produced elongation of the mean velocity magnitude towards the Shercliff walls, Fig. 4.3(b). By replacing the electrically insulated Hartmann walls with the weekly conducting ones ($C_d = 0.05$), further elongation of the high-velocity region towards the Shercliff walls and further reduction from the Hartmann walls was obtained, Fig. 4.3(c). At $C_d = 0.15$, an interesting flow reorganization occurred, Fig. 4.3(d). It can be seen that the two distinct regions with elevated velocity magnitude were generated in the proximity of Shercliff walls. This distribution is a consequence of the flow laminarization, as previously illustrated in Fig. 4.2(d). When a partial regeneration of the turbulence was obtained at $C_d = 0.25$, the wall jets in the proximity of Hartmann walls start to be elongated in the y-direction, forming two distinct ellipsoid-like regions, Fig. 4.3(e). For $C_d = 0.5$, a fur-

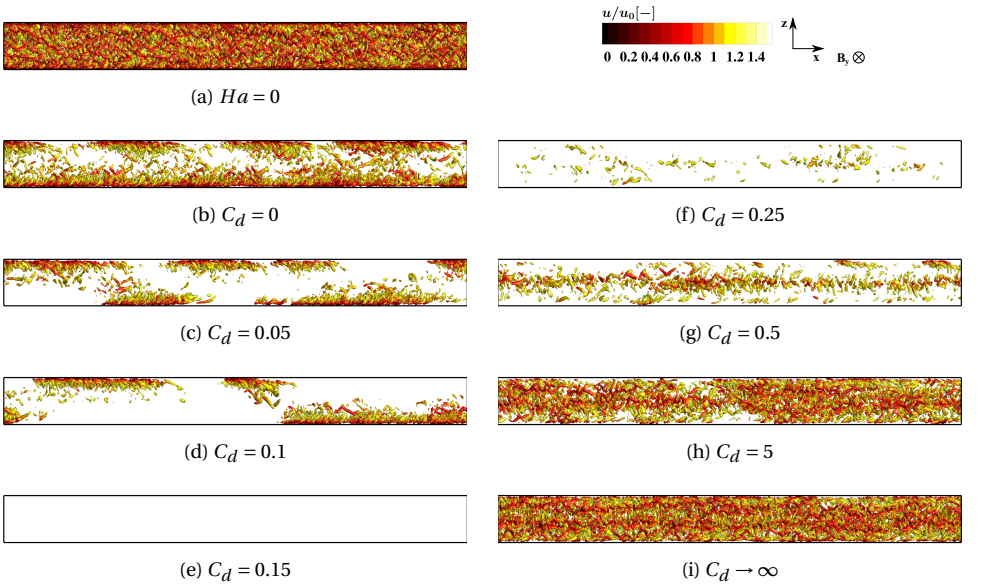

(a) $Ha = 0$

(b) $C_d = 0$

(c) $C_d = 0.05$

(d) $C_d = 0.1$

(e) $C_d = 0.15$

(f) $C_d = 0.25$

(g) $C_d = 0.5$

(h) $C_d = 5$

(i) $C_d \to \infty$

Figure 4.2: The side-view of the iso-surfaces of the second-invariant of the velocity gradient (Q-criterion, Q = 0.8 s^{-2}) colored by instantaneous non-dimensional velocity magnitude ($|u|/u_0$) at (a) $Ha = 0$, and (b-h) $Ha = 21.2$, $0 \leq C_d < \infty$. Note that the scale factor of $L_{scale} = 0.4$ is applied in the x-direction for a better visibility.

ther reduction of these distinct wall jet regions is obtained, Fig. 4.3(f). From $C_d = 5$ to $C_d \to \infty$, just marginal changes can be observed, indicating the saturation regime was achieved already at the previous value of C_d, Figs. 4.3(g-h).

It is interesting to note that the previous studies dealing with laminar MHD flows and electrically conductive walls demonstrated a gradual change of the velocity pattern with an increase of the wall conductivity[28],[29],[39]. In the laminar MHD duct flows, there were no sudden transitions occurring between $C_d = 0.05$, $C_d = 0.15$ and $C_d = 0.25$. Here, we postulate that observed non-monotonic behavior of the mean velocity magnitude are the consequence of the initial re-laminarization and re-appearance of the turbulence in the duct. To confirm this, we have evaluated the profiles of the non-dimensional mean streamwise velocity along the central vertical (between Shercliff walls) and horizontal (between Hartmann walls) cross-sections, Fig. 4.4. The DNS results of [44] for the non-MHD case ($Ha = 0$) in the square duct flow were used as a reference for validation of our simulations. It can be seen that a good agreement was obtained for the reference case. With changes in the electrical conductivity of the side walls, significant deviations from the classic log-law distribution were obtained in the vertical cross-section, Fig. 4.4(a). Already at $C_d = 0$ and $C_d = 0.05$, the vertical profiles exhibited re-laminarization trends. The laminarized state was obtained at $C_d = 0.15$. After this point, a further increase of

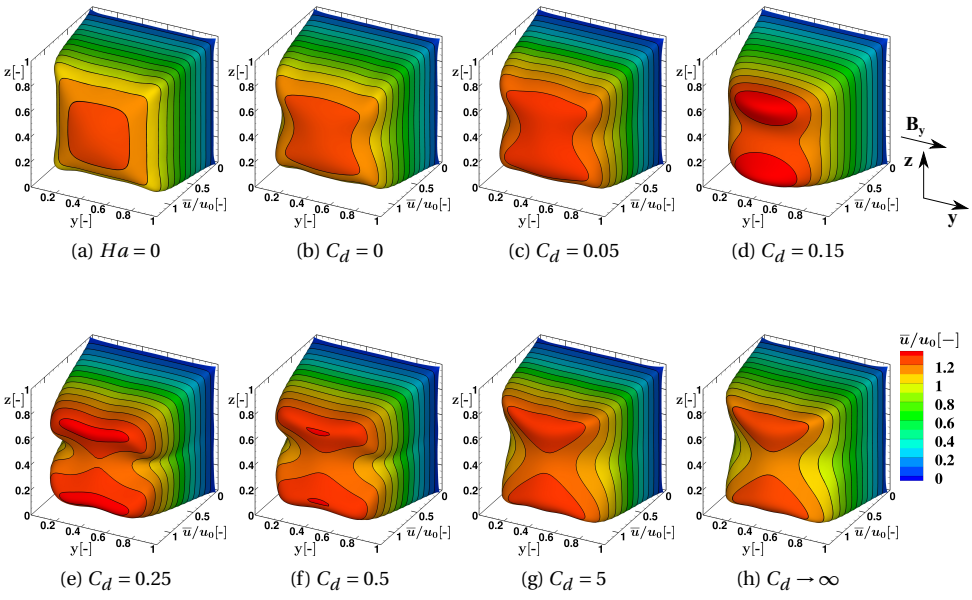

(a) $Ha = 0$ (b) $C_d = 0$ (c) $C_d = 0.05$ (d) $C_d = 0.15$

(e) $C_d = 0.25$ (f) $C_d = 0.5$ (g) $C_d = 5$ (h) $C_d \to \infty$

Figure 4.3: The time- and spatially-averaged (along the entire duct length) non-dimensional velocity magnitude distribution in the vertical cross-section: (a) $Ha = 0$, and (b-h) $Ha = 21.2$, $0 \leq C_d < \infty$.

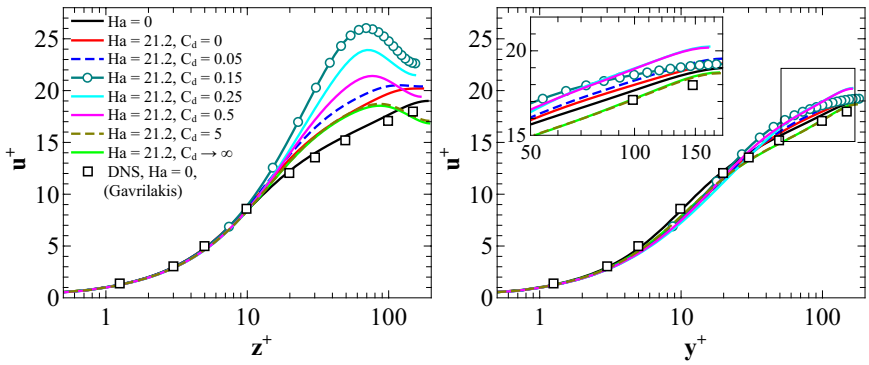

(a) (b)

Figure 4.4: Dependency of the time-averaged non-dimensional streamwise velocity $u^+ = u/u_\tau$ versus the non-dimensional wall distance $[y,z]^+ = u_\tau[y,z]/\nu$ along the central vertical (between the Shercliff walls) (a) and horizontal (between the Hartmann walls) (b) cross-sections.

C_d reversed this behavior, resulting in distributions closer to the neutral log-law behavior, confirming the turbulence re-appearance. The horizontal profiles (i.e. between the Hartmann walls) were showing much less variation, Fig. 4.4(b). Even for the $C_d = 0.15$

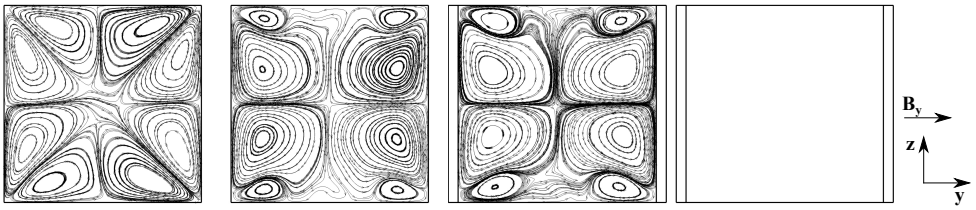

(a) $Ha = 0$ (b) $C_d = 0$ (c) $C_d = 0.05$ (d) $C_d = 0.15$

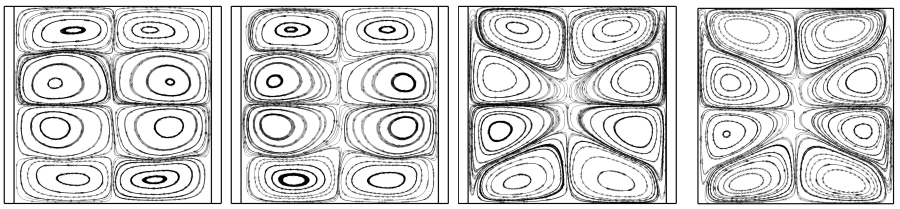

(e) $C_d = 0.25$ (f) $C_d = 0.5$ (g) $C_d = 5$ (h) $C_d \to \infty$

Figure 4.5: The time-averaged two-dimensional (y- and z- components) velocity streamlines indicating the secondary motions in the vertical (the x-component) cross-section at (a) $Ha = 0$, and (b-h) $Ha = 21.2$, $0 \leq C_d < \infty$.

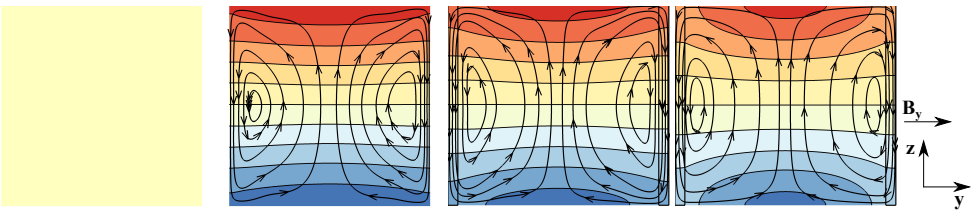

(a) $Ha = 0$ (b) $C_d = 0$ (c) $C_d = 0.05$ (d) $C_d = 0.15$

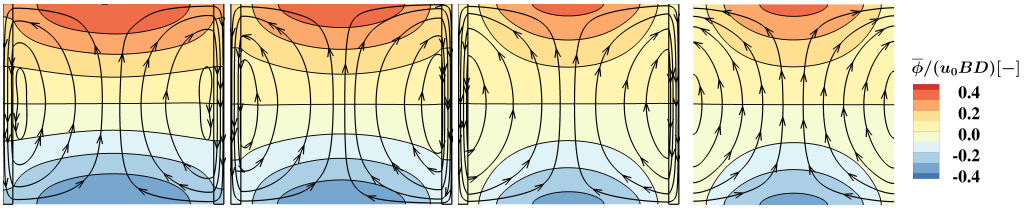

(e) $C_d = 0.25$ (f) $C_d = 0.5$ (g) $C_d = 5$ (h) $C_d \to \infty$

Figure 4.6: The contours of the time-averaged non-dimensional electric potential superimposed with the total current density streamlines in the vertical (the x-component) cross-section at (a) $Ha = 0$, and (b-h) $Ha = 21.2$, $0 \leq C_d < \infty$.

value, the deviation from the characteristic log-law distribution was just marginal.

Effects of the wall conductivity on the secondary motion (long-term time- and spatially-

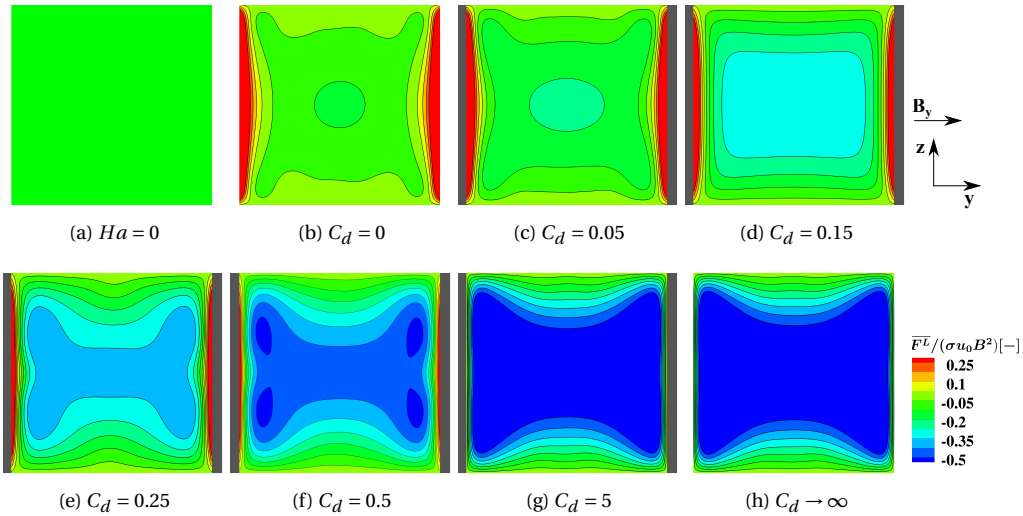

(a) $Ha = 0$ (b) $C_d = 0$ (c) $C_d = 0.05$ (d) $C_d = 0.15$

(e) $C_d = 0.25$ (f) $C_d = 0.5$ (g) $C_d = 5$ (h) $C_d \to \infty$

Figure 4.7: The time-averaged non-dimensional streamwise Lorentz force contours in the vertical (the x-component) cross-section at (a) $Ha = 0$, and (b-h) $Ha = 21.2$, $0 \leq C_d < \infty$.

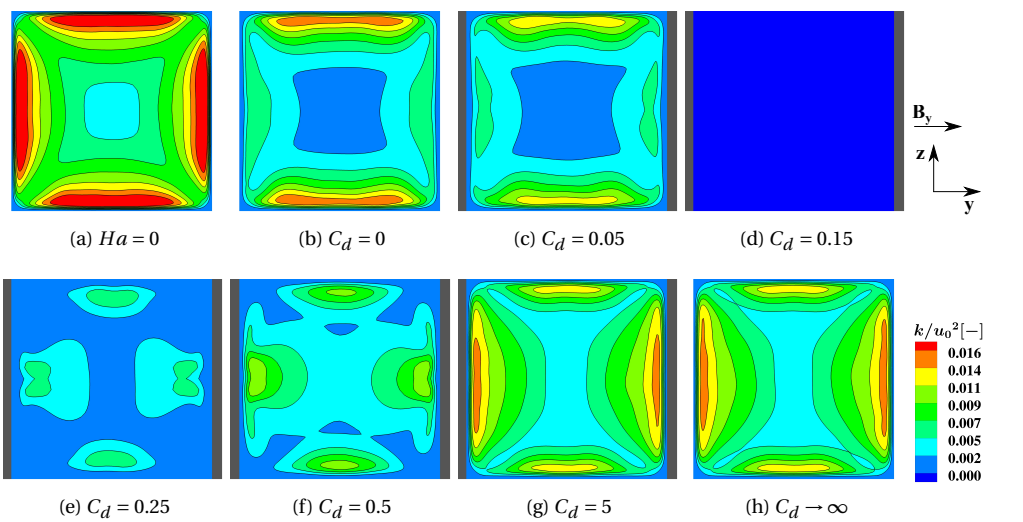

(a) $Ha = 0$ (b) $C_d = 0$ (c) $C_d = 0.05$ (d) $C_d = 0.15$

(e) $C_d = 0.25$ (f) $C_d = 0.5$ (g) $C_d = 5$ (h) $C_d \to \infty$

Figure 4.8: The resolved non-dimensional turbulent kinetic energy contours in the vertical (the x-component) cross-section at (a) $Ha = 0$, and (b-h) $Ha = 21.2$, $0 \leq C_d < \infty$.

averaged y- and z-velocity components) are shown in Fig. 4.5. For the MHD neutral case, a full diagonal symmetrical distribution was generated with eight identical size eddies, Fig. 4.5(a). This diagonal symmetry was broken with activation of the magnetic field

for the case where all walls were electrically insulated ($C_d = 0$), Fig. 4.5(b). The eddies in the proximity of Shercliff walls were suppressed, while the eddies in the proximity of the Hartmann walls got elongated in the y-direction. By replacing the electrically insulated with electrically conducting walls (i.e. $C_d = 0.05$), the eddies located near the Shercliff walls slightly expanded, Fig. 4.5(c). For $C_d = 0.15$, because of a sudden flow re-laminarization, there were no secondary motions generated, Fig. 4.5(d). With further increase of C_d ($0.25 \leq C_d \leq 0.5$) and turbulence regeneration, the secondary flow patterns reappeared, Figs. 4.5(e-h). Now, the eddies are differently organized, and the diagonal symmetry was replaced by the central vertical line symmetry. For $C_d = 0.25$ and 0.5, the eddies are oriented in the direction of the imposed magnetic field (i.e. the y-direction), Figs. 4.5(e-f). With a further increase of the wall conductivity, the eddies in the proximity of the Shercliff walls were suppressing the ones along the Hartmann walls, Fig. 4.5(g). Again, the condition of the perfectly conducting walls just marginally changed the morphology of secondary motion eddies, Fig. 4.5(h).

To provide detailed insights into the origins of the flow reorganization, we focus on distributions of the electromagnetic parameters. The contours of the mean electric potential with superimposed streamlines of the total current density are plotted in Fig. 4.6. By evaluating the case of the fully electrically insulated walls, it can be seen that a linear distribution between the Shercliff walls is obtained with fully closed loops of the total current density within the fluid region, Fig. 4.6(b). Activation of the electrically conducting walls leads to a gradual reduction of the local maximum/minimum electric potential zones near the Shercliff walls, Figs. 4.6(c)-(h). Furthermore, the loops of the total current density also penetrate the solid domains. With a C_d increase, the resistance to the current transfer within the walls is significantly reduced, resulting in the gradual changes of the current density loops in the proximity of the Hartmann walls. These changes in the current density behavior immediately contribute to the Lorentz force distribution, as shown in Fig. 4.7. For the $C_d = 0$ case, the contours of the most dominant streamwise component of the Lorentz force show high positive contributions in the proximity of the Hartmann walls, Fig. 4.7(b). Further away from the walls, the streamwise component of the Lorentz force becomes negative. The regions near the Shercliff walls are less affected since the direction of the current density is mainly parallel to the imposed magnetic field. An increase in the Hartmann walls conductivity ($0.05 \leq C_d \leq 0.5$) leads to the significant reduction of regions with positive values and appearance of strongly negative regions in the duct center, Figs. 4.7(c-f). For $C_d = 5$ and $C_d \to \infty$, these high positive regions along the Hartmann walls have disappeared, and a large region with the strong negative contributions is present in the large portion of the duct center, Fig. 4.7(g-h).

4.4.2. THE IMPACT ON THE TURBULENCE FEATURES

Next, we focus on the turbulence parameters. The contours of the long-term time- and spatially-averaged (in the streamwise direction) resolved turbulent kinetic energy in the vertical cross-section are shown in Fig. 4.8. The typical fully symmetrical distribution

with enhanced turbulence region in the proximity of walls was obtained for the neutral case, Fig. 4.8(a). With the MHD activation, for the $C_d = 0$ case, a strong suppression is obtained in the proximity of the Hartmann walls, whereas the suppression in the proximity of the Shercliff walls was less, Fig. 4.8(b). With a further increase of the $C_d = 0.05$, the turbulence suppression continued, making both the wall and center of duct regions less turbulent, Fig. 4.8(c). For $C_d = 0.15$ a full flow relaminarization occurred, Fig. 4.8(d). An interesting distribution of the resolved turbulent kinetic energy was obtained for $C_d = 0.25$, Fig. 4.8(e). The localized spots placed at approximately halfway between the walls and the duct center can be seen, confirming the localized turbulence regeneration. For $C_d = 0.5$, these localized turbulence regions expanded further, now covering the entire duct center region too, Fig. 4.8(f). At $C_d = 5$, this process of the turbulence regeneration continued with locally enhanced spots in the proximity of walls, Fig. 4.8(g). Now, in contrast to the relaminarization process, the regions in the proximity of the Hartmann walls were significantly more turbulent compared to the regions in the proximity of the Shercliff walls. The identical trend with marginal modification was also present at $C_d \to \infty$, confirming the turbulence sustenance, Fig. 4.8(h). The recovery of the turbulence is correlated to the Lorentz force redistribution and its impact on the flow: two jets directly contribute to the turbulence level in the proximity of the Shercliff walls, while the excessively strong Lorentz force augments the velocity gradient in the proximity of the Hartmann walls. The profiles of the non-dimensional RMS of the velocity component fluctuations along the central vertical and horizontal intersections for different values of C_d are shown in Fig. 4.9. Note that additional DNS data were also plotted for the non-MHD [44] and the MHD case with $C_d = 0$ [21]. It can be seen that a good agreement between our LES and DNS data from the literature was obtained. For the RMS profiles for all velocity components along the central vertical line exhibit qualitatively similar behavior: a continuous decrease in the $0 \leq C_d \leq 0.15$ range, a full relaminarization at $C_d = 0.15$, and a continuous increase in the $0.25 \leq C_d < \infty$ range, Figs. 4.9(a,c,e). It should be noted that after the turbulence regeneration, the obtained peak RMS value in the wall proximity of all velocity components were smaller than corresponding values for the initial non-MHD case. Furthermore, in this turbulence regeneration phase (i.e. for $C_d \geq 0.25$), all RMS profiles along the central vertical line exhibit characteristic double peaks. The second peaks were located close to the duct center are asymptotically approaching the non-MHD values and are higher than the reference MHD case with the fully insulated walls ($C_d = 0$). The profiles of the RMS of the velocity components along the central horizontal line show a different behavior, Figs. 4.9(b,d,f). There are no secondary peaks observed, and for $C_d \geq 5$, in comparison to the non-MHD case, all RMS values show higher values in the region between the near-wall peak location and the center of the duct ($0.15 \leq y/D \leq 0.5$).

The profiles of the turbulent shear stress components are shown in Fig. 4.10. The vertical profiles of the $\overline{u'w'}$ component show monotonous damping of the peak values in the proximity of the Shercliff wall until a full relaminarization was obtained ($0 \leq$

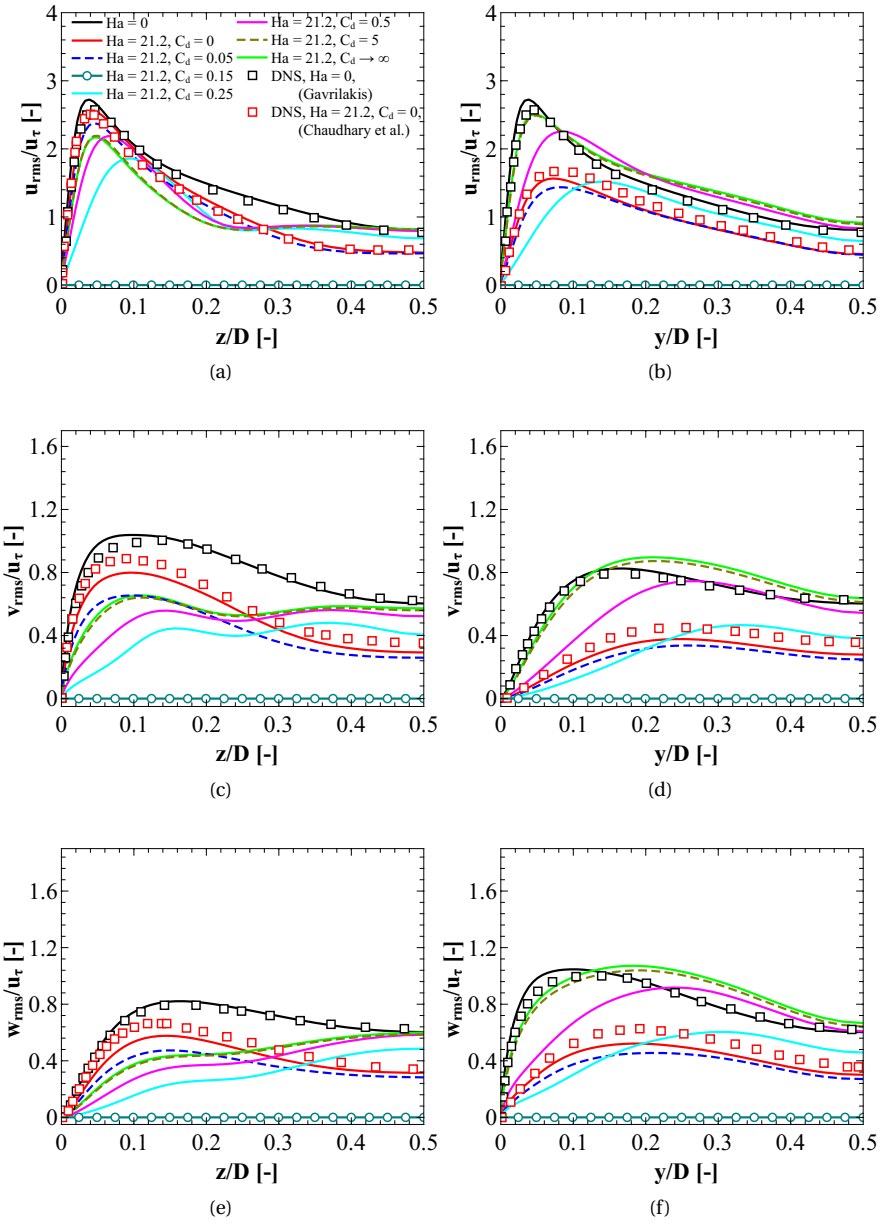

Figure 4.9: The profiles of non-dimensional RMS of the velocity fluctuations (u', v' and w') along the central horizontal and vertical intersections in the proximity of the (a,c,e) Shercliff and (b,d,f) Hartmann walls.

$C_d \leq 0.15$), Fig. 4.10(a). During the turbulence regeneration process, the near-wall peaks gradually increase until the saturation point was reached at $C_d = 5$. Interestingly, during

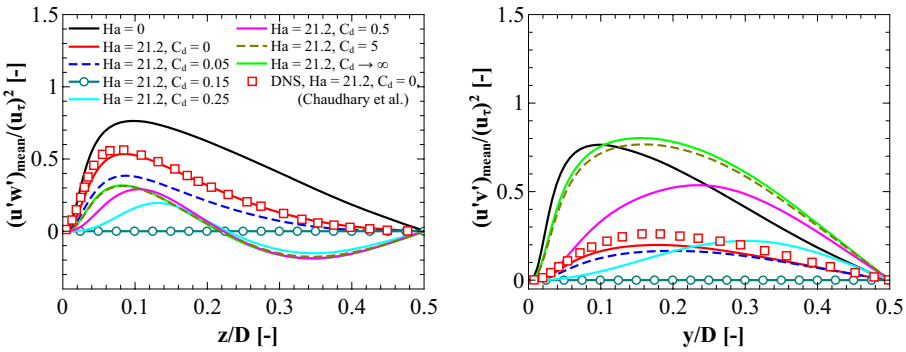

Figure 4.10: The non-dimensional time-averaged profiles of non-diagonal components of the Reynolds stress tensor $\overline{u'w'}$ and $\overline{u'v'}$ along the central vertical and horizontal intersections in the proximity of the (a) Shercliff and (b) Hartmann walls.

the process of the turbulence reappearance and sustenance ($0.25 \leq C_d \rightarrow \infty$), characteristic negative contributions of the shear stress were obtained in the $0.2 \leq z/D \leq 0.5$ region. This behavior of the vertical profiles, as well the double-peak behavior of the v_{rms} and w_{rms} components (already discussed in Fig. 4.9, can be explained in terms of the double-jet M-shape formation in the proximity of the Shercliff walls, as illustrated in Fig. 4.3(e-h). The horizontal profiles of the $\overline{u'v'}$ turbulent stress component exhibited a qualitatively different behavior, Fig. 4.10(b). Here, after the initial effective suppression ($0 \leq C_d \leq 0.15$), an effective recovery occurred, resulting in the rapid increase of the shear stress component. Now, the peak values in the wall proximity reached values of the non-MHD case (albeit with their locations moved farther away from the Hartmann wall). Furthermore, the values of the $\overline{u'v'}$ were surpassing values for the neutral non-MHD case in ($5 \leq C_d \rightarrow \infty$) range.

Next, we move to analyze the budget of the turbulent kinetic energy transport equation. By introducing the long-term time-averaging $\langle\,\rangle$ and fluctuating ($'$) operators, the equation can be written in the general form as:

$$\underbrace{\langle u_j\rangle\frac{\partial k}{\partial x_j}}_{Convection} = \underbrace{-\langle u_i'u_j'\rangle\frac{\partial\langle u_i\rangle}{\partial x_j}}_{Production} \underbrace{-\frac{1}{2}\frac{\partial\langle u_i'u_i'u_j'\rangle}{\partial x_j}}_{\substack{Turbulent\\ diffusion}} \underbrace{-\frac{1}{\rho}\langle u_i'\frac{\partial p'}{\partial x_i}\rangle}_{\substack{Pressure\\ diffusion}} \underbrace{+2\nu\frac{\partial\langle S_{ij}'u_i'\rangle}{\partial x_j}}_{\substack{Viscous\\ diffusion}} \underbrace{-2\nu\langle S_{ij}'S_{ij}'\rangle}_{Dissipation}$$
$$\underbrace{-\frac{\partial\langle\tau_{ij}^{sgs}u_i'\rangle}{\partial x_j}}_{\substack{SGS\\ diffusion}} + \underbrace{\langle\tau_{ij}^{sgs}S_{ij}'\rangle}_{\substack{SGS\\ dissipation}} \underbrace{-2\frac{\sigma}{\rho}kB_k^2}_{\substack{MHD\\ loss}} \underbrace{-\frac{\sigma}{\rho}\epsilon_{ijk}B_k\langle u_i'\frac{\partial\phi'}{\partial x_j}\rangle + \frac{\sigma}{\rho}\langle u_i'u_j'\rangle B_iB_k}_{\substack{MHD\\ gain}} \qquad (4.17)$$

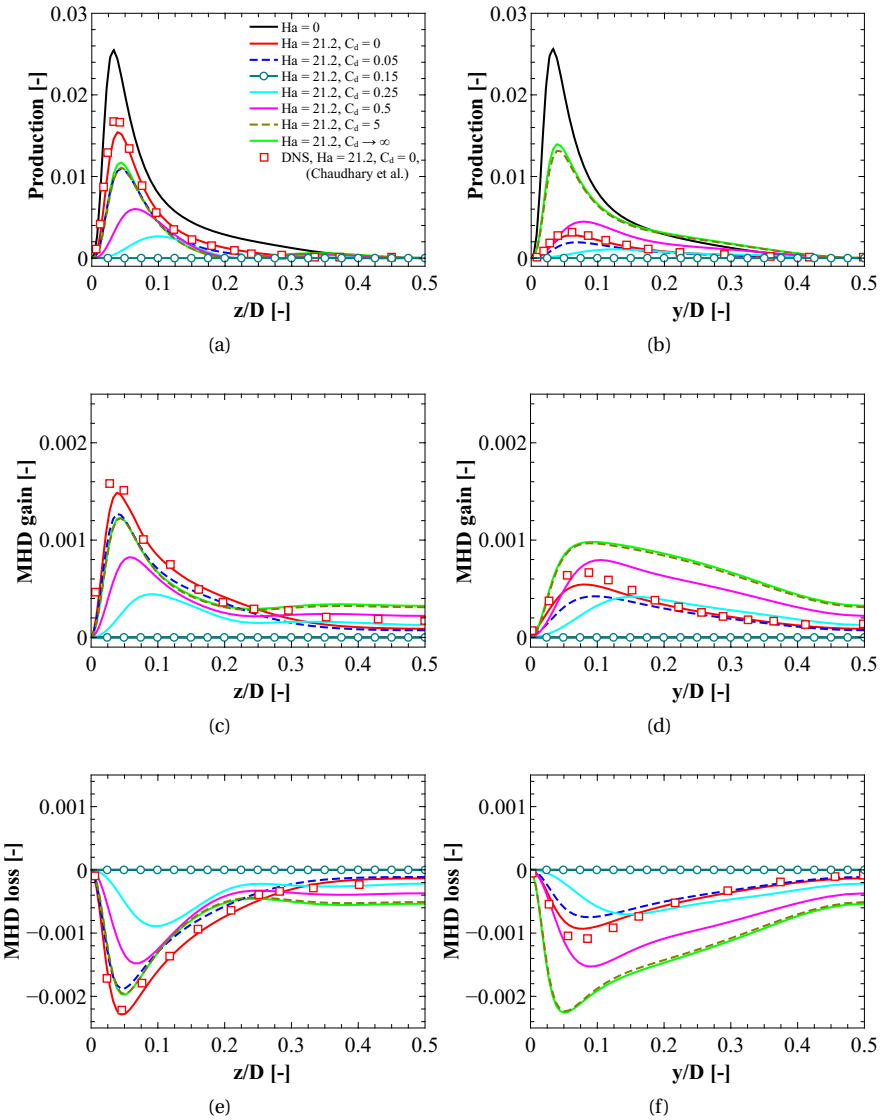

Figure 4.11: The profiles of non-dimensional turbulent kinetic energy budget terms (production, MHD gain and MHD loss) extracted along the central vertical and horizontal intersections in the proximity of the (a,c,e) Shercliff and (b,d,f) Hartmann walls.

The distributions of the turbulent kinetic energy budget terms (scaled with u_0^3/D) along the central vertical and horizontal intersections of the central vertical plane are presented in Figs. 4.11 and 4.12. This separation of the term contributions is done to provide a better overview of the physical mechanism of the energy distribution. The

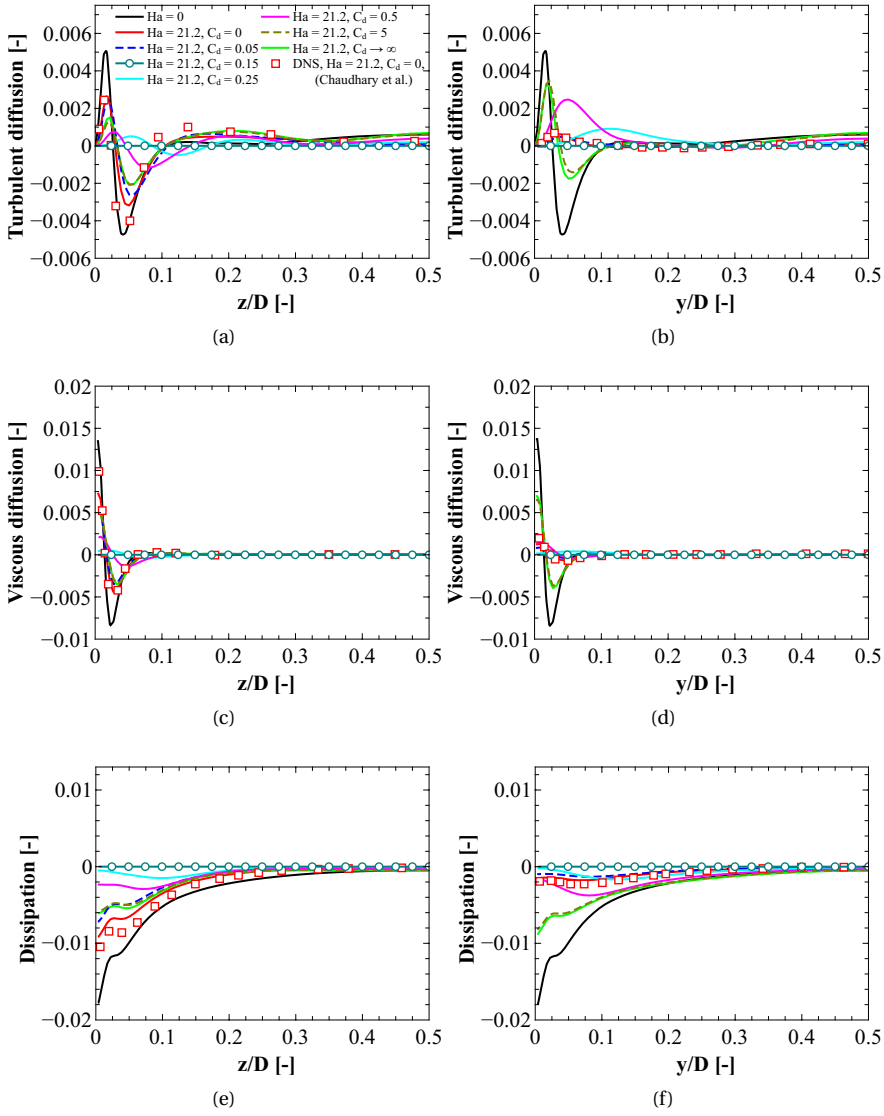

Figure 4.12: The profiles of the non-dimensional turbulent kinetic energy budget terms (turbulent diffusion, viscous diffusion and dissipation) along the central vertical and horizontal intersections in the proximity of the (a,c,e) Shercliff and (b,d,f) Hartmann walls.

contributions of the pressure and subgrid diffusion, as well as subgrid dissipation are not shown due to their negligible contributions compared with the remaining terms. For comparative purposes, we also have plotted budget contributions of the fully insulated case (C_d = 0) from the literature [21]. It can be concluded that for all presented bud-

get contributions, a generally good agreement between the present results and results from the literature [21] were obtained. Some minor local differences (e.g. for turbulent diffusion and viscous dissipation) can be explained in terms of different numerical approaches used.

Starting from the mechanical production term, it can be seen that the activation of the imposed magnetic field suppresses the characteristic near-wall peak values in the proximity of both walls until the full relaminarization is achieved ($0 \leq C_d \leq 0.15$), Fig. 4.11(a,b). With further increase of C_d, the production contribution increases, the final peak value (at $C_d \to \infty$) in the proximity of the Hartmann wall now exceeds the value in the proximity of the Shercliff wall. When compared to the peak values for the $C_d = 0$ case, the peak value for $C_d \to \infty$ in the proximity of the Hartmann wall shows an increase of almost factor four (Fig. 4.11(b)), whereas the peak value in the proximity of the Shercliff wall was reduced by approximately 60%, Fig. 4.11(a).

The qualitative similar behavior of the production term is also observed for profiles of the MHD gain (Figs. 4.11(c,d)) and MHD loss budget terms (Figs. 4.11(e,f)). However, in contrast to the production term, the MHD budget contributions changed less significantly in response to the varied wall conductivity, especially in the proximity of the Hartmann wall, Fig. 4.11(d). The peak values of the MHD gain term for $C_d = 5$ and $C_d \to \infty$ in the vicinity of the Hartmann wall are now slightly enhanced (approximately 20%) in comparison to the $C_d = 0$ case. In contrast, the MHD loss term peak in the proximity of the Hartmann wall almost doubled for $C_d \to \infty$ when compared to the $C_d = 0$, Fig. 4.11(f). By comparing the order of magnitude between the production (Figs. 4.11(a,b)) and MHD gain budget (Fig.4.11(c,d)) terms, we can conclude the flow reorganization (because of the presence of the mean velocity gradient in the production term) has a leading role with respect to the pure turbulence contributions and their interaction with the imposed magnetic field.

The profiles of the turbulent and viscous diffusion demonstrate significant contributions only in the proximity of the walls, Figs. 4.12(a,b,c,d). In the vicinity of the Shercliff wall, the final $C_d \to \infty$ almost halved in comparison to the $C_d = 0$ case, Fig. 4.12(a). In contrast to that behavior, for identical values of C_d, the profiles of the turbulent diffusion near the Hartmann wall were augmented for a factor three, Fig. 4.12(b). The qualitative similar trends were observed also for the viscous diffusion terms, Figs. 4.12(c,d). Finally, the dissipation profiles in the proximity of the Shercliff wall show lower values for $C_d \to \infty$ than for $C_d = 0$ case, Fig. 4.12(e). In contrast, a significant augmentation was obtained in the vicinity of the Hartmann wall for $C_d \to \infty$, Fig. 4.12(f). This behavior was expected due to a balance between the viscous diffusion and dissipation budget terms at the duct walls.

Next, we analyze the turbulence anisotropy states by plotting the Lumley's turbulence triangles ([45]) for the turbulent stress components extracted along the central vertical and horizontal intersections, Figs. 4.13(a,c), respectively. Here, ξ and η are the second and third-invariants of the anisotropy tensor b_{ij}, defined as:

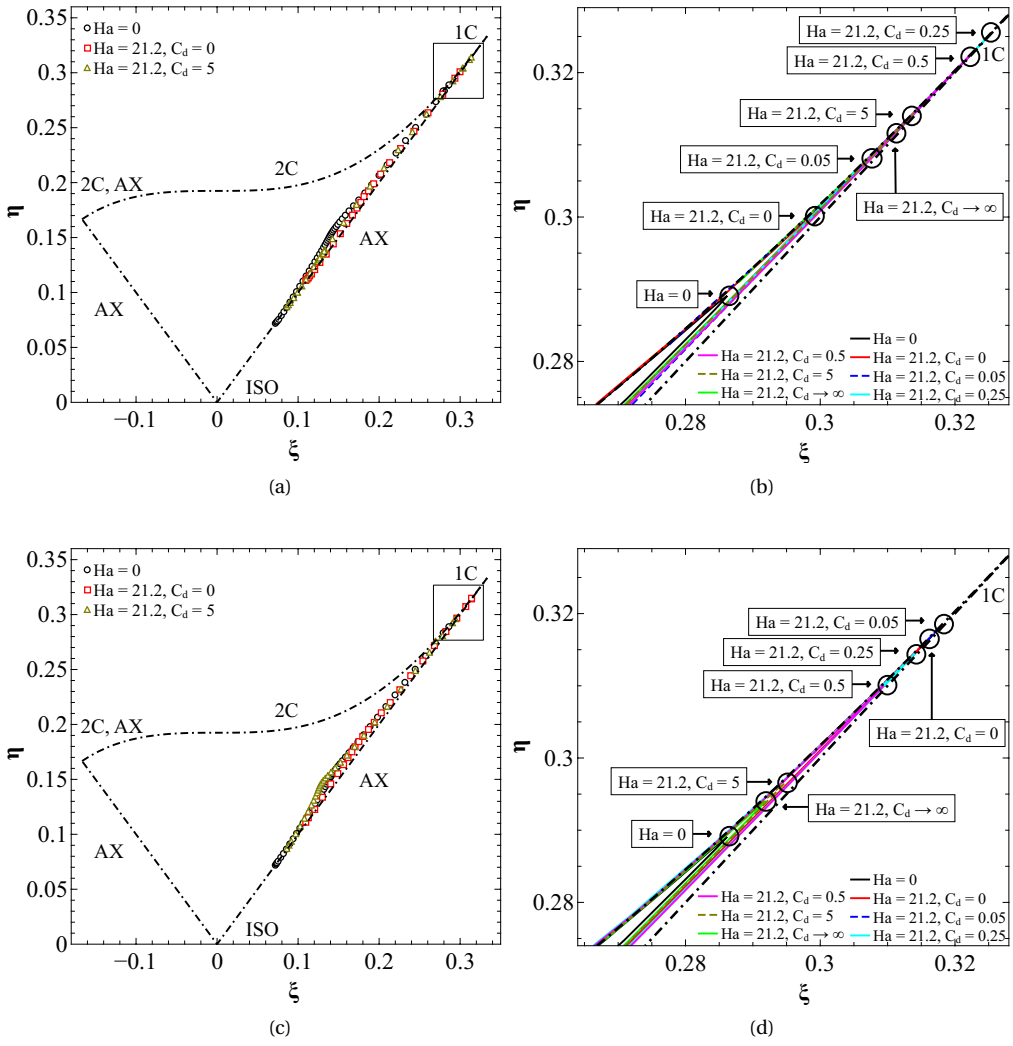

Figure 4.13: The anisotropy distribution of the turbulence (Lumley triangle) extracted along the central vertical (in the proximity of the Shercliff wall) (a) and horizontal (in the proximity of the Hartmann wall) (c) profiles of the vertical cross-section of the duct. The zoom-in of the zone indicating one-component turbulence for the Shercliff and Hartmann regions is presented in (b) and (d) correspondingly. The following notation is used for the turbulence states: ISO - isotropic, 2C - two-component, 1C - one-component, AX - axisymmetric.

$$6\eta^2 = b_{ij}b_{ji},\ 6\xi^3 = b_{ij}b_{jk}b_{ki},\ b_{ij} = \frac{\overline{u_i' u_j'}}{2k} - \frac{1}{3}\delta_{ij} \tag{4.18}$$

Starting from the entire map of turbulence state distributions for the neutral (non-MHD) case one can observe typical two-component (2C) region close to the walls, followed by the one-component (1C) state, and the final axisymmetric state (AX), Figs. 4.13(a,c). Then, to provide a better insight into turbulence state reorganization caused by the imposed electrical conductivity of the duct side walls, we provide zoom-ins in the proximity of the one-component turbulence state point (1C) for profiles extracted along the vertical and horizontal central intersections, respectively, as shown in Figs. 4.13(b,d).

The minimum of the turbulence anisotropy (defined in terms of the farthest distance from the 1C limit point) was obtained for $Ha = 0$ case for both walls. In the vicinity of the Shercliff wall, an increase in the electrical wall conductivity leads to the anisotropy increase in $0 \leq C_d < 0.25$ range, Fig. 4.13(b). The peak is achieved at $C_d = 0.25$ after which a decrease is obtained in $0.25 < C_d < \infty$ range. Despite this reduction in the turbulence anisotropy, the final $C_d \to \infty$ value is still more anisotropic than the $C_d = 0$ situation. The turbulence anisotropy in the proximity of the Hartmann wall showed a different behavior, Fig. 4.13(d). Now, an enhancement of turbulence anisotropy was observed only in the relatively narrow region $0 \leq C_d < 0.05$. At $C_d = 0.05$ the peak value was reached, followed by a gradual decrease as C_d increased. In contrast to the Shercliff wall, the anisotropy value in the vicinity of the Hartmann wall at $C_d \to \infty$ is much closer to the neutral case ($Ha = 0$) value.

Finally, we performed the analysis of the time series of the instantaneous streamwise velocity sampled at characteristic monitoring locations in the duct center and in proximities of the Shercliff and Hartmann walls. for different values of the C_d, Fig. 4.14. It can be seen that the instantaneous behavior in the duct center is just slightly affected by imposed changes of the C_d parameter, Fig. 4.14(a). The instantaneous response is different for the near-wall locations, Fig.4.14(b,c). Here, the imprints of the patterned turbulence structures are particularly visible in the form of quasi-periodic signals for the $C_d = 0.1$ case. Corresponding power spectra density (PSD) distributions [46] are shown in Fig. 4.15. The characteristic slopes of $-5/3$ (Kolmogorov inertial range) and $-16/3$ (dissipation range) do not show any significant changes with imposed C_d variation in the duct center, Fig. 4.15(a). A sudden appearance of the leading frequency $f = 0.02$ Hz can be seen for $C_d = 0.1$, which corresponds to the characteristic quasi-periodic signal shown in Fig. 4.14(a). At the location in the proximity of the Shercliff wall, notable differences are obtained for the $C_d = 0.25$, where the inertial range started at the lower frequencies, and where the dissipative range slope becomes less steep, Fig. 4.15(b). In the vicinity of the Hartmann wall, the observed changes in characteristic slopes were more pronounced, Fig. 4.15(c). The inertial range started at lower frequencies already at $C_d = 0$, while the dissipation range slope was less rapid at $C_d = 0.1$. With a further increase in C_d, the slope of $-16/3$ in the dissipation range was recovered.

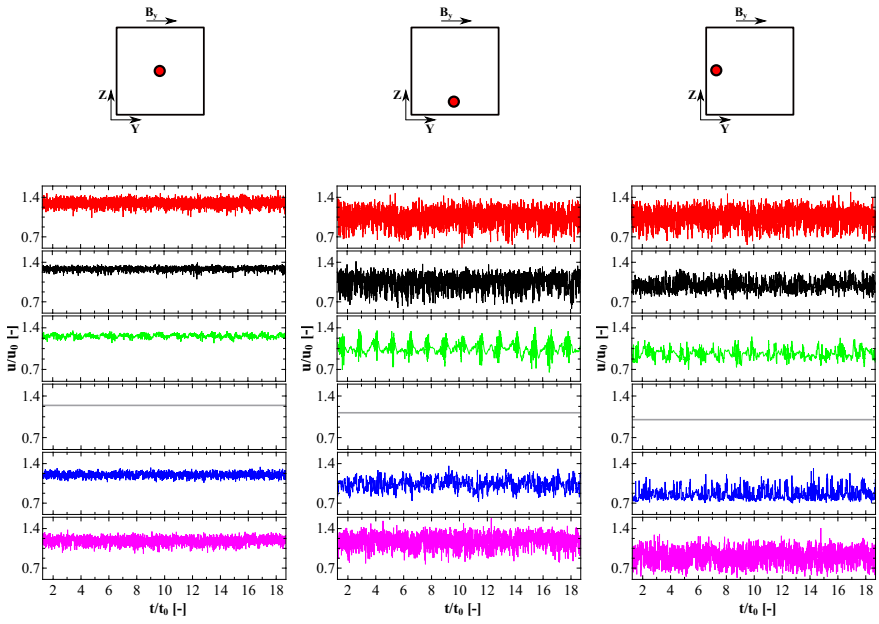

Figure 4.14: The time series of the non-dimensional instantaneous streamwise (x-component) velocity in the center of the duct with the following coordinates $p_{yz}(0.5, 0.5)$ (a), in the proximity of the Shercliff wall with the following coordinates $p_{yz}(0.5, 0.1)$ (b), and in the proximity of the Hartmann wall with the following coordinates $p_{yz}(0.1, 0.5)$ (c). The following indication is used: (—) - $Ha = 0$, (—) - $Ha = 21.2$, $C_d = 0$, (—) - $Ha = 21.2$, $C_d = 0.1$, (—) - $Ha = 21.2$, $C_d = 0.15$, (—) - $Ha = 21.2$, $C_d = 0.25$, (—) - $Ha = 21.2$, $C_d \to \infty$,

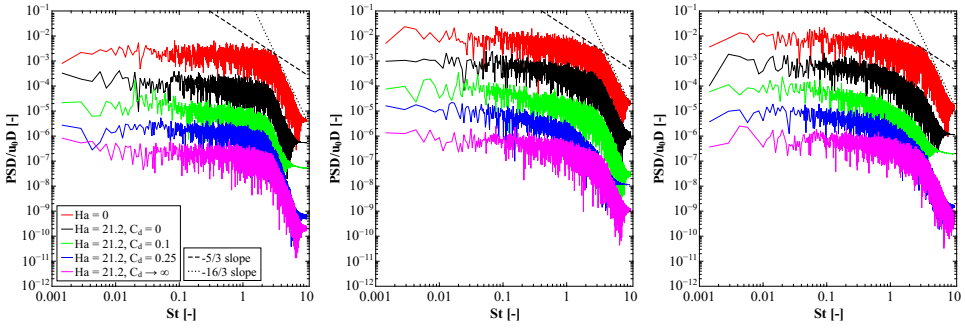

Figure 4.15: The power spectral density of the non-dimensional instantaneous streamwise (x-component) velocity for different values of C_d at locations shown in the previous figure. Note that due to better visibility, the vertical axis was shifted down for one decade for each consecutive plot.

4.5. SUMMARY AND CONCLUSION

We have performed a numerical study of the turbulent magnetohydrodynamic square duct flow with arbitrary electrically conducting Hartmann walls subjected to a transverse uniform magnetic field. We have assumed the one-way coupling between the fluid flow and imposed magnetic field, and have applied Large Eddy Simulation with the dynamic Smagorinsky subgrid closure to account for the turbulence. We have varied the typical wall conductance ratio over a wide range of $0 \leq C_d \rightarrow \infty$, for fixed values of the Reynolds ($Re = 5602$) and Hartmann ($Ha = 21.2$) numbers (both selected to provide a fully developed turbulence regime). The variation of the electrical conductance of the Hartmann walls has introduced significant flow and turbulence reorganization, which can be classified into the following three stages. The first stage corresponds to the $0 \leq C_d < 0.15$ range, and was characterized by a gradual suppression of the velocity fluctuations and appearance of the patterned turbulence clusters in the vicinity of the Shercliff walls. The second stage was obtained at $C_d = 0.15$, when a full flow laminarization occurred. The final third stage was obtained in the $0.15 < C_d \rightarrow \infty$ range, when a turbulence regeneration (triggered in the regions between the Hartmann walls and the duct center) and sustenance was observed.

The flow morphology, including the secondary flow patterns, went through significant alternation along all three stages. The analysis of the turbulent kinetic energy budgets have provided detailed insight into mechanisms behind the MHD induced flow relaminarization and final turbulence regeneration (i.e. due to the interplay between the flow reorganization and local distribution of the current density). For the perfectly electrically conducting Hartmann walls, the turbulence reached level close to the non-MHD situation (i.e. $Ha = 0$), confirming the full turbulence regeneration after an initial MHD induced suppression. The maximum of the turbulence anisotropy was reached at $C_d = 0.05$ and $C_d = 0.25$ in proximities of the Hartmann and Shercliff walls, respectively. The slopes of the power spectra density distributions were mostly affected in the intermediate range of C_d in the proximity of the Hartmann walls. The provided numerical results also intended to motivate additional experimental studies in the similar range of the Re/Ha working parameters to provide the final answers on turbulence regeneration triggered by the changes of the electrical conductance of the Hartmann walls. The importance of the finite electrical conductance of the Hartmann walls can find direct applications in the flow and turbulence control during the continuous casting and in liquid metal blankets of the new generation of the fusions reactors.

REFERENCES

[1] J. Hartmann and F. Lazarus, *Theory of the laminar flow of an electrically conducting liquid in an homogeneous magnetic field,* Kongelige Danske Videnskabernes Selskab Matematisk **15**, 1 (1937).

[2] H.Alfven, *Existence of electromagnetic-hydrodynamic waves,* Nature **150**, 405 (1942).

[3] L. Bühler, *Liquid metal magnetohydrodynamics for fusion blankets,* in *Magnetohydrodynamics: Historical Evolution and Trends* (Springer Netherlands, 2007) pp. 171–194.

[4] C. Mistrangelo, L. Bühler, C. Koehly, and I. Ricapito, *Magnetohydrodynamic velocity and pressure drop in manifolds of a WCLL TBM,* Nuclear Fusion **61**, 096037 (2021).

[5] S. Smolentsev, *Physical background, computations and practical issues of the magnetohydrodynamic pressure drop in a fusion liquid metal blanket,* Fluids **6**, 110 (2021).

[6] B. G. Thomas and R. Chaudhary, *State of the art in electromagnetic flow control in continuous casting of steel slabs: Modeling and plant validation,* 6th International Conference on Electromagnetic Processing of Materials EPM (2009).

[7] S.-M. Cho and B. G. Thomas, *Electromagnetic forces in continuous casting of steel slabs,* Metals **9**, 471 (2019).

[8] N.-T. Nguyen, *Micro-magnetofluidics: Interactions between magnetism and fluid flow on the microscale,* Microfluidics and Nanofluidics **12**, 1 (2012).

[9] A. Ortiz-Pérez, V. García-Ángel, A. Acuña-Ramírez, L. Vargas-Osuna, J. Pérez-Barrera, and S. Cuevas, *Magnetohydrodynamic flow with slippage in an annular duct for microfluidic applications,* Microfluidics and Nanofluidics **21**, 1 (2017).

[10] X. Wang, H. Xu, and H. Qi, *Transient magnetohydrodynamic flow and heat transfer of fractional Oldroyd-B fluids in a microchannel with slip boundary condition,* Physics of Fluids **32**, 103104 (2020).

[11] O. Zikanov, D. Krasnov, T. Boeck, A. Thess, and M. Rossi, *Laminar-turbulent transition in magnetohydrodynamic duct, pipe, and channel flows,* Applied Mechanics Reviews **6**, 030802 (2014).

[12] P. A. Davidson, *An Introduction to Magnetohydrodynamics*, Cambridge Texts in Applied Mathematics (Cambridge University Press, 2001).

[13] S. Kenjereš, *On modeling and eddy-resolving simulations of flow, turbulence, mixing and heat transfer of electrically conducting and magnetizing fluids: A review,* International Journal of Heat and Fluid Flow **73**, 270 (2018).

[14] S. Kenjereš and K. Hanjalić, *On the implementation of effects of Lorentz force in turbulence closure models,* International Journal of Heat and Fluid Flow **21**, 329 (2000).

[15] S. Smolentsev and R. Moreau, *One-equation model for quasi-two-dimensional turbulent magnetohydrodynamic flows,* Physics of Fluids **19**, 078101 (2007).

[16] O. Widlund, S. Zahrai, and F. H. Bark, *Development of a Reynolds stress closure for modeling of homogeneous MHD turbulence,* Physics of Fluids **10**, 1987 (1998).

[17] X. Miao, K. Timmel, D. Lucas, Z. Ren, S. Eckert, and G. Gerbeth, *Effect of an electromagnetic brake on the turbulent melt flow in a continuous-casting mold,* Metallurgical and Materials Transactions B **43**, 954 (2012).

[18] S. Kenjereš, K. Hanjalić, and D. Bal, *A direct-numerical-simulation-based second-moment closure for turbulent magnetohydrodynamic flows,* Physics of Fluids **16**, 1229 (2004).

[19] H. Kobayashi, *Large eddy simulation of magnetohydrodynamic turbulent channel flows with local subgrid-scale model based on coherent structures,* Physics of Fluids **18**, 045107 (2006).

[20] D. Krasnov, O. Zikanov, J. Schumacher, and T. Boeck, *Magnetohydrodynamic turbulence in a channel with spanwise magnetic field,* Physics of Fluids **20**, 095105 (2008).

[21] R. Chaudhary, S. P. Vanka, and B. G. Thomas, *Direct numerical simulations of magnetic field effects on turbulent flow in a square duct,* Physics of Fluids **22**, 075102 (2010).

[22] D. Krasnov, O. Zikanov, and T. Boeck, *Numerical study of magnetohydrodynamic duct flow at high Reynolds and Hartmann numbers,* Journal of Fluid Mechanics **704**, 421–446 (2012).

[23] D. Krasnov, A. Thess, T. Boeck, Y. Zhao, and O. Zikanov, *Patterned turbulence in liquid metal flow: Computational reconstruction of the Hartmann experiment,* Phys. Rev. Lett. **110** (2013).

[24] O. Zikanov, D. Krasnov, Y. Li, T. Boeck, and A. Thess, *Patterned turbulence in spatially evolving magnetohydrodynamic duct and pipe flows,* Theoretical and Computational Fluid Dynamics **28**, 319 (2013).

[25] O. Zikanov, D. Krasnov, T. Boeck, and S. Sukoriansky, *Decay of turbulence in a liquid metal duct flow with transverse magnetic field,* Journal of Fluid Mechanics **867**, 661–690 (2019).

[26] Y. Yang, W. H. Matthaeus, Y. Shi, M. Wan, and S. Chen, *Compressibility effect on coherent structures, energy transfer, and scaling in magnetohydrodynamic turbulence,* Physics of Fluids **29**, 035105 (2017).

[27] A. De Rosis, R. Liu, and A. Revell, *One-stage simplified lattice Boltzmann method for two-and three-dimensional magnetohydrodynamic flows,* Physics of Fluids **33**, 085114 (2021).

[28] J. C. R. Hunt, *Magnetohydrodynamic flow in rectangular ducts,* Journal of Fluid Mechanics **21**, 577–590 (1965).

[29] A. Sterl, *Numerical simulation of liquid-metal MHD flows in rectangular ducts,* Journal of Fluid Mechanics **216**, 161–191 (1990).

[30] T. Arlt, J. Priede, and L. Bühler, *The effect of finite-conductivity Hartmann walls on the linear stability of Hunt's flow,* Journal of Fluid Mechanics **822**, 880–891 (2017).

[31] A. Thomas and L. Bühler, *Numerical simulations of time-dependent hunt flows with finite wall conductivity,* Magnetohydrodynamics **55**, 319 (2019).

[32] L. Bühler, T. Arlt, T. Boeck, L. Braiden, V. Chowdhury, D. Krasnov, C. Mistrangelo, S. Molokov, and J. Priede, *Magnetically induced instabilities in duct flows,* IOP Conference Series: Materials Science and Engineering **228**, 012003 (2017).

[33] K. Zhang, M. Weeks, and P. Roberts, *Effect of electrically conducting walls on rotating magnetoconvection,* Physics of Fluids **16**, 2023 (2004).

[34] A. T. Akinshilo, *Mixed convective heat transfer analysis of MHD fluid flowing through an electrically conducting and non-conducting walls of a vertical micro-channel considering radiation effect,* Applied Thermal Engineering **156**, 506 (2019).

[35] A. Blishchik and S. Kenjereš, *Observation of a novel flow regime caused by finite electric wall conductance in an initially turbulent magnetohydrodynamic duct flow,* Physical Review E **104**, L013101 (2021).

[36] J. Smagorinsky, *General circulation experiments with the primitive equations: I. The basic experiment,* Monthly Weather Review **91**, 99 (1963).

[37] J. Mao, K. Zhang, and K. Liu, *Comparative study of different subgrid-scale models for large eddy simulations of magnetohydrodynamic turbulent duct flow in OpenFOAM,* Computers and Fluids **152**, 195 (2017).

[38] D. K. Lilly, *A proposed modification of the Germano subgrid-scale closure method,* Physics of Fluids A: Fluid Dynamics **4**, 633 (1992).

[39] A. Blishchik, M. van der Lans, and S. Kenjereš, *An extensive numerical benchmark of the various magnetohydrodynamic flows,* International Journal of Heat and Fluid Flow **90**, 108800 (2021).

[40] H. G. Weller, G. Tabor, H. Jasak, and C. Fureby, *A tensorial approach to computational continuum mechanics using object-oriented techniques,* Computers in Physics **12**, 620 (1998).

[41] M.-J. Ni, R. Munipalli, P. Huang, N. B. Morley, and M. A. Abdou, *A current density conservative scheme for incompressible MHD flows at a low magnetic Reynolds number. Part II: On an arbitrary collocated mesh,* Journal of Computational Physics **227**, 205 (2007).

[42] N. Weber, P. Beckstein, V. Galindo, M. Starace, and T. Weier, *Electro-vortex flow simulation using coupled meshes,* Computers and Fluids **168**, 101 (2018).

[43] R. Issa, A. Gosman, and A. Watkins, *The computation of compressible and incompressible recirculating flows by a non-iterative implicit scheme,* Journal of Computational Physics **62**, 66–82 (1986).

[44] S. Gavrilakis, *Numerical simulation of low-Reynolds-number turbulent flow through a straight square duct,* Journal of Fluid Mechanics **244**, 101 (1992).

[45] J. L. Lumley, *Computational modeling of turbulent flows,* Advances in Applied Mechanics **18**, 123 (1979).

[46] S. Kenjereš, *Energy spectra and turbulence generation in the wake of magnetic obstacles,* Physics of Fluids **24**, 115111 (2012).

5

EFFECTS OF ELECTRICALLY CONDUCTIVE WALLS ON A TURBULENT MAGNETOHYDRODYNAMIC FLOW IN A CONTINUOUS CASTING MOLD

In the present chapter, we have performed a series of numerical simulations of the turbulent liquid metal flow in a laboratory-scale setup of the continuous casting. The liquid metal flow was subjected to an external non-uniform magnetic field reproducing a realistic electromagnetic brake (EMBr) effect. The focus of this chapter was on the effects of the finite electrical conductivity of Hartmann walls on the flow and turbulence in the mold. The results obtained for the neutral (non-MHD) and MHD cases over a range of the imposed EMBr strengths - all for the perfectly electrically insulated walls - were compared with the available Ultrasound Doppler Velocimetry (UDV) measurements. A good agreement between simulations and experiments was obtained for all simulated cases. Next, we completed a series of simulations including a wide range of the finite electrical conductivities (ranging from weakly to perfectly conducting wall conditions) of the Hartmann walls for a fixed value of the imposed EMBr. The obtained results demonstrated a significant influence of the electric wall conductivities on the flow and turbulence reorganization.

Published as: A. Blishchik, I. Glavinić, T. Wondrak, D. van Odyck, S. Kenjereš, Effects of electrically conductive walls on turbulent magnetohydrodynamic flow in a continuous casting mold, International Journal of Heat and Fluid Flow 95, 108967, 2022, doi: 10.1016/j.ijheatfluidflow.2022.108967

5.1. INTRODUCTION

Steel casting is one of the most important industrial processes that fills humanity's needs in this material widely used in a range of technological applications. Nowadays, the great majority of the produced steel is obtained with continuous casting (CC) technology. Although the continuous casting has been actively used since the 1950s, incessant efforts to improve the efficiency of the entire process and specific crucial parts are being made. One of these crucial parts is the transport of the highly turbulent liquid metal flow from a tundish to a casting mold through a submerged entry nozzle. It is recognized that various destructive phenomena occurring in the mold are responsible for a significant reduction of the product quality [1]. These phenomena include excessively strong double-roll flow patterns or entrainment and entrapping of the slag particles from the mold free-surface. To make such a sensitive process more stable, several control tools, including in particular, the electromagnetic brake (EMBr), are used. The application of the electromagnetic brake, as an elegant non-invasive Magnetohydrodynamics (MHD) based control mechanism, is possible because of a high electrical conductivity of the liquid steel ($\sigma = \mathcal{O}(10^6)$ S/m), which will produce electric current within the fluid when subjected to an external magnetic field. Finally, interactions of the generated electric current and imposed magnetic field will produce a Lorentz force which will locally affect the velocity field, [2–4].

Experimental studies of the MHD phenomena of continuous casting are challenging due to the presence of extremely high temperatures of the liquid steel (approx. 1500°C). To circumvent these high temperatures, experiments utilizing alloys (such as galinstan, GaInSn) that are in a liquid state at room temperatures are designed, [5]. The remaining problem with this and similar alloys is their opaqueness, which prevents them from applications of the classic laser optics diagnostics tools such as Laser Doppler Anemometry (LDA) and Particle Imaging Velocimetry (PIV).

Despite numerous challenges, significant research progress was made during the last decade. Many numerical and experimental studies focusing on the EMBr mechanism have been reported in the literature. In the numerical studies of [6], Large Eddy Simulation (LES) method was used to analyze the effects of the EMBr vertical position. It was demonstrated that by applying a magnetic field across the port stronger jets were created, while a double-ruler brake significantly suppressed turbulence intensity. Effects of the imposed magnetic field strength and depth of the submerged nozzle were numerically investigated in [7]. When the magnetic field strengthened, the typical double-roll flow pattern was moved up, whereas the deeper SEN resulted in moving these rolls down. An interesting combination of the LES and a zero-dimensional model was applied in numerical studies of the origin of the self-sustained oscillations in a thin cavity mimicking the simplified continuous casting setup, [8]. The multi-phase simulations of effects of the argon bubbles injection on the removal of the inclusion at the meniscus (top surface) were investigated in [9] and [10]. It was shown that the injection of smaller bubbles resulted in larger inclusions. Furthermore, by increasing the flow rate of injected bubbles the meniscus velocity was also increased.

In [11] authors reported on experiments with the Ultrasound Doppler Velocimetry (UDV) sensors, which they used to analyze the specific nozzle shape in generating a swirling flow. The same measuring technique was also used in [12] where the focus was on the imposed magnetic field effects on the resulting flow structure and turbulence. To be able to track the presence of the injected argon bubbles in the mold, a novel magnetic induction tomography (MIT) experimental technique was introduced in [13]. The improved multi-phase capabilities of the MIT sensors, able to provide both the phase and amplitude data, were recently reported in [14]. Considering the control theory, the initial attempts of creating the control loop for the continuous casting process were mainly focused on maintaining the level of the liquid metal in the mold, [15]. In the more recent work of [16], the concept of the industrial real-time controller, capable of adjusting flow structure, was proposed.

It should be noted that in a great majority of studies reported in the literature dealing with continuous casting assumed the presence of the fully electrically insulated walls. However, in the real-scale industrial continuous-casting mold, working conditions can significantly deviate from this assumption (e.g. due to a formation of the solidifying shells in the proximity of the walls). A very few numerical and experimental studies addressed the effects of the electric wall conductivities, e.g.[17], [18]. In these studies, a single value of the characteristic ratio of the wall/fluid conductivities was considered, and it was concluded that a finite wall conductivity had a significant impact on the flow. The effects of different configurations of the wide and narrow conductive walls in a continuous-casting mold were numerically investigated in [19]. The authors considered also a single value of the finite wall conductivity ratio in addition to perfectly insulated and perfectly conductive walls. The turbulent flow in the mold was reported to be strongly suppressed in the case of the conductive walls. The impact of the various imposed magnetic field strengths on the meniscus flow in a continuous-casting mold was presented in [20]. Again, the walls with just a single value of the characteristic wall conductivity ratio were used. The strong effect of the meniscus flow acceleration and braking was demonstrated depending on the strength of the imposed magnetic field. For generic MHD configurations (i.e. flows in rectangular channels or pipes), it was demonstrated that a change of the wall conductance can have significant impact on the flow and turbulence reorganization, as shown in [21],[22], [23], [24]. This lack of a wider range of studies dealing with the effects of the electrically conducting walls is associated with partial challenges in creating and executing proper working conditions. The experimental difficulties are associated with a necessity to have a complex multi-modular structure of the setup allowing a simple replacement of the walls. For the computer simulations, the particular challenges are in the necessity to integrate both fluid and solid wall domains (so-called conjugate MHD [25]), which requires the development of advanced numerical algorithms.

In the present work, to fill the existing gap in the literature regarding the possible effects of the finite wall conductivity ratios on the flow and turbulence reorganization, we

will perform a series of numerical simulations of an existing laboratory-scale continuous casting setup. Currently, the wall conductivity ratio is not considered as a control mechanism in a real continuous casting process. However, we will demonstrate that accounting for various values of the wall conductivity ratio at the design stage of a CC setup can significantly change the flow pattern. First, we will perform simulations of the non-MHD case and MHD case with perfectly electrically insulated walls over a range of EMBr (i.e. different values of the imposed current to generate localized spatial distribution of the magnetic field) and will compare results with the available experimental data. Second, we will perform a detailed parametric study of various electric conductivities of the Hartmann walls for a fixed value of the EMBr strength, and will report on the flow and turbulence reorganization.

5.2. GOVERNING EQUATIONS AND NUMERICAL DETAILS

5.2.1. GOVERNING EQUATIONS FOR A TURBULENT ONE-WAY COUPLED MHD FLOW

An incompressible single-phase electrically conductive fluid is considered. The fluid is subjected to the external constant non-uniform magnetic field resulting in the appearance of the contributing Lorentz force. The flow of an electrically conducting fluid can be described by conservation of the mass and momentum, as follows:

$$\nabla \cdot \mathbf{U} = 0 \tag{5.1}$$

$$\frac{\partial \mathbf{U}}{\partial t} + (\mathbf{U} \cdot \nabla)\mathbf{U} = -\frac{1}{\rho}\nabla p + \nu \nabla^2 \mathbf{U} + \frac{1}{\rho}\mathbf{F_L} \tag{5.2}$$

where $\mathbf{U}$ is velocity, p is pressure, ν is the kinematic viscosity, ρ is density, and $\mathbf{F_L}$ is the Lorentz force. The liquid metal flow in continuous casting mold is expected to be highly turbulent $\left(Re = \mathcal{O}(10^4 - 10^5)\right)$, and special attention should be devoted to the correct turbulence prediction. In the present study, we adopt the dynamic Large Eddy Simulation (LES) approach. In the LES, spatially filtered governing equations Eqn. (5.1) and Eqn. (5.2) can be written as:

$$\nabla \cdot \overline{\mathbf{U}} = 0 \tag{5.3}$$

$$\frac{\partial \overline{\mathbf{U}}}{\partial t} + \left(\overline{\mathbf{U}} \cdot \nabla\right)\overline{\mathbf{U}} = -\frac{1}{\rho}\nabla \overline{p}^* + \nu \nabla^2 \overline{\mathbf{U}} - \nabla \cdot \overline{\overline{\tau}}_{sgs} + \frac{1}{\rho}\overline{\mathbf{F}}_{\mathbf{L}} \tag{5.4}$$

where $(\overline{\overline{\tau}}_{sgs})$ is the sub-grid scale (SGS) stress tensor, ('–') is the spatially filtered value, and $\overline{p}^* = \overline{p} + \frac{1}{3}\tau' \mathbf{I}$ is the modified pressure. In order to close Eqn. (5.4), the linear dependency of the SGS stress tensor on the strain rate is introduced:

$$\tau_{ij}^{sgs} = -2\nu_{sgs}\overline{S_{ij}}, \;\; \nu_{sgs} = (C_S \Delta)^2 \left(2\overline{S}_{ij}\overline{S}_{ij}\right)^{\frac{1}{2}} \tag{5.5}$$

where C_s is the Smagorinsky coefficient, $\overline{S}_{ij}$ is the strain rate tensor, ν_{sgs} is the sub-grid scale turbulent viscosity. Assuming C_s to be a constant would be not correct, considering the strong influence of the magnetic field on the flow fluctuations, [26]. Hence, the dynamic approach proposed by Lily [27], representing the local calculation of C_s, is applied as follows:

$$C_S^2 = \frac{1}{2}\frac{\langle\langle L_{ij}M_{ij}\rangle\rangle}{\langle\langle M_{ij}M_{ij}\rangle\rangle} \tag{5.6}$$

$$L_{ij} = \widetilde{\overline{U}_i\overline{U}_j} + \widetilde{\overline{U}}_i\widetilde{\overline{U}}_j \tag{5.7}$$

$$M_{ij} = \Delta^2\widetilde{\overline{S}\overline{S}_{ij}} + \widetilde{\Delta^2}\widetilde{\overline{S}}\widetilde{\overline{S}}_{ij} \tag{5.8}$$

where Δ is the main filter ($\Delta = (\Delta_x\Delta_y\Delta_z)^{1/3}$), $\widetilde{\Delta}$ is the second filter ($\widetilde{\Delta} = 2\Delta$) and '$\langle\langle ...\rangle\rangle$' indicates the local spatial averaging operation over the cell faces.

The accounting of the MHD interactions is accomplished through the Lorentz force term, formulated as:

$$\overline{\mathbf{F}}_\mathbf{L} = \bar{\mathbf{J}} \times \mathbf{B} \tag{5.9}$$

where $\bar{\mathbf{J}}$ is the current density, and $\mathbf{B}$ is the constant imposed magnetic field. To calculate the new additional unknown variable $\bar{\mathbf{J}}$, we refer to the liquid metal nature of the fluid implying the extremely high magnetic diffusion and subsequently the very low magnetic Reynolds number:

$$Re_m = \frac{UD}{\lambda} << 1 \tag{5.10}$$

where Re_m is the magnetic Reynolds number, D is the characteristic length and λ is the magnetic diffusion. Following the statement in Eqn. 5.10, the one-way coupling MHD approach can be applied starting from the Ohm law for the moving conducting fluid as:

$$\bar{\mathbf{J}} = \sigma\left(-\nabla\overline{\phi} + \overline{\mathbf{U}} \times \mathbf{B}\right) \tag{5.11}$$

where σ is the electrical conductivity of the fluid and $\overline{\phi}$ is the electric potential. By substituting the divergence-free condition for the current density into Eqn. (5.11), the Poisson equation for the electric potential can be formulated as:

$$\nabla^2\overline{\phi} = \nabla\cdot\left(\overline{\mathbf{U}} \times \mathbf{B}\right) \tag{5.12}$$

The pressure-driven MHD flows are defined with two characteristic non-dimensional numbers, Reynolds and Hartmann numbers that are calculated as:

$$Re = \frac{UD}{\nu}, \quad Ha = BD\sqrt{\frac{\sigma}{\rho\nu}} \tag{5.13}$$

To conserve $\bar{\mathbf{J}}$, the Four Steps Projection Method (FSPM), proposed by [28], is implemented in our code. Further key details of the numerical implementation are given in our recent work [23].

5.2.2. MODELING OF THE FINITE ELECTRICALLY CONDUCTIVE WALLS

Taking into account the finite electrical conductivity and finite thickness of surrounding walls is not a trivial task, and requires a specific approach aimed at predicting the electric potential and current density transfer between fluid and wall domains. In the present study, we use our recently developed conjugate MHD method. Here, a brief summary of this approach is provided, while the complementary steps of the algorithm, as well as the thorough validation, can be found in [23]. The conjugate MHD method is generally based on splitting fluid and wall regions into different computation domains, where the Poisson's equation for the electric potential in different domains is formulated as:

$$\nabla \cdot \left(\sigma_L \nabla \overline{\phi}_L \right) = \nabla \cdot \left(\sigma_L \left(\overline{\mathbf{U}} \times \overline{\mathbf{B}} \right) \right) \tag{5.14}$$

$$\nabla \cdot \left(\sigma_S \nabla \overline{\phi}_S \right) = 0 \tag{5.15}$$

where subscripts L and S indicate the liquid and solid domain, respectively. The specific weighted flux interpolation scheme is used to obtain the electric potential at the interface, [29]:

$$\overline{\phi}_{i[L,S]} = w\overline{\phi}_L + (1-w)\overline{\phi}_S, \quad w = \frac{r_S \sigma_L}{r_L \sigma_S + r_S \sigma_L} \tag{5.16}$$

where r is the corresponding first cell-center distance from the interface. For the conjugate MHD problems, it is convenient to introduce additional non-dimensional parameter (C_d)) representing the characteristic electrical conductivities and thickness ratios as:

$$C_d = \frac{\sigma_S d_w}{\sigma_L D} \tag{5.17}$$

where d_w is the characteristic thickness of the wall and D is the characteristic length-scale of the fluid domain.

5.2.3. THE COMPUTER CODE

To carry out the simulations, we used our in-house finite-volume MHD solver based on the open-source library OpenFOAM [30]. The solver includes all described conjugate MHD equations, [23]. The spatial discretization for the convective and diffusive term is performed by using the second-order central differencing scheme (CDS), while the second-order temporal discretization is accomplished by using the backward scheme. The PISO algorithm [31] is applied to couple pressure and velocity fields.

5.3. MINI-LIMMCAST SETUP AND BOUNDARY CONDITIONS

5.3.1. EXPERIMENTAL SETUP

In the present study, the geometry used for the numerical simulations is based on the most recent version of the laboratory-scaled mold of a continuous caster at Mini-LIMMCAST

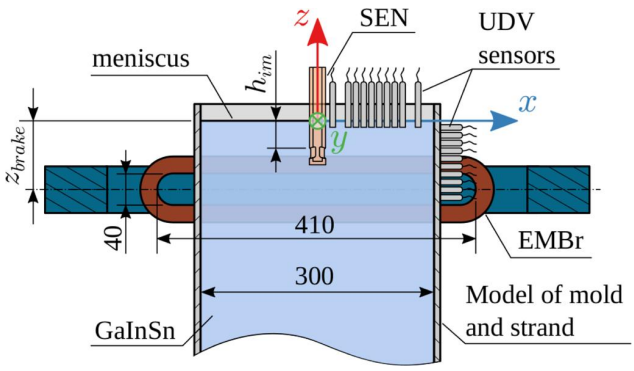

Figure 5.1: Sketch of the experimental setup, [32]. Note that the setup dimensions are defined in millimeters.

(Liquid Metal Model for Continuous Casting) facility located at Helmholtz–Zentrum Dresden–Rossendorf (HZDR), [32]. The experimental details are only briefly provided here, while the detailed information is available in [32]. The eutectic alloy galinstan (GaInSn) is used as a model of liquid steel since it is liquid at room temperature, and has similar physical and electrical properties to liquid steel. Liquid metal is continuously driven from the reservoir to the tundish, where it enters the mold through the submerged entry nozzle (SEN), and then moves back to the reservoir. The flow rate through the SEN is controlled by the stopper rod, while the liquid metal level in the mold is kept constant. Two coils, one adjacent to each wide face of the mold, generate the electromagnetic braking (EMBr) effect 0.075 m below the free surface, Fig. 5.1. The strength of the generated magnetic field depends on the electric current through the coils and can reach up to $B = 0.4$ T for the maximum current of $I = 600$ A. Walls in the experiment are considered as electrically insulated, i.e. $C_d = 0$. Velocity measurements are performed by using Ultrasound Doppler Velocimetry (UDV) with an array of ten ultrasound transducers on the upper part of the narrow wall. One should take into account that UDV can measure the velocity along the entire length of the beam but only the component in the axial direction of each transducer (the x-component for the present case) and the velocities are spatially averaged depending on the diameter of the ultrasound beam (which is 8 mm for the present setup).

5.3.2. NUMERICAL SETUP

There is no need to consider a tundish and a reservoir in the numerical study, and consequently, the setup can be greatly simplified. The numerically simulated Mini-LIMMCAST domain will include the submerged entry nozzle with a bifurcated port and a rectangular mold, as shown in Fig. 5.2(a). The numerically simulated geometry is identical to the experimental setup: (i) the distance from the outlet to the meniscus $L = 0.612$ m, (ii) the width of the mold $W = 0.3$ m, (iii) the half-thickness of the mold $D = 0.0175$ m. It is important to note that these dimensions are valid only in the case of the electrically

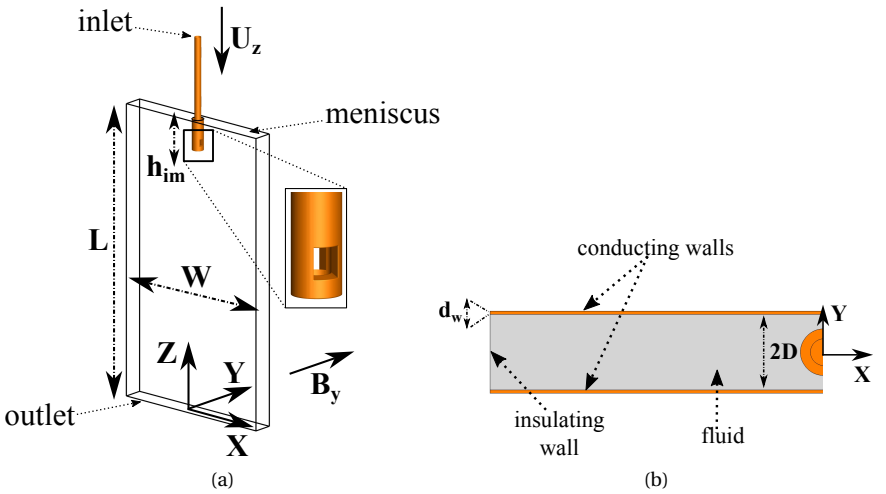

Figure 5.2: Sketch of the numerical setup: (a) a side view of the entire mold, (b) a top view (from meniscus) of the mold (note that only half of domain is shown).

5

insulated solid walls. By inserting inside the mold two finite, electrically conducting, and perpendicular to the y-direction walls with the finite wall thickness $d_w = 5 \times 10^{-4}$ m, resulting half-thickness of the mold will be reduced to $D = 0.017$ m, Fig. 5.2(b). The SEN immersion depth $h_{im} = 0.35$ m remains constant. The numerically simulated port shapes are slightly less round than in original experiments resulting in a superior mesh quality (much less skewed control volume mesh in the proximity of the port). Note that this slight change of the port shape has not produced any notable changes in the flow and turbulence predictions.

5.3.3. MESH AND BOUNDARY CONDITIONS

The constant flow rate obtained from the experiment $Q_{flow} = 7.17 \times 10^{-5}$ m^3/s is imposed at the inlet, and the zero-pressure boundary condition at the outlet. Although the bifurcated port is a natural turbulence generator, the turbulent structures need to be initialized before the port to mimic the real conditions where the flow is already turbulent in the SEN because of the flow disturbances generated by the stopper rod. In the present chapter, a fully developed turbulence state is obtained by imposing periodic boundary conditions at the upper part of the inlet segment. The no-slip velocity boundary condition is applied at all walls. The meniscus is modeled by imposing the slip boundary conditions. This approach proved to be the most numerically efficient and accurate because of a relatively small free-surface deformation observed in the experiments. We also conducted a series of additional test simulations to ensure that the meniscus fluctuations were marginal. These results are presented in Appendix A. Lastly, to generate electro-magnetic braking in the mold, the external magnetic field spatial distribution

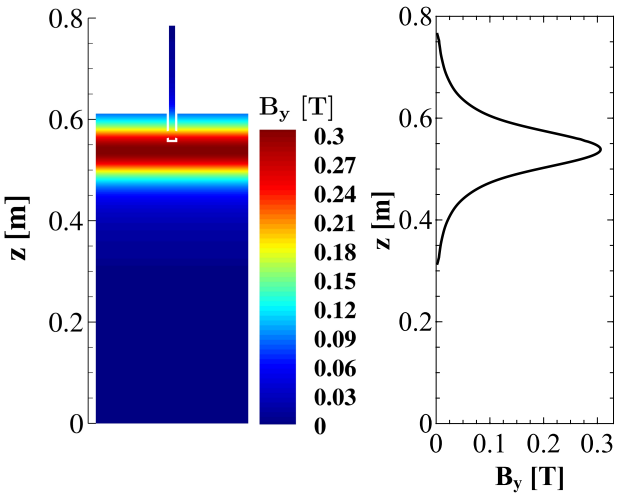

(a) (b)

Figure 5.3: (a) The contours of the B_y component of the magnetic field in the central vertical cross-section ($y = 0$ m); (b) the vertical profile of the B_y component of the magnetic field; Note that shown magnetic field is for imposed electric current of $I = 375$ A.

Table 5.1: List of simulations performed in the present study.

Group	Re	Ha	EMBr (in A)	C_d (Hartmann walls)
I	32000	0	0	0
		68	100	0
		142	225	0
		210	375	0
II	32000	142	225	0.025
		142	225	0.05
		142	225	0.1
		142	225	0.15
		142	225	0.2
		142	225	0.5
		142	225	1
		142	225	5
		142	225	∞

is imposed based on the measured B_y component of the external magnetic field in the z-coordinate direction, as indicated in Fig. 5.3.

We divide our simulations into two groups. The first group includes the electrically

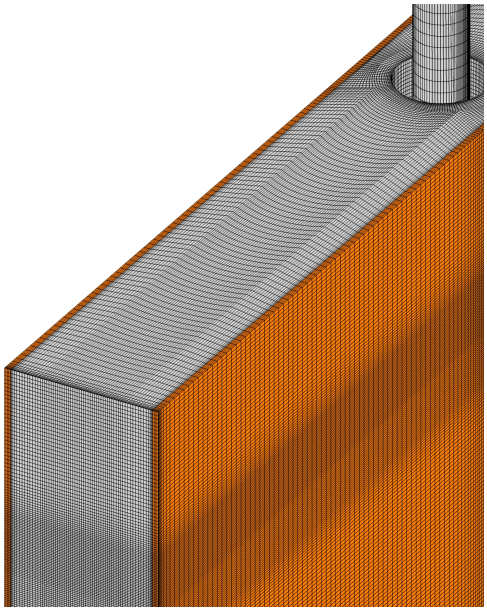

Figure 5.4: The numerical mesh in the upper-left part of the mold. The fluid region is colored by grey, the solid region is colored by orange.

insulating walls ($C_d = 0, \partial\phi/\partial n = 0$) and direct comparisons with the experiments over a range of imposed electric current ($0 \le I \le 375$ A) and resulting magnetic field strength ($0 \le Ha \le 210$). The second group of simulations includes activation of the conjugate MHD where the electrical conductance of the Hartmann walls is varied over a wide range of the conductance wall parameter ($0.025 \le C_d \le 5$) with a fixed value of the imposed current of $I = 225$ A. Note that the wall conductivity ratio of the solidifying shell forming on the walls during the real size caster is $C_d \approx 0.125$. Additionally, the extreme case with $C_d \to \infty$ is considered as well (where $\phi = 0$ boundary condition is imposed), indicating the fully electrically conducting walls. The experimental data are not available for the second group of simulations but generated numerical results are intended to guide the design of a new generation of experimental setups with a finite conductance of the Hartmann walls. An overview of performed simulations is given in table 5.1.

For the conjugate MHD cases (i.e. a finite C_d), the computational domain contains the fluid occupying and solid-wall (two Hartmann walls) regions. ICEM CFD meshing software is used to generate a block-structured non-uniform mesh containing regular hexagonal control volumes (CVs). The fluid domain is represented by $M_L \approx 4 \times 10^6$ control volumes (29 nodes across the port in the horizontal direction), while the solid-wall domain contains $M_S \approx 5 \times 10^5$ control volumes, Fig. 5.4. The mesh refinement is applied in the proximity of the walls, meniscus at the top, as well as around the entrance ports of the nozzle. In the present study, we apply the Spalding wall functions for the

wall treatment [33]. To check the grid dependency of obtained solutions two additional numerical meshes are also considered: the coarse mesh, with $M_{L,coarse} \approx 2 \times 10^6$ CVs (15 nodes across the port in the horizontal direction), the fine mesh $M_{L,fine} \approx 6 \times 10^6$ CVs (45 nodes across the port in the horizontal direction), Appendix B. The Courant number $Co = (\Delta t/2V) \sum_{faces} |\psi_i| \approx 1$ is kept for all simulations (note that V is the cell volume and ψ is the face volumetric flux).

5.4. RESULTS AND DISCUSSION

5.4.1. VALIDATION WITH THE EXPERIMENT FOR THE ELECTRICALLY INSULATED WALLS

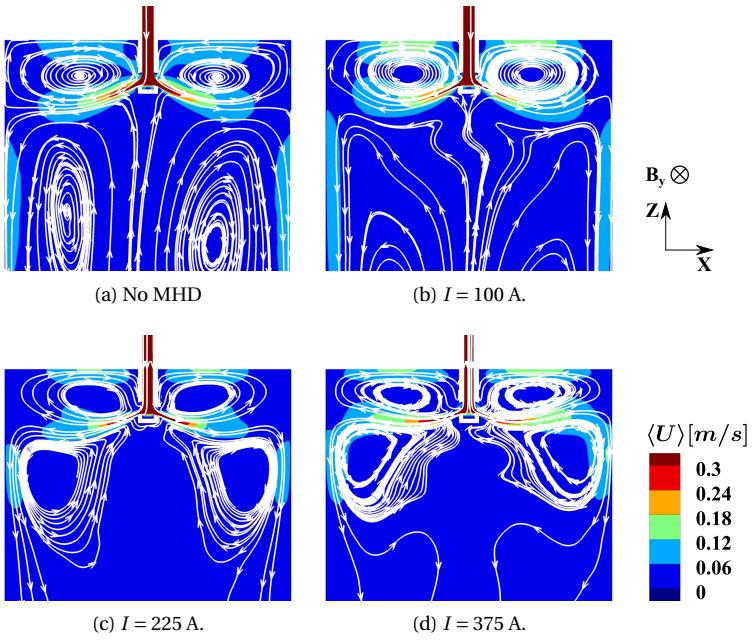

(a) No MHD (b) $I = 100$ A.

(c) $I = 225$ A. (d) $I = 375$ A.

Figure 5.5: The contours of time-averaged velocity magnitude superimposed with the velocity streamlines (white lines) in the central vertical ($y = 0$ m) cross-section (upper half of the mold) for the range of EMBr strength and fixed $C_d = 0$ (electrically insulated walls).

We start our analysis by comparing numerical simulations and experimental results for cases with the electrically insulated walls (group I results as listed in Table 5.1). The most salient long-term averaged flow features are shown in Fig. 5.5, where we select the central vertical cross-section and superimpose the streamlines and contours of the velocity magnitude for various strengths of the imposed EMBr (i.e. $0 \leq I \leq 375$ A). To obtain a reliable convergence of the first- and second-moments of the velocity field statistics, we perform averaging over 120 s after the initial flow establishment. This period equals

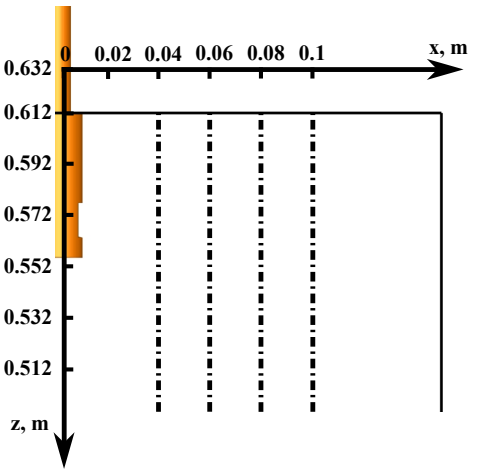

Figure 5.6: A sketch of the locations in the central-vertical plane (y = 0 m) for which characteristic velocity profiles are extracted along the following coordinates: x = 0.04, 0.06, 0.08 and 0.1 m.

to approximately 3 days of real-time using 96 cores of 2.6 GHz Intel Xeon E5-2697A v4. It can be seen that flow has a typical double-roll structure in the upper and lower parts of the mold. By imposing the electric current of I = 100A, Fig. 5.5(b), the centers of the lower rolls are more shifted in the negative z-direction compared to the neutral case, Fig. 5.5(a), while the upper rolls stay unaffected. With further increase of the applied current, the lower rolls are significantly reduced and their centers are moved closer to the inlet port, Figs. 5.5(c),(d). In contrast, locations of centers of upper rolls are just slightly affected by imposed changes of electric current.

Next, we compare measured and numerically obtained vertical profiles of the mean streamwise (in the x-coordinate direction) velocity component in the central vertical plane (y = 0 m) at characteristic horizontal locations: $x = 0.04, 0.06, 0.08, 0.1$ m, as illustrated in Fig. 5.6. To make a direct comparison between measurements and numerical simulations, we also perform spatial averaging of simulations data in a form of the cylindrical shape (mimicking UDV beam) with typical radius of $r_{av} = 4 \times 10^{-3}$ m and the height $h_{av} = 0.5 \times 10^{-3}$ m.

The comparison between velocity profiles for various strengths of the imposed electric currents is shown in Fig. 5.7. The profiles exhibit typical behavior of a spreading jet with a characteristic peak diminishing with the distance from the nozzle. For the neutral case (I = 0 A), a good agreement is obtained at all locations, Fig. 5.7(a). With the magnetic field activation, the jet angle changes because of the Lorentz force effect. This results in a characteristic jet peak increase in magnitude, with its location closer to the meniscus, and stronger penetration within the mold, Fig. 5.7(b-d). Similar behavior of the flow was previously also observed in experimental studies of [32]. An overall good agreement is obtained at practically all considered locations. Some differences in

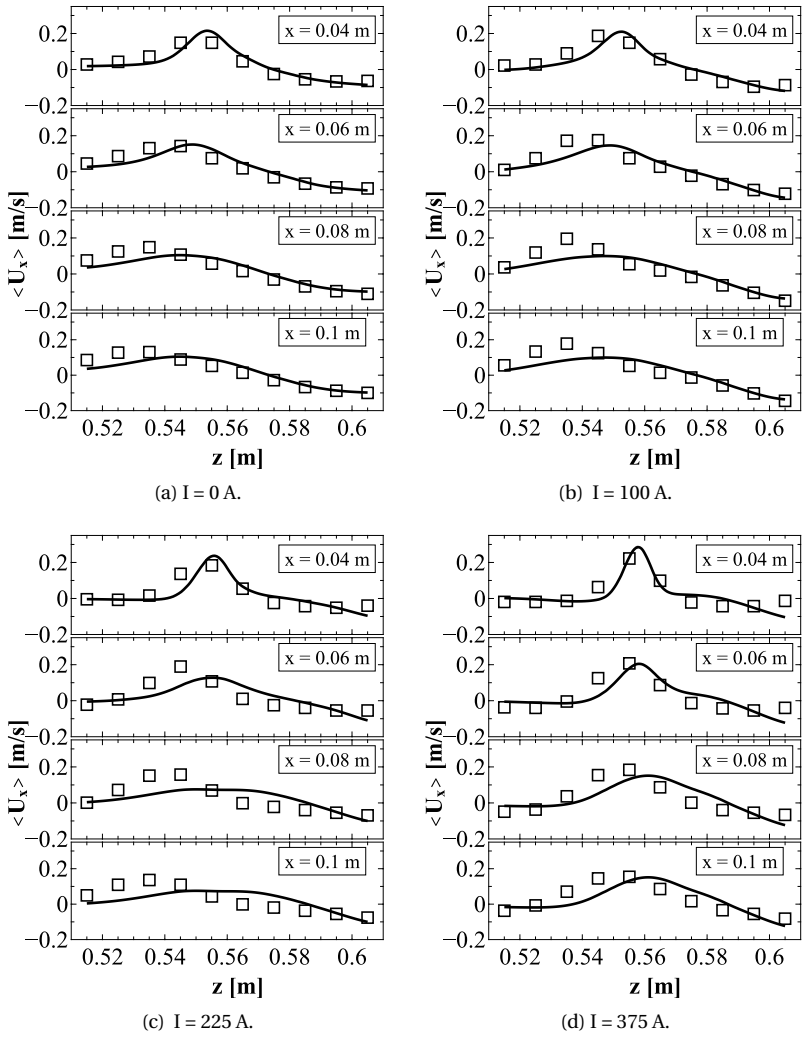

(a) I = 0 A.

(b) I = 100 A.

(c) I = 225 A.

(d) I = 375 A.

Figure 5.7: The profiles of the time- and spatially-averaged horizontal (x-direction) velocity component at characteristic locations indicated in Fig. 5.6 in the range $0 \leq I \leq 375$ A and fixed $C_d = 0$. The following indication is used: (——) - the present numerical study, (□) - the experimental results.

the proximity of the meniscus at x = 0.04, 0.06 and 0.08 m locations are visible for the strongest applied current of $I = 375$ A, Fig. 5.7(d). This can be possibly explained by the formation of the oxide layer at the meniscus in the experiment. The oxide layer can potentially impact the flow distribution acting as a "floating wall". However, this assumption requires further investigation which can be conducted as a continuation of this work. Note that all results presented here are for the intermediate numerical mesh

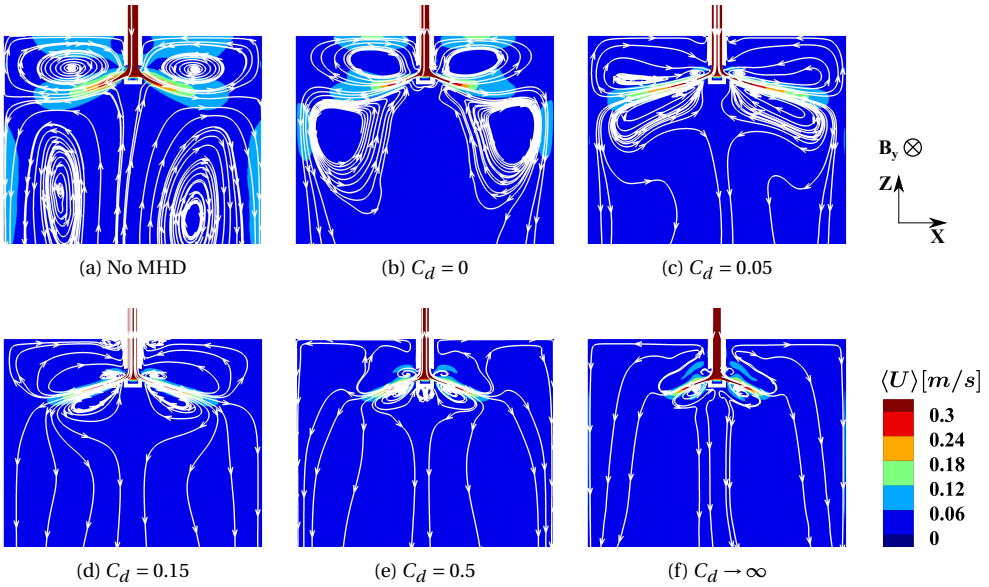

(a) No MHD (b) $C_d = 0$ (c) $C_d = 0.05$

(d) $C_d = 0.15$ (e) $C_d = 0.5$ (f) $C_d \to \infty$

Figure 5.8: The superimposed contours of the long-term time-averaged velocity magnitude and streamlines (white lines) in the central vertical ($y = 0$ m) cross-section (upper half of the mold) for the range of C_d parameter and the specific EMBr strength of $I = 225$ A.

since it proved to be adequate, as shown in the grid dependency analysis in Appendix B.

5.4.2. THE INFLUENCE OF THE WALL CONDUCTIVITY ON THE FLOW STRUCTURE

To study the effects of the finite electrical conductivity of the Hartmann walls on flow and turbulence, we perform a series of numerical simulations from group II (Table. 5.1), where we vary the wall conductance ratio with a fixed imposed electric current of $I = 225$ A. This intermediate current intensity is selected since it proved enough to impose some significant effects on the flow and turbulence for the electrically insulated walls. The long-term time-averaging is performed for 100 s, which proved to be sufficient to get reliable convergence of the flow statistics. This period equals to approximately 1 week of real-time using 96 cores of 2.6 GHz Intel Xeon E5-2697A v4.

The mean velocity fields in the central vertical plane for different values of the wall conductance parameter are shown in Fig. 5.8. To make easier comparisons between different cases, we also plot results of the neutral case (Ha=0), Fig. 5.8(a), as well as the case with electrically insulated walls ($C_d = 0$), Fig. 5.8(b) that are already discussed above. It is striking that even a relatively small wall conductance parameter ($C_d = 0.05$) leads to a significant flow reorganization, as shown in Fig. 5.8(c). The upper and lower rolls are significantly reduced in the vertical direction. The centers of the upper rolls are shifted

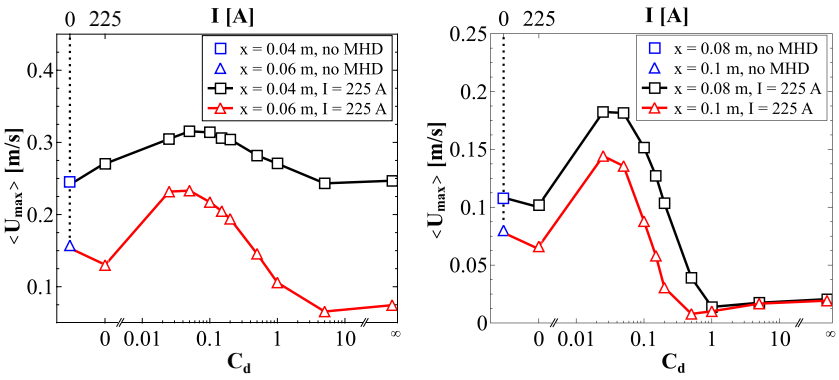

Figure 5.9: Dependency of the maximum magnitude of the mean velocity in the vertical ($y = 0$ m) cross-section with the horizontal coordinates of (a) $x = 0.04$ m and $x = 0.06$ m and (b) $x = 0.08$ m and $x = 0.1$ m on the wall conductivity ratio parameter C_d at the specific EMBr strength of $I = 225$ A. The relative position of the cross-sections is indicated in Fig. 5.6.

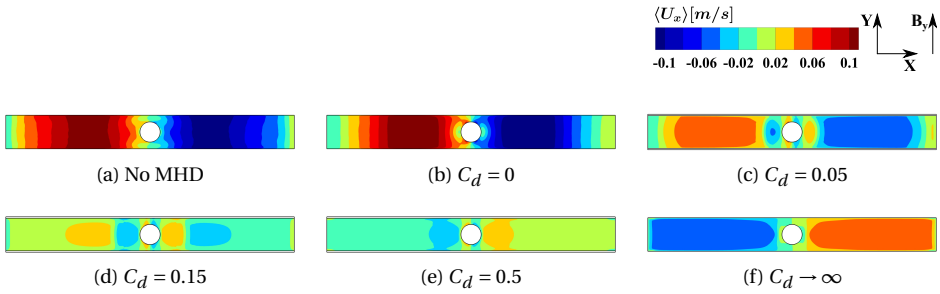

Figure 5.10: The contours of the time-averaged horizontal velocity at the meniscus for the range of C_d parameters and the specific EMBr strength of $I = 225$ A.

away from the SEN, while the situation is opposite for the lower rolls. The penetrative depth of the incoming angular jet also increased. With further increase of the $C_d = 0.15$, much weaker upper and lower rolls are generated, Fig. 5.8(d). At the same time, the penetrative depth of the angular incoming jets also weakens. This reduction of the penetrative depth is even more clear for $C_d = 0.5$ case, while the incoming jet angle stays unchanged. Finally, for the fully conducting Hartmann walls, the upper rolls can not be observed anymore, and the penetrative depth of the incoming jet is reduced further, Fig. 5.8(e).

To provide a more detailed way of comparing the observed changes of the flow, we extract the maximum of the mean velocity magnitude in the central vertical plane ($y = 0$ m)

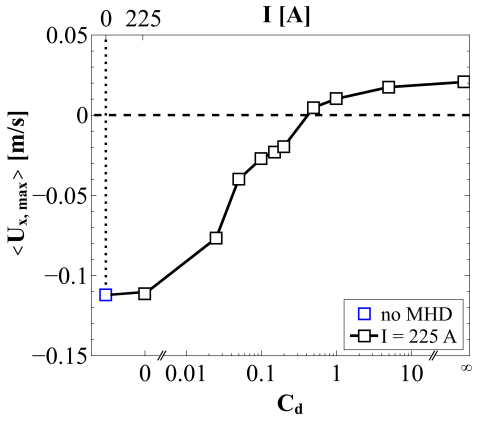

Figure 5.11: Dependency of the meniscus maximum mean horizontal (x) velocity on the wall conductivity ratio C_d, at the specific EMBr strength of I = 225 A. The relative position of the cross-sections is indicated in Fig. 5.6.

along the selected vertical profiles at fixed values of x=0.04, 0.06, 0.08 and 0.1 m, respectively, as illustrated in Fig. 5.9. We focus on the effects of the wall conducting ratio (C_d) for a fixed value of applied current I = 225 A) and show obtained results in Fig. 5.9. For all four locations, we observe a distinct non-linear behavior. For the first location (x=0.04 m), the initial value of the neutral case initially increases until reaching a peak value (at $C_d = 0.1$), followed initially by a gradual decrease before reaching a final value (note that there is a slight increase as $C_d \to \infty$). The remaining three locations (x=0.06, 0.08, and 0.1 m) - all show qualitatively similar behavior, starting with an initial suppression of the maximum of the velocity magnitude immediately upon activation of the magnetic field for the electrically insulated case ($C_d = 0$). All distributions are reaching the local peak in the $0.01 \leq C_d \leq 0.1$ interval, followed by initially very rapid decay (up to $C_d = 1$). After that value, a gradual mild increase is observed with a further increase of C_d. The slopes of the $\langle U_{max} \rangle$ versus C_d curves are showing the largest gradients at distances farther away from the SEN, i.e. at $x = 0.08$ and 0.1 m The observed non-monotonic behavior of the local maxima of the velocity magnitude can be explained in terms of the double rolls reorganization. and the corresponding stretching of the incoming jets. Also, this behavior should be included in the analysis of optimization of the incoming jet spreading, since too strong jets can distort the solidifying regions along the vertical walls. To achieve a stable double roll flow structure and significantly reduced penetrative strength of the incoming jets, one has to keep the wall conductance ratio parameter close to unity.

Another important flow region for continuous casting is the meniscus zone. Here, strong upper rolls can break the upper slag layer at the top surface and cause unwanted entrainment of impurities towards the rest of the mold. Because of its importance, we analyze next the effects of the wall conductivities on the flow at the meniscus, Fig. 5.10. Here, we plot the contours of the horizontal mean velocity $\langle U_x \rangle$ to capture potential

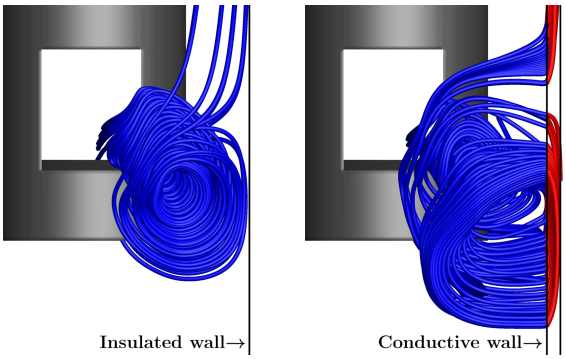

(a) $C_d = 0$ (b) $C_d = 0.15$

Figure 5.12: Visualization of the three-dimensional time-averaged electric current density streamlines in the vicinity of the bottom right corner of the SEN port for the electrically insulated ($C_d = 0$) (a) and Hartmann walls with finite conductivity ($C_d = 0.15$) (b). Note that color indicates distribution within the flow region (blue) or solid wall (red).

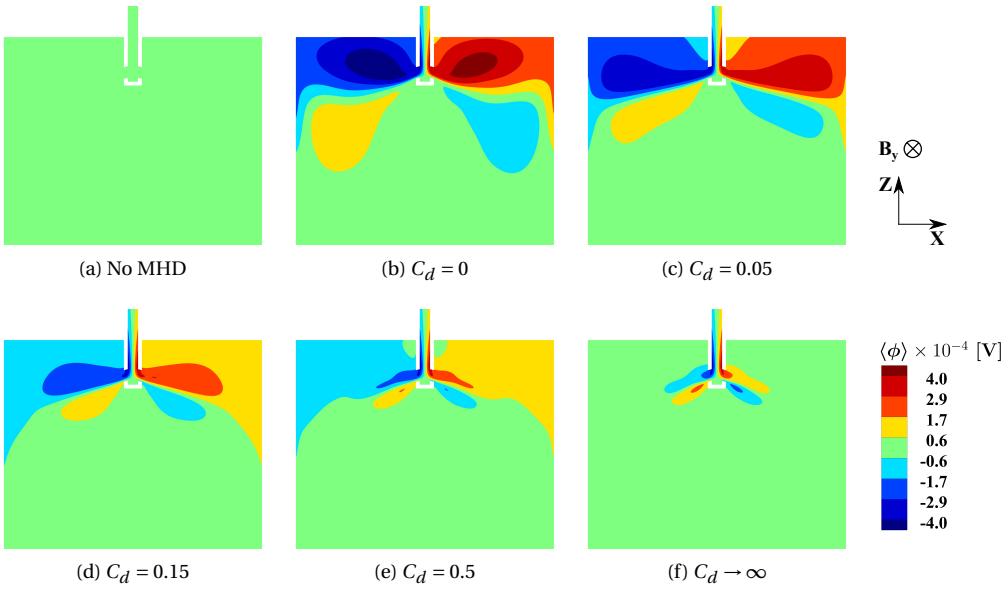

(a) No MHD (b) $C_d = 0$ (c) $C_d = 0.05$

(d) $C_d = 0.15$ (e) $C_d = 0.5$ (f) $C_d \to \infty$

Figure 5.13: The contours of the time-averaged electric potential in the central vertical ($y = 0$ m) cross-section (upper half of the mold) for the range of C_d parameters and fixed EMBr strength of $I = 225$ A.

changes in the flow direction caused by the various wall conductivities. For the non-MHD case, the flow at the meniscus is directed towards the SEN, Fig. 5.10(a). By activating the magnetic field and increasing the wall conductivity the horizontal velocity grad-

ually weakens (Figs. 5.10(b)-(d)), till a critical value of $C_d = 0.5$ is achieved, causing the flow reversal, Fig. 5.10(e). Further increase in C_d produces even stronger reversed flow at the meniscus, Fig. 5.10(f). To provide a more quantitative insight into the strength of the flow at the top surface, we extract the maximum values of the horizontal velocity for various wall conductivities, as shown in Fig. 5.11. It can be seen that very similar values are obtained for the non-MHD and MHD with $C_d = 0$. Further increase of the C_d results in a rapid suppression, with an almost non-moving top surface for the $C_d \approx 0.5$. It can be concluded that the most efficient suppression of the horizontal velocity at the meniscus is obtained in the $0.2 \leq C_d \leq 1$ range, which is useful information for a future design on the continuous casting set-ups.

One should note the main difference in the MHD interaction mechanism between simulations from the above-mentioned groups I and II. For the cases belonging to group I, the resulting Lorentz force distribution is directly affected by strength of the imposed EMBr (i.e. strength of the magnetic field). In contrast to this, for the cases belonging to group II, the resulting Lorentz force is additionally affected by rearrangement of the current density streamlines caused by the finite electrical conductivity of the walls. Now, instead of having fully closed loops of the electric current density streamlines within the fluid domain (for the electrically insulated walls), the electric current also penetrates solid walls, as shown in Fig. 5.12. With higher wall conductivity, the more current density enters the solid region, and current streamlines now loop over both flow and wall domains. This reorganization of the electric current density changes the local Lorentz force distribution, and finally, the velocity field.

To provide additional insights into underlying MHD variables, contours of the mean electric potential in the central vertical plane are shown in Fig. 5.13. Starting from the fully electrically insulated case ($C_d = 0$), it can be seen that local maxima and minima coincide with the locations of the flow loops, Fig. 5.13(b). By increasing C_d, these distinct regions get reduced in size, Fig. 5.8(c)-(f). This behavior is expected since the source of electric potential is the cross product of the magnetic field and local velocity, and distributions of electrical potential closely follow the above-analyzed velocity fields shown in Fig. 5.8. Previous studies indicate that the flow in the mold can be influenced by several control mechanisms, such as argon bubbles injections [34], different strength of the magnetic field [20], [35], [36], and the position of the stopper-rod [37]. The mechanism presented in this work, which consists in using various C_d, differs qualitatively from the mechanisms previously reported in the literature and can be potentially used to obtain a necessary flow structure.

Previous studies indicate that the flow in the mold can be influenced by several control mechanisms, such as argon bubbles injections [34], different strength of the magnetic field [20], [35], [36], and the position of the stopper-rod [37]. The mechanism presented in this work, which consists in using various C_d, differs qualitatively from the mechanisms previously reported in the literature and can be potentially used to obtain a necessary flow structure.

5.4.3. THE INFLUENCE OF THE WALL CONDUCTIVITY ON THE TURBULENCE AND INSTANTANEOUS COHERENT STRUCTURES

Next, we move to analyze in detail the effects of the wall conductance also on the resolved turbulence. The contours of the long-term time-averaged resolved turbulent kinetic energy (TKE) are shown in Fig. 5.14. It can be seen that the predominantly turbulent regions are generated in the bifurcating jet regions for all considered wall conductivities. In addition, for the non-MHD case, the TKE is also high inside the port where the remaining incoming flow after bifurcations impinges on the bottom part. Compared to the neutral no-MHD case, Fig. 5.14(a), activation of the magnetic field causes an extension of the turbulence dominated regions towards the sidewalls and in the proximity of the top surface, while the strong suppression is observed inside the SEN, Fig. 5.14(b). Activation of the finite wall conductance, even with a relatively low value of $C_d = 0.05$, significantly alters this initial distribution and a significant reduction of turbulent regions can be observed, Fig. 5.14(c). Further increase of the wall conductance (i.e. $0.15 \leq C_d \rightarrow \infty$) produces just marginal effects on the TKE distribution, indicating that a saturation point of turbulence reorganization and suppression is achieved, as seen in Figs. 5.14(d-f).

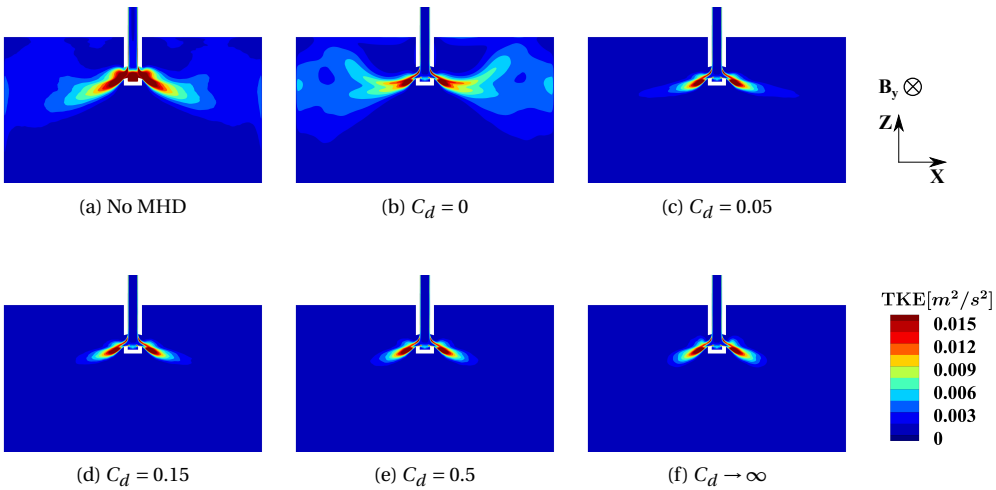

(a) No MHD (b) $C_d = 0$ (c) $C_d = 0.05$

(d) $C_d = 0.15$ (e) $C_d = 0.5$ (f) $C_d \rightarrow \infty$

Figure 5.14: The contours of the long-term time-averaged resolved turbulent kinetic energy (TKE) in the central vertical ($y = 0$ m) cross-section (upper half of the mold) for the range of C_d parameters and fixed EMBr strength of $I = 225$ A.

We close our analysis by finally providing some detailed insights into instantaneous flow and turbulence behavior for different wall conductivities. To represent qualitatively the instantaneous three-dimensional flow structures, we adopt the Q-criterion (i.e. the second-invariant of the velocity gradient tensor), as shown in Fig. 5.15. The non-MHD case exhibits the most dense patterns, indicating a strong interaction between the bifur-

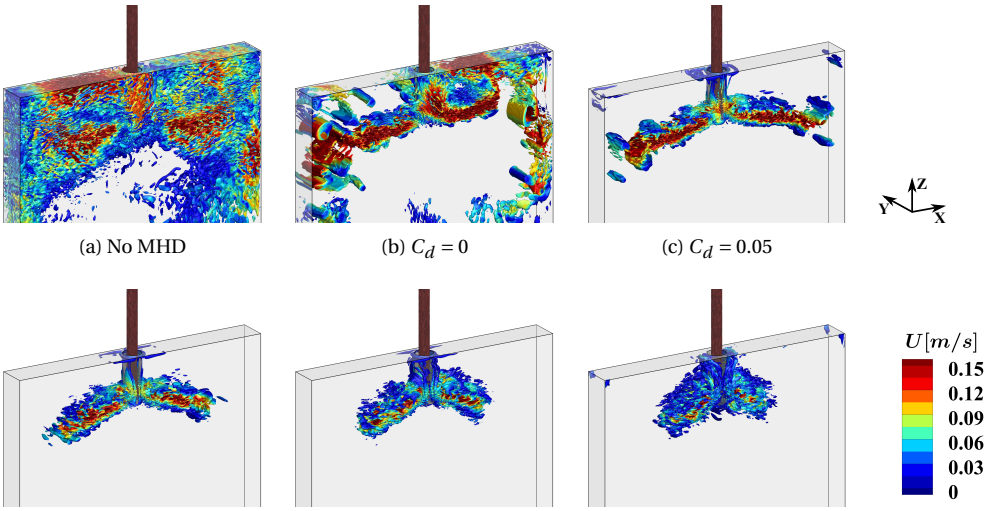

(a) No MHD (b) $C_d = 0$ (c) $C_d = 0.05$

(d) $C_d = 0.15$ (e) $C_d = 0.5$ (f) $C_d \to \infty$

Figure 5.15: The isosurfaces of the second-invariant of the velocity gradient tensor (Q-criterion, Q = 20 s^{-2}) colored by instantaneous velocity magnitude for the range of C_d parameters and fixed EMBr strength of I = 225 A.

cating jets and the free surface regions, Fig. 5.15(a). Activation of the EMBr with $C_d = 0$ generates less populated coherent structure regions with distinct asymmetrical distribution of the bifurcating jets, Fig. 5.15(b). Note that size of coherent structures in the bifurcating jets increases in comparison with the neutral case. In contrast to the fully electrically insulated walls ($C_d = 0$) case, the embedding of electrically conducting walls with $C_d = 0.05$ almost eliminates the long cylindrical-shaped vortices, while remaining coherent structures are mainly concentrated in the bifurcating jets, Fig. 5.15(c). With further increase of C_d, the coherent structures are suppressed and clustered in the horizontally reduced bifurcating jet regions, Fig. 5.15(d-f).

To provide information on the temporal behavior of the bifurcating jets for different values of the wall conductivities, we analyze the time-series of the velocity magnitude at a particular monitoring point (similar to [38, 39]): (i) the 'jet' probe located in the jet proximity with the following coordinates $p_j(0.1, 0, 0.54)$ m, and (ii) the 'meniscus' probe located in the proximity of the top surface with the following coordinates $p_m(0.1, 0, 0.605)$ m, as indicated in Fig. 5.16. The selected monitoring locations are placed in flow regions that are the most sensitive to the flow oscillations.

The time evolutions (over a time interval of 70 s) of the velocity magnitude at characteristic monitoring points, for various values of C_d, are shown in Fig. 5.17. The presented signals illustrate the large-scale vertical (along the z-direction) oscillations of jets emanating from the SEN. It can be seen that both the magnitude and the frequency of pre-

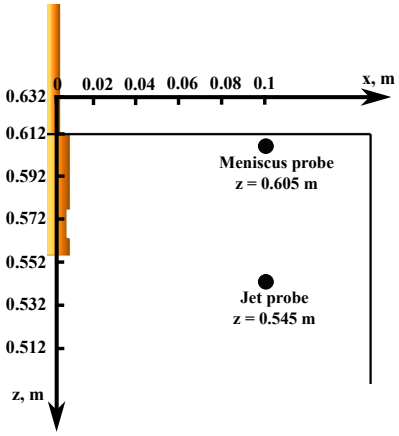

Figure 5.16: The locations of selected monitoring points (probes) in the jet and close to meniscus regions - both in the central vertical ($y = 0$ m) cross-section.

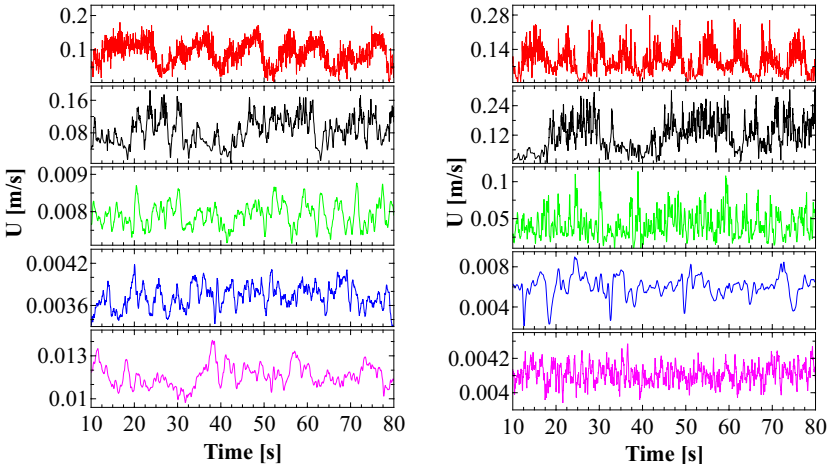

(a) The meniscus probe.

(b) The jet probe.

Figure 5.17: Time series of velocity magnitude for the various C_d parameters and fixed EMBr strength of $I = 225$ A in two monitoring points (as indicated in Fig. 5.16): (a) the meniscus probe; (b) the jet probe. The following lines are used: (—) - no MHD ($I = 0$ A) case; (—) - $I = 225$ A, $C_d = 0$; (—) - $I = 225$ A, $C_d = 0.15$; (—) - $I = 225$ A, $C_d = 0.5$; (—) - $I = 225$ A, $C_d \to \infty$.

sented signals are significantly modified by changing C_d. We calculate the power spectral density (PSD) of these signals by performing a discrete Fourier transformation, and results are shown in Fig. 5.18. Note that to get a better overview of distributions, each spectrum after the non-MHD case is shifted relative to the previous one with a factor of 1/10. For both the sub-meniscus and jet probes, we also indicate characteristic -5/3

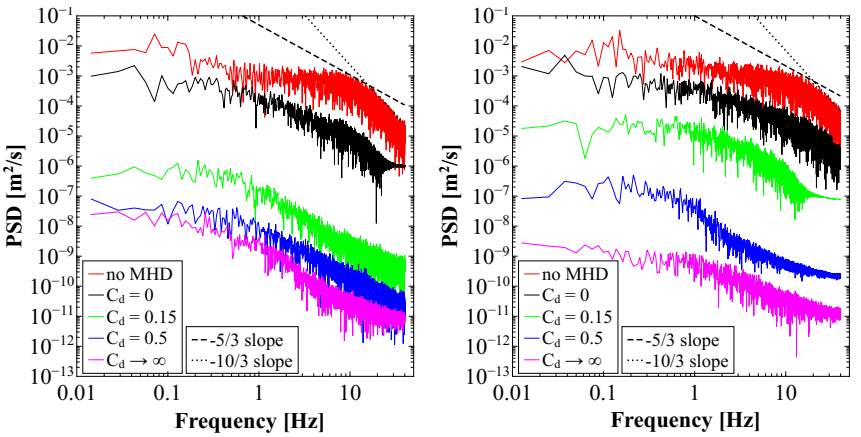

Figure 5.18: Dependency of the power spectral density (PSD) on the frequency at (a) the meniscus probe and (b) the jet probe (locations are shown in Fig. 5.16) for the range of C_d parameters and fixed EMBr strength of $I = 225$ A.

Kolmogorov (black dashed lines) and -10/3 viscous dissipation (black dot lines) slopes. It can be seen that both slopes are followed at both monitoring locations for the neutral non-MHD case, Figs. 5.17(a) and (b). For the sub-meniscus probe, activation of the EMBr with $C_d = 0$ introduces a significant extension of -5/3 slope (inertial) region (i.e. it starts earlier at significantly lower frequencies, $f \approx 1$ Hz), while -10/3 viscous dissipation region is significantly reduced, Figs. 5.18(a). With a further increase of C_d, the -10/3 slope can not be observed anymore while the -5/3 slope (inertial cascade range) still extends over a significant range of frequencies (i.e. $0.2 \leq f \leq 10$ Hz). The PSD at the jet probe location for the non-MHD case also exhibits both -5/3 and -10/3 slopes, Fig. 5.18(b). However, in contrast to the sub-meniscus probe, here the -10/3 slope still can be observed for up to $C_d = 0.5$. Both the inertial and dissipation range are shifted to the lower frequencies with an increase of the wall conductivity ratio, similarly to the sub-meniscus location.

To obtain and compare distinct frequencies of the flow, we extract this information from the above-presented PSD plots and collect them in Table.5.2. For the sub-meniscus probe, a dominant frequency of $f_1 = 0.07$ Hz is observed for the non-MHD case. With EMBr activation, this dominant frequency shifts to $f_1 = 0.042$ Hz. These relatively low frequencies indicate the presence of the extremely long-time preserving unsteady flow behavior, which implies that special care should be taken for a proper collection of the flow first- and second-moments. For $C_d = 0.15$, the most dominant frequency is significantly shifted to $f_1 = 0.21$ Hz, followed with appearance of secondary frequencies at $f_2 = 0.12$ Hz and $f_3 = 0.25$ Hz, respectively. Finally, for $C_d = 0.5$ and $C_d \rightarrow \infty$ cases, the

Table 5.2: List of dominant and secondary frequencies based on the power spectral density at the meniscus probe and the jet probe. The position of the probes is shown in Fig. 5.16.

C_d, Hartmann walls	Meniscus probe, frequency, Hz	Jet probe, frequency, Hz
no MHD	$f_1 = 0.07$	$f_1 = 0.15$
0	$f_1 = 0.042$	$f_1 = 0.035$
0.15	$f_1 = 0.21$ $f_2 = 0.12$ $f_3 = 0.25$	$f_1 = 0.17$ $f_2 = 0.61$ $f_3 = 1.2$
0.5	$f_1 = 0.12$ $f_2 = 0.087$ $f_3 = 0.18$	$f_1 = 0.21$ $f_2 = 0.16$ $f_3 = 0.11$
∞	$f_1 = 0.03$ $f_2 = 0.057$	$f_1 = 0.06$ $f_2 = 0.087$

dominant frequencies are shifted back to $f_1 = 0.12$ Hz and $f_1 = 0.03$ Hz, respectively. For the jet probe, the imposing the EMBr with $C_d = 0$ again produces a reduction of the dominant frequency compared to the neutral non-MHD case, i.e. from $f_1 = 0.15$ Hz to $f_1 = 0.035$ Hz. With further increase of $C_d = 0.15$ and $C_d = 0.5$, multiple secondary frequencies (f_2 and f_3) are also observed. Finally, for $C_d \to \infty$, the most dominant frequency is shifted back to $f_1 = 0.06$ Hz. To conclude, the jet probe indicates the existence of the long-term low-frequency flow oscillations for the non-MHD and fully electrically insulated MHD case ($C_d = 0$). Activation of the finite wall conductance removes these long-term fluctuations ($C_d = 0.15$ and 0.5). However, application of the perfectly conducting walls ($C_d \to \infty$) promotes again a return of long-term low-frequency flow oscillations.

5.5. SUMMARY AND CONCLUSION

We have presented a comprehensive numerical study on the effects of the electric wall conductivity on behavior of a turbulent electrically conducting liquid alloy flow subjected to an external magnetic field - mimicking the experimental setup of the Mini-LIMMCAST casting mold. We have applied an advanced in-house developed conjugate MHD extended Navier-Stokes solver based on open-source OpenFOAM code. The solver is based on the inductionless assumption of the generated magnetic field (i.e. one-way coupling between the momentum and imposed magnetic field) in a combination with

the Large-Eddy Simulation approach employing the dynamic subgrid closure for unresolved turbulent stresses. We have performed a series of numerical simulations that include the neutral (non-MHD) and MHD cases with various imposed EMBr (latter with the fully electrically insulating walls) and compared obtained results with the experimental data. A good agreement between simulations and experiments of the characteristic horizontal component of the mean velocity profiles at different locations is obtained for both non-MHD and MHD cases for various strengths of the imposed EMBr for fully electrically insulated walls. Next, we considered an extensive range of the wall conductivity ratio parameter ($0.025 \leq C_d < \infty$) and analyzed its effects on the flow and turbulence inside the mold. We have shown that with increasing the wall conductivity ratio of the Hartmann walls a significant reorganization of the initial double-roll flow structure takes place. This flow reorganization was also followed by significant suppression of the flow oscillations. We have observed a non-monotonic behavior of the mean velocity magnitude maximum at all selected profiles in the central vertical plane. This non-monotonic behavior also indicated generation of the enhanced side-jets in the $0.025 \leq C_d < 1$ range, while the strongest mean velocity suppression was obtained for $C_d \approx 1$. In addition, we have demonstrated that the velocity in the proximity of the top surface (i.e. the sub-meniscus region) showed high sensitivity to the presence of the electrically conducting walls. The maximum velocity was obtained in the $0.2 \leq C_d \leq 1$ range, whereas the flow reversal was taking place with a further increase of C_d. The power spectral density analysis of the instantaneous velocity magnitude at two characteristic monitoring locations, placed in the side-jet and the vicinity of the meniscus revealed the existence of flow oscillations with a very low frequency for the neutral (non-MHD) and MHD case with perfectly electrically insulated walls ($C_d = 0$). This low frequency was not observed for the MHD cases with $0.15 \leq C_d \leq 0.5$. However, for the perfectly electrically conducting walls case ($C_d \to \infty$), the long-term low-frequency flow oscillation reappeared. Practical implementation of various C_d can be possible by changing the mold parameters such as the mold width, though high values of the wall conductivity ratio ($C_d > 1$) will be challenging to achieve. The alternative way will be changing the size of the EMBr. The presented results can provide important designing guidelines for the new generation of the laboratory- and real-scale industrial continuous casting setups.

REFERENCES

[1] B. G. Thomas and L. Zhang, *Mathematical modeling of fluid flow in continuous casting,* ISIJ International **41**, 1181 (2001).

[2] P. A. Davidson, *An introduction to magnetohydrodynamics*, Cambridge Texts in Applied Mathematics (Cambridge University Press, 2001).

[3] B. G. Thomas and R. Chaudhary, *State of the art in electromagnetic flow control in continuous casting of steel slabs: Modeling and plant validation,* 6th International Conference on Electromagnetic Processing of Materials EPM (2009).

[4] S. Kenjereš, *On modeling and eddy-resolving simulations of flow, turbulence, mixing and heat transfer of electrically conducting and magnetizing fluids: A review,* International Journal of Heat and Fluid Flow **73**, 270 (2018).

[5] Y. Plevachuk, V. Sklyarchuk, S. Eckert, G. Gerbeth, and R. Novakovic, *Thermophysical properties of the liquid Ga–In–Sn eutectic alloy,* Journal of Chemical & Engineering Data **59**, 757 (2014).

[6] R. Chaudhary, B. Thomas, and S. Vanka, *Effect of electromagnetic ruler braking (EMBr) on transient turbulent flow in continuous slab casting using large eddy simulations,* Metallurgical and Materials Transactions B **43**, 532 (2012).

[7] F. Li, E. Wang, M. Feng, and Z. Li, *Simulation research of flow field in continuous casting mold with vertical electromagnetic brake,* ISIJ International **55**, 814 (2015).

[8] B. Righolt, S. Kenjereš, R. Kalter, M. Tummers, and C. Kleijn, *Dynamics of an oscillating turbulent jet in a confined cavity,* Physics of Fluids **27**, 095107 (2015).

[9] L. Zhang, J. Aoki, and B. G. Thomas, *Inclusion removal by bubble flotation in a continuous casting mold,* Metallurgical and Materials Transactions B **37**, 361 (2006).

[10] S. Sarkar, V. Singh, S. K. Ajmani, R. K. Singh, and E. Z. Chacko, *Effect of argon injection in meniscus flow and turbulence intensity distribution in continuous slab casting mold under the influence of double ruler magnetic field,* ISIJ International (2017).

[11] D. Schurmann, B. Willers, G. Hackl, Y. Tang, and S. Eckert, *Experimental study of the mold flow induced by a swirling flow nozzle and electromagnetic stirring for continuous casting of round blooms,* Metallurgical and Materials Transactions B **50**, 716 (2019).

[12] K. Timmel, S. Eckert, and G. Gerbeth, *Experimental investigation of the flow in a continuous-casting mold under the influence of a transverse, direct current magnetic field,* Metallurgical and Materials Transactions B **42**, 68 (2011).

[13] T. Wondrak, S. Eckert, G. Gerbeth, K. Klotsche, F. Stefani, K. Timmel, A. J. Peyton, N. Terzija, and W. Yin, *Combined electromagnetic tomography for determining two-phase flow characteristics in the submerged entry nozzle and in the mold of a continuous casting model,* Metallurgical and Materials Transactions B **42**, 1201 (2011).

[14] I. Muttakin and M. Soleimani, *Magnetic induction tomography spectroscopy for structural and functional characterization in metallic materials,* Materials **13**, 2639 (2020).

[15] S. Graebe, G. Goodwin, and G. Elsley, *Control design and implementation in continuous steel casting,* IEEE Control Systems Magazine **15**, 64 (1995).

[16] S. Abouelazayem, I. Glavinić, T. Wondrak, and J. Hlava, *Flow control based on feature extraction in continuous casting process,* Sensors **20**, 6880 (2020).

[17] X. Miao, K. Timmel, D. Lucas, Z. Ren, S. Eckert, and G. Gerbeth, *Effect of an electromagnetic brake on the turbulent melt flow in a continuous-casting mold,* Metallurgical and Materials Transactions B **43**, 954 (2012).

[18] Z. Liu, A. Vakhrushev, M. Wu, E. Karimi-Sibaki, A. Kharicha, A. Ludwig, and B. Li, *Effect of an electrically-conducting wall on transient magnetohydrodynamic flow in a continuous-casting mold with an electromagnetic brake,* Metals **8**, 609 (2018).

[19] A. Vakhrushev, A. Kharicha, Z. Liu, M. Wu, A. Ludwig, G. Nitzl, Y. Tang, G. Hackl, and J. Watzinger, *Electric current distribution during electromagnetic braking in continuous casting,* Metallurgical and Materials Transactions B **51**, 2811 (2020).

[20] A. Vakhrushev, A. Kharicha, E. Karimi-Sibaki, M. Wu, A. Ludwig, G. Nitzl, Y. Tang, G. Hackl, J. Watzinger, and S. Eckert, *Generation of reverse meniscus flow by applying an electromagnetic brake,* Metallurgical and Materials Transactions B **52**, 3193 (2021).

[21] K. Zhang, M. Weeks, and P. Roberts, *Effect of electrically conducting walls on rotating magnetoconvection,* Physics of Fluids **16**, 2023 (2004).

[22] S. Smolentsev, R. Moreau, L. Bühler, and C. Mistrangelo, *MHD thermofluid issues of liquid-metal blankets: phenomena and advances,* Fusion Engineering and Design **85**, 1196 (2010).

[23] A. Blishchik, M. van der Lans, and S. Kenjereš, *An extensive numerical benchmark of the various magnetohydrodynamic flows,* International Journal of Heat and Fluid Flow **90**, 108800 (2021).

[24] A. Blishchik and S. Kenjereš, *Observation of a novel flow regime caused by finite electric wall conductance in an initially turbulent magnetohydrodynamic duct flow,* Physical Review E **104**, L013101 (2021).

[25] C. Mistrangelo and L. Bühler, *Development of a numerical tool to simulate magnetohydrodynamic interactions of liquid metals with strong applied magnetic fields,* Fusion Science and Technology **60**, 798 (2011).

[26] D. Krasnov, O. Zikanov, J. Schumacher, and T. Boeck, *Magnetohydrodynamic turbulence in a channel with spanwise magnetic field,* Physics of Fluids **20**, 095105 (2008).

[27] D. K. Lilly, *A proposed modification of the Germano subgrid-scale closure method,* Physics of Fluids A: Fluid Dynamics **4**, 633 (1992).

[28] M.-J. Ni, R. Munipalli, N. B. Morley, P. Huang, and M. A. Abdou, *A current density conservative scheme for incompressible MHD flows at a low magnetic Reynolds number. Part I: On a rectangular collocated grid system,* Journal of Computational Physics **227**, 174 (2007).

[29] N. Weber, P. Beckstein, V. Galindo, M. Starace, and T. Weier, *Electro-vortex flow simulation using coupled meshes,* Computers & Fluids **168**, 101 (2018).

[30] H. G. Weller, G. Tabor, H. Jasak, and C. Fureby, *A tensorial approach to computational continuum mechanics using object-oriented techniques,* Computers in Physics **12**, 620 (1998).

[31] R. I. Issa, A. Gosman, and A. Watkins, *The computation of compressible and incompressible recirculating flows by a non-iterative implicit scheme,* Journal of Computational Physics **62**, 66 (1986).

[32] D. Schurmann, I. Glavinić, B. Willers, K. Timmel, and S. Eckert, *Impact of the electromagnetic brake position on the flow structure in a slab continuous casting mold: An experimental parameter study,* Metallurgical and Materials Transactions B **51**, 61 (2020).

[33] D. Spalding, *A single formula for the law of the wall,* Journal of Applied Mechanics **28**, 455 (1961).

[34] P. L. Santos, J. J. M. Peixoto, C. A. da Silva, I. A. da Silva, and C. M. Galinari, *Bubble behavior in the slab continuous casting mold: Physical and mathematical model,* Journal of Materials Research and Technology **9**, 4717 (2020).

[35] D. Schurmann, I. Glavinić, B. Willers, K. Timmel, and S. Eckert, *Impact of the electromagnetic brake position on the flow structure in a slab continuous casting mold: An experimental parameter study,* Metallurgical and Materials Transactions B (2019).

[36] J. Kubota, N. Kubo, T. Ishii, M. Suzuki, N. Aramaki, and R. Nishimachi, *Steel flow control in continuous slab caster mold by traveling magnetic field,* NKK Technical Review **85**, 1 (2001).

[37] R. Chaudhary, G.-G. Lee, B. G. Thomas, S.-M. Cho, S.-H. Kim, and O.-D. Kwon, *Effect of stopper-rod misalignment on fluid flow in continuous casting of steel,* Metallurgical and Materials Transactions B **42**, 300 (2011).

[38] S. Kenjereš, S. Ten Cate, and C. Voesenek, *Vortical structures and turbulent bursts behind magnetic obstacles in transitional flow regimes,* International Journal of Heat and Fluid Flow **32**, 510 (2011).

[39] S. Kenjereš, *Energy spectra and turbulence generation in the wake of magnetic obstacles,* Physics of Fluids **24**, 115111 (2012).

6

CONCLUSION

6.1. CONCLUSIONS

The use of electrically conductive fluids, such as liquid metals, is common in various industrial applications. The high electrical conductivity of these fluids give an opportunity to interact with them in a non-invasive way. By imposing an external magnetic field, an additional force on the flow is produced. This interaction can be described using magnetohydrodynamic (MHD) principles, and its application is found to be a key factor to control unstable industrial flows. Given the cost and temperature/storage conditions of liquid metals, numerical simulations are considered to be the preferred method to investigate MHD mechanisms. This dissertation describes the numerical research of different MHD mechanisms in industrial (continuous casting) and simplified flow setups, primarily focusing on MHD turbulence and the influence of electrically conductive surrounding walls.

In Chapter 2, we presented the details of our computational code based on the open-source library OpenFOAM. The development of an accurate and advanced MHD code is a crucial task for the present research since existing commercial codes have limited capabilities (e.g. implementation of new algorithms or models). To simulate such flows, each numerical method and model implemented in our solver was thoroughly validated. The code was developed under the assumption of a high magnetic diffusivity of the liquid metal (low-Re_m formulation), and therefore a Poisson equation for the electric potential was discretized and solved. To conserve current density at cell faces, the Four Steps Projection Method (FSPM) was implemented. FSPM is known to be an accurate and efficient method based on the conservative formulation of the Lorentz force. Validation of FSPM was conducted by simulating classical cases including MHD flow in a duct and a back-step MHD flow. The next part of the benchmark was devoted to multiphase MHD modeling. To simulate the liquid surface of different electrically conductive fluids, we implemented a modified Volume of Fluid method. The impact of the spurious currents was suppressed by the application of a Laplacian filter. Validation was performed by simulating MHD cavity flow and a raising gas bubble in a conductive liquid metal exposed to a magnetic field.

After implementing fundamental magnetohydrodynamic methods, we approached the first research question: How to model the interaction between electrically conductive walls and an electrically conductive flowing fluid? Several concepts to model the interaction between electrically conductive walls and an electrically conductive flowing fluid have been generally discussed. Based on that discussion, we developed and implemented a method which we called conjugate MHD. This method is essentially based on splitting the computational domain into sub-domains: the liquid sub-domain and solid sub-domains. The explicit advantage of the conjugate MHD method is that any geometry with any thickness/conductivity can be modeled, which is not the case for other methods reproducing wall conductivity. Validation of the conjugate MHD method was performed by modeling laminar/turbulent MHD flow in a duct with finite arbitrary electrically conductive walls. Hence, we answered our first research question. To conclude,

we developed, implemented, and validated the advanced numerical MHD code capable to deal with a broad range of magnetohydrodynamic flows. This solver is used in the next chapters.

In Chapter 3, we approached the second research question: How does the presence of electrically conductive walls affect the MHD turbulent flow? To answer this question, we investigated the impact of a wide range of wall conductivity ratios C_d on turbulent MHD flow in a square duct with an external transverse magnetic field. The Reynolds number Re and the Hartmann number Ha were fixed as constants in order to focus entirely on the C_d influence. Our main finding is that as the wall conductivity ratio increases the turbulent flow undergoes a rapid laminarization process until reaching a fully laminar state at $C_d = 0.15$. However, a further increase of C_d does not maintain the laminar state. Instead, we observed the gradual recurrence of turbulence at $C_d \geq 0.25$, and the return to the highly-turbulent state at $C_d = 5$. Remarkably, a further increase of the wall conductivity ratio up to $C_d \to \infty$ results in a higher turbulence level compared even to the neutral case at $Ha = 0$. It is also important to emphasize the difference between the classical MHD damping mechanism and the present novel turbulent-laminar-turbulent transition phenomena. Unlike the classical MHD damping mechanism which affects the turbulence due to the increase of the magnetic field, the novel flow regime is observed at a constant magnetic field strength.

In Chapter 4, we continued with the second research question and further investigated the fundamental properties of the turbulent-laminar-turbulent transition due to the change in the wall conductivity ratio C_d. We found that the flow laminarization is accompanied by the appearance of a patterned turbulence phenomenon. Separate turbulent puffs and spots can be identified in the proximity of walls parallel to the magnetic field. The patterned turbulence phenomenon becomes more pronounced as the wall conductivity ratio approaches the critical value of $C_d = 0.15$. The subsequent turbulence regeneration does not follow the same trend. Turbulence structures start forming closer to the flow core and near the walls perpendicular to the magnetic field. Special attention in this chapter was also devoted to the understanding of the origin of the transition mechanism. It was found that the change of the wall conductivity caused a reduction of the electric potential gradient. In turn, this leads to the reorganization of the current density which is directly linked to the Lorentz force. By analyzing the turbulent kinetic energy budgets, we found that such an alteration of the Lorentz force had a strong impact on the velocity gradient and therefore on the production term. Thus, based on the discussion in Chapter 2 and Chapter 3, we can conclude that the presence of electrically conductive walls significantly affects the turbulent MHD flow and can suppress or promote MHD turbulence.

In Chapter 5, we directly approached the third research question: What is the influence of an electrically conductive shell on the MHD liquid metal flow structure in a continuous casting mold? The flow in the mold was exposed to the electromagnetic brake influence. The shell was mimicked by embedding electrically conductive walls inside

the mold. To validate our results, we used experimental data provided by Helmholtz-Zentrum Dresden Rossendorf. It was found that an increase of the shell conductivity significantly affected the double-roll flow structure, gradually transforming it into a single-roll structure. Remarkably, the subsequent change in velocity values in the jets coming out of the submerged entry nozzle (SEN) occurred non-monotonically. The maximum was reached in the range $0.025 \leq C_d < 0.1$, while the minimum occurred at $C_d \approx 1$. This was directly linked to the rearrangement in the double-roll pattern. At low C_d, squeezed but elongated rolls formed, while at moderate C_d the rolls became smaller. The appearance of strong jets at small C_d can be potentially problematic in terms of the shell structural integrity and should be taken into account. The meniscus area was also found to be influenced by the shell conductivity. In particular, an increase of C_d led to a reverse flow at the meniscus. The minimum meniscus velocity was achieved at $C_d \approx 1$. An analysis of impact of the shell conductivity on the turbulence demonstrated a strong turbulence suppression while increasing C_d. Thus, the strong influence of an electrically conductive shell on the MHD liquid metal flow structure in a continuous casting mold was found.

To conclude, we emphasize two main points. First, it is crucial to account for electrically conductive solid walls and structures in simulations and experiments, to properly account for their presence in a real-life MHD processes. Considering continuous casting, their neglect can lead to incorrect predictions of flow behavior in the critical zones. Second, the introduction of electrically conductive walls in setups potentially opens a wide range of opportunities to control MHD flows. In particular, it can be used to control highly unstable turbulent flows.

6.2. FUTURE OPPORTUNITIES

In this section, we present future research opportunities that can extend the present work.

6.2.1. THE INFLUENCE OF THE CORRELATION R - C_d ON TURBULENT FLOW IN AN ELECTRICALLY CONDUCTIVE DUCT

The patterned turbulence phenomenon in classical turbulent MHD duct flow with fully electrically insulated walls ($C_d = 0$) is known to be sensitive to the ratio $R = Re/Ha$ [1]. This sensitivity can be expressed in the form of a dependency between the flow regime and the R value, Fig. 6.1. There are five flow regimes in total and two of them are associated with the patterned turbulence. Although the limits and ranges presented are clearly approximate, they provide researchers with an estimate of when to expect the transition. In this dissertation, we considered a different setup, namely R was a constant while C_d was varied. Similar to the R-map, the dependency between flow regimes and C_d can be portrayed as a C_d-map, Fig. 6.2. Given that both the R-map and the C_d-map are correlated to each other, several research opportunities can be formulated. First, it is expected that by increasing or decreasing the R value (relative to the present value of

$R = 265$), the C_d-map will undergo significant changes. For example, we think that an increase of R could strongly reduce or even remove the patterned turbulence regimes from the C_d-map. Similarly, a decrease of R could enhance the patterned turbulence regimes. Second, the reverse influence of C_d on the R-map should not be underestimated. By keeping C_d constant and changing the R parameter, a different distribution of regimes could be obtained. Since full-scale CFD simulations of all possible correlations between C_d and R take a lot of time, the careful application of machine learning techniques could help researchers to generally characterise regimes.

6.2.2. THE CUMULATIVE IMPACT OF THE CASTING SPEED, THE SHELL CONDUCTIVITY, AND THE NON-UNIFORM SHELL THICKNESS

An electrically conductive shell is formed in the casting mold due to the cooling processes. In this work, we already described the importance of the electrical conductivity of the shell. However, there are several additional factors and properties that should be taken into account. Proper consideration of these factors could extend the present work and complement the existing knowledge. First, the shell is moved down by support rolls during the casting process. This is an essential operation to transport the solidified shell for further processing. The velocity at which the transportation takes place is called the casting speed u_c. Although the casting speed is relatively small, an influence of the so-called "moving walls" on the flow in the mold is to be expected. Second, while solidifying, the shell maintains a non-uniform thickness. The shell in the proximity of the meniscus is thinner compared to the shell in the proximity of the outlet. This non-uniform thickness will have a direct impact on the wall conductivity ratio C_d. Furthermore, changes in the electrical conductivity of the shell due to temperature differences will also be relevant [2]. Thus, the combined interaction of the moving non-uniform electrically conductive shell could potentially affect the flow in a more complex way, Fig. 6.3.

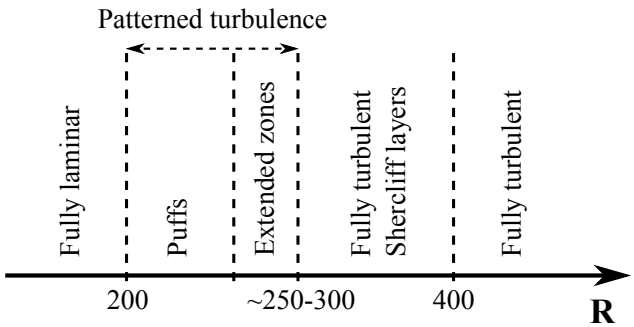

Figure 6.1: Dependency between flow regimes and $R = Re/Ha$ for the electrically insulated duct $C_d = 0$.

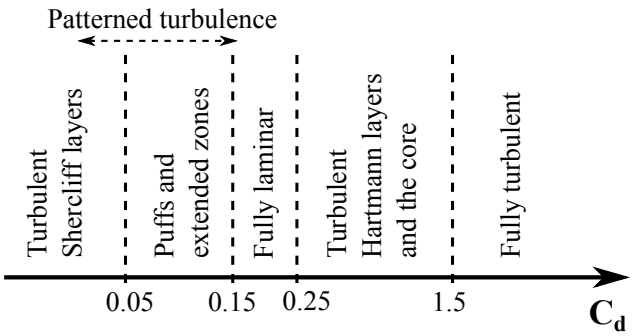

Figure 6.2: Dependency between flow regimes and C_d for the regime at $R = 265$.

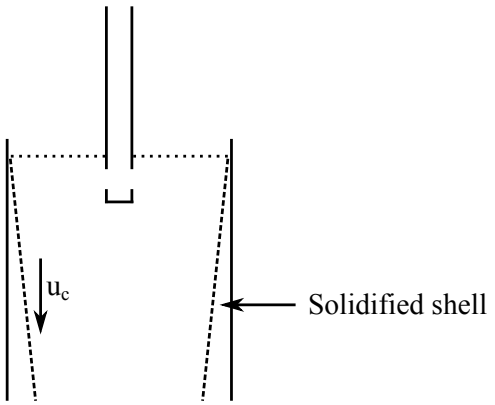

Figure 6.3: Sketch of the solidified shell.

6.2.3. OPTIMISATION OF LIQUID METAL BLANKET DESIGNS

A breeding blanket (BB) system is known to be one of the most challenging parts of a fusion reactor. The BB system stays in a contact with fusion plasma and undergoes extreme thermal loads. In order to keep the BB system stable, heat has to be removed. Liquid metals are widely used in such a case due to their relatively high thermal conductivity. However, given a strong magnetic field in a fusion reactor, magnetohydrodynamic effects also play an important role in addition to thermal effects [3].

The optimization of processes in liquid metal blankets can potentially benefit energy performance and equipment costs. The liquid metal blankets contain various geometrical elements such as ducts, pipes, and bends. Conducting real- or laboratory-scaled experiments aimed at the optimization of such elements is costly, and these experimental facilities are also difficult to operate. Thus, simulations remain the most affordable choice. Considering numerical simulations, special attention should be devoted to the fluid-solid MHD interactions which occur due to the strong magnetic field and arbitrary electrical conductivity of solid parts. A high level of turbulence in a flow of a liquid metal

should be also taken into account. The numerical conjugate MHD solver presented in this dissertation can be used for such a study. Our solver can accurately simulate turbulent MHD flows as well as fluid-solid MHD interactions.

6.2.4. INVESTIGATION OF BATH-ALUMINIUM INTERFACE INSTABILITIES IN A HALL– HÉROULT CELL

The Hall–Héroult process is the main industrial process for smelting aluminum. The process is based on generating Joule heating due to the high resistivity of the bath layer in an anode-cathode system. The efficiency of the system strongly depends on the so-called anode-cathode distance (ACD) which should be as small as possible, Fig. 6.4. However, the possible decrease in the ACD is associated with technological limitations caused by the instabilities at the bath-aluminum interface. These instabilities occur due to a coupled impact of hydrodynamic and magnetohydrodynamic forces. For example, an electric current flowing inside and outside the system creates a strong non-uniform magnetic field which contributes to the Lorentz force. Such a phenomenon is extremely difficult to investigate in an experimental facility. Hence, a multiphase magnetohydrodynamic solver is necessary to study possibilities for lowering ACD in new or existing industrial facilities. The solver presented in this dissertation is capable to solve this type of multiphase MHD flows using the Volume of Fluid framework. Such simulations can be computationally costly but potentially can provide a deeper insight into the flow physics at the interface.

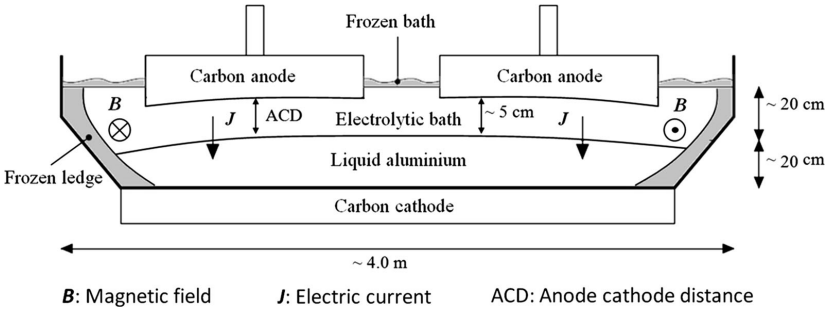

Figure 6.4: Sketch of a Hall– Héroult cell [4].

REFERENCES

[1] O. Zikanov, D. Krasnov, T. Boeck, A. Thess, and M. Rossi, *Laminar-turbulent transition in magnetohydrodynamic duct, pipe, and channel flows,* Applied Mechanics Reviews **66** (2014).

[2] B. Wilthan, W. Schützenhöfer, and G. Pottlacher, *Thermophysical properties of five industrial steels in the solid and liquid phase,* International Journal of Thermophysics **38**, 83 (2017).

[3] C. Mistrangelo, L. Bühler, S. Smolentsev, V. Klüber, I. Maione, and J. Aubert, *MHD flow in liquid metal blankets: Major design issues, MHD guidelines and numerical analysis,* Fusion Engineering and Design **173**, 112795 (2021).

[4] J. Hua, M. Rudshaug, C. Droste, R. Jorgensen, and N.-H. Giskeodegard, *Numerical simulation of multiphase magnetohydrodynamic flow and deformation of electrolyte–metal interface in aluminum electrolysis cells,* Metallurgical and Materials Transactions B **49**, 1246 (2018).

ACKNOWLEDGEMENTS

I would like to thank everyone who supported me during my PhD journey. This period of my life gave me a lot of new skills, interesting experience, and amazing connections. Obviously, four years of work on the PhD project were quite intense and were full of ups and downs. Without my family, friends, and colleagues, it would be definitely impossible to complete this dissertation.

Saša, it is impossible to exactly measure the amount of support you have given me as my main promoter. You were always ready to help me with both work-related and personal matters. I really appreciate that you gave me such an incredible chance to work on a very interesting topic and an opportunity to develop myself further. Special thanks for your help with scientific writing, which was definitely one of the most difficult things for me. **Chris**, I am grateful to you for the career-oriented discussions that we had during our meetings. These discussions significantly expanded my horizons and were very helpful to me. **Daniel and Dirk**, I enjoyed our intensive collaboration and brainstorming. It was very motivating to look at the industrial implementation of our work. **Ivan, Thomas, Shereen, and Imamul**, cooperating with you was one of the best parts of my PhD. I am proud that our liquid metal group was one of the most successful and friendly groups in the TOMOCON project. **Thomas**, my secondment at HZDR was the first time when I had an opportunity to work with real liquid metal and it was super interesting.

Elin, you were a great responsive colleague and one of the best OpenFOAM/CFD experts in our group. Thank you for your help, especially at the beginning of my PhD. **Matheus**, I was very happy when you decided to move into our office because at that moment the number of jokes doubled. It was always good to complain together about the PhD fate. **Doni, Fei, Kevin, Brice, Saikat, Ruipeng**, thank you for being my office mates, I wish all of you the best of luck. **Sid, Manu, Annekatrien, Romana, and Yanyan**, it was always a pleasure to have regular lunches with you and discuss some funny things. **Jorrit**, I appreciate your help with the Dutch translation of my summary. **Lorenz and Caroline**, thank you for hosting our board and video games parties, they were really great. **Andrey**, our political tea talks helped a lot. **Kostadin, Nathalie, Xiaolin, Manas, Minu, Bijoy, Xiaolin, Aron, Vojtech, Jan, Christian, Mike, Ahmed, Rik, Sandra, and Luis**, I am glad that I met you all.

Iana, not every person decides to leave her home and move with her partner to somewhere unknown. And even fewer people are able to become stronger under these difficult circumstances. You managed to do it and meanwhile, you always support me regardless of the problem I have. I am privileged to be your partner.

Мама, Папа, спасибо за всю ту громадную поддержку, которую вы мне оказали.

Та точка моего пути, где я сейчас нахожусь, была бы вряд ли возможна, если бы вы не пожертвовали все свои доступные и недоступные ресурсы на меня. Я это ценю и не забываю.

A

Analysis of the meniscus fluctuations for the Mini-LIMMCAST setup

A

The spatial-temporal contours of the meniscus free surface fluctuations are shown in Fig. A.1. The free surface was modeled by applying the modified Volume of Fluid method. It can be seen that the fluctuations become more intense as the Hartmann number increases. However, even at $Ha = 210$, the amplitude of the fluctuations does not exceed the limit of 4 mm. Therefore, it can be concluded that the replacement of the free surface with the slip wall does not affect the flow in the mold significantly.

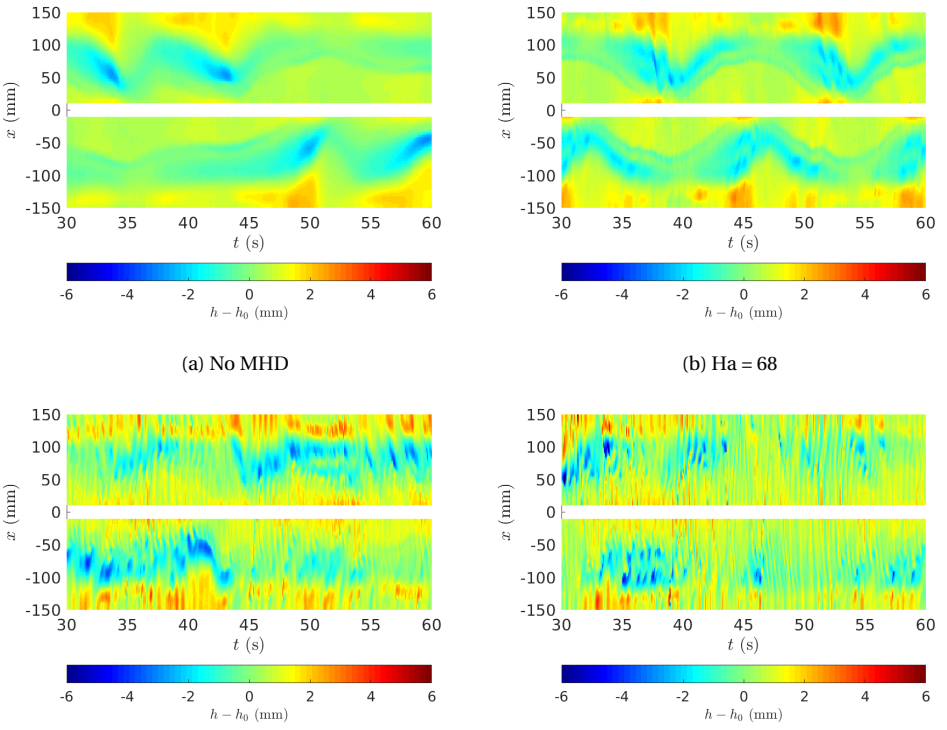

(a) No MHD

(b) Ha = 68

(c) Ha = 142

(d) Ha = 210

Figure A.1: Spatial-temporal plots of the meniscus fluctuations at $Re = 50000$ and at various Ha.

B

MESH INDEPENDENCE FOR THE MINI-LIMMCAST SETUP

B

The investigation of the mesh influence on the obtained solution is shown in Fig. B.1, for the case with the EMBr strength of I = 375 A. Three already mentioned grids have been tested: the coarse mesh $M_{L,coarse}$, the intermediate mesh M_L, and the fine mesh $M_{L,fine}$. As it can be seen, the difference between the M_L and $M_{L,fine}$ is marginal, and therefore the results obtained with the intermediate mesh can be declared as the grid-independent.

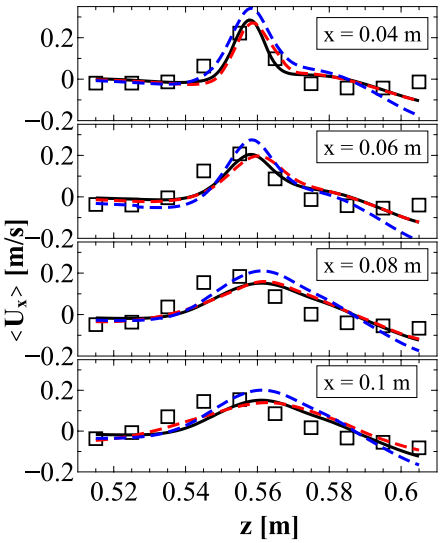

Figure B.1: The profiles of the long-term time- and spatially-averaged horizontal velocity obtained at various grids at I = 375 A and C_d = 0. The following notation is used: (□) - the experimental results; (– –) - the coarse mesh $M_{L,coarse}$; (——) - the main intermediate mesh; M_L (– –) - the fine mesh $M_{L,fine}$.

C

COMPUTATIONAL CODE

The MHD solvers presented in this dissertation are generally open-source and can be used by anyone without any restrictions. However, the computational codes are quite lengthy, and therefore, they are not suitable to be included as a text appendix. Thus, most of the solvers can be accessed online via the following links:
`https://github.com/Kommbinator/MHD_Solvers_OpenFOAM`
`https://github.com/Kommbinator`

C

The conjugate MHD algorithm is based on the standard ChtMultiRegionFoam algorithm [1] and can be described as follows:

1. The equations in the fluid domains are solved. The electric potential equation in the fluid domain is solved using the solid electric potential values from the previous step to calculate the boundary conditions in the fluid domain.

2. The equations in the solid domains are solved. The electric potential equation in the solid domain is solved using the fluid electric potential values from the previous step to calculate the boundary conditions in the solid domain.

3. The electric potential value at the interface is calculated based on the weighted-flux scheme [2].

[1] https://openfoamwiki.net/
[2] N. Weber, P. Beckstein, V. Galindo, M. Starace, and T.Weier, Electro-vortex flow simulation using coupled meshes, Computers and Fluids 168, 101 (2018).

CURRICULUM VITÆ

Artem BLISHCHIK

10-12-1992 Born in Saint Petersburg, Russia.

EDUCATION AND WORK EXPERIENCE

1999–2002	School # 675 Saint Petersburg, Russia
2002–2010	School # 568 Saint Petersburg, Russia
2010–2014	Bachelor of Science in Applied Mathematics and Physics Peter the Great St.Petersburg Polytechnic University Saint Petersburg, Russia
2014–2016	Master of Science in Applied Mathematics and Physics Peter the Great St.Petersburg Polytechnic University Saint Petersburg, Russia
2015–2018	Computational Fluid Dynamics Engineer Krylov Research Centre Saint Petersburg, Russia
2018–2022	Ph.D. candidate Delft University of Technology Delft, The Netherlands
Thesis:	Numerical modeling of conjugate magnetohydrodynamic flow phenomena
Promotor:	Prof. dr. S. Kenjereš & Prof. dr. ir. C. R. Kleijn

LIST OF PUBLICATIONS

7. **A. Blishchik,** I. Glavinić, T. Wondrak, D. van Odyck, S. Kenjereš, *Effects of electrically conductive walls on turbulent magnetohydrodynamic flow in a continuous casting mold*, International Journal of Heat and Fluid Flow **95**, 108967 (2022).

6. **A. Blishchik,** S. Kenjereš, *Turbulence suppression and regeneration in a magnetohydrodynamic duct flow due to influence of arbitrary electrically conductive walls*, Physics of Fluids **34**, 045101 (2022).

5. I. Glavinić, I. Muttakin, S. Abouelazayem, **A. Blishchik,** F. Stefani, S. Eckert, M. Soleimani, I. Saidani, J. Hlava, S. Kenjereš, T. Wondrak, *Laboratory investigation of tomography-controlled continuous steel casting*, Sensors **22(6)**, 2195 (2022).

4. **A. Blishchik,** S. Kenjereš, *Dynamic LES of the magnetohydrodynamic flow in a square duct with the varied wall conductance parameters*, Journal of Physics: Conference Series **2116**, 012036 (2021).

3. **A. Blishchik,** S. Kenjereš, *Observation of a novel flow regime caused by finite electric wall conductance in an initially turbulent magnetohydrodynamic duct flow*, Physical Review E **104**, L013101 (2021).

2. **A. Blishchik,** M. van der Lans, S. Kenjereš, *An extensive numerical benchmark of the various magnetohydrodynamic flows*, International Journal of Heat and Fluid Flow **90**, 108800 (2021).

1. T. Wondrak, U. Hampel, M. Ratajczak, I. Glavinić, F. Stefani, S. Eckert, D. van der Plas, P. Pennerstorfer, I. Muttakin, M. Soleimani, S. Abouelazayem, J. Hlava, **A. Blishchik,** S. Kenjereš, *Real-time control of the mould flow in a model of continuous casting in frame of the TOMOCON project*, IOP Conference Series: Materials Science and Engineering **424**, 012003 (2018).